The influence of shrub expansion on albedo and the winter radiation budget in the Canadian Low Arctic

Thèse

Maria Belke Brea

Doctorat en sciences géographiques
Philosophiæ doctor (Ph. D.)

Québec, Canada

The influence of shrub expansion on albedo and the winter radiation budget in the Canadian Low Arctic

Thèse – Doctorat en sciences géographiques

Maria Belke-Brea

Sous la direction de:

Florent Dominé, directeur de recherche
Ghislain Picard, codirecteur de recherche
Stéphane Boudreau, codirecteur de recherche

Résumé

Au cours des dernières décennies, le réchauffement climatique a entrainé une arbustation accélérée des écosystèmes arctiques. En modifiant l'albédo, les arbustes influencent la température de l'atmosphère, du manteau neigeux et du pergélisol, ce qui pourrait accélérer la fonte ou le dégel de ces deux derniers et initier de fortes boucles de rétroaction positive qui accentueraient les effets des changements climatiques. L'une des conséquences principales de cette arbustation est la réduction de l'albédo de la neige par les branches qui dépassent du manteau neigeux et en assombrissent la surface. De plus, des interactions complexes entre neige et arbustes d'une part modulent la remobilisation et le transport de la neige par le vent et d'autre part accélèrent la fonte durant les redoux. Ainsi, la présence d'arbustes au sein du manteau neigeux peut affecter les propriétés physiques et optiques de la neige, altérant encore davantage l'albédo de la surface affectée. Enfin, les branches ensevelies dans la neige peuvent également influencer le budget radiatif en absorbant les rayons lumineux car ceux-ci pénètrent généralement à plus de 10 cm de profondeur dans le manteau neigeux. Pour étudier et quantifier les interactions entre la neige, les arbustes et la lumière, nous avons récolté un jeu de données unique qui compare des manteaux neigeux avec et sans arbustes. Pour tous les sites échantillonnés, nous avons mesuré l'albédo spectral *in situ* et les profils de propriétés physiques de la neige ainsi que d'irradiance. Nous avons récolté ces données dans le bas Arctique, à Umiujaq, Nord du Québec, Canada (56° N, 76° W), au cours de plusieurs campagnes de terrain d'automne et d'hiver. En nous basant sur les données obtenues ainsi que des données de taille et de distribution verticale de branches d'arbustes, nous avons développé et validé une paramétrisation simple mais efficace permettant de modéliser l'albédo de surfaces hétérogènes composées de neige et d'arbustes. Cette nouvelle paramétrisation nous a permis de modéliser l'albédo avec une erreur inférieure à 3 %. Elle peut être utilisée de manière prédictive et est facile à intégrer aux modèles de système terre.

L’albédo ainsi modélisé nous a permis d’élucider des processus importants des interactions entre la neige, les arbustes et la lumière. Nous avons trouvé que la réduction de l’albédo par les branches qui dépassent du manteau neigeux dépend de la longueur d’ondes considérée. Tôt durant la saison nivale, les branches diminuent l’albedo de 55 % à 500 nm et 18 % à 1000 nm. En revanche, l’effet des branches sur les propriétés physiques de la neige n’étaient pas suffisamment importants pour affecter l’albédo, sauf lors d’évènements climatiques extrêmes comme les blizzards ou les épisodes de chaleur. Nos résultats suggèrent que l’impact direct de l’assombrissement par les branches est largement supérieur aux effets indirects causés par les changements des propriétés physiques de la neige. Cependant, ces derniers pourraient gagner en importance si les évènements climatiques extrêmes devenaient plus fréquents au fur et à mesure que le réchauffement de l’Arctique s’intensifie. Finalement, nous montrons que l’impact des branches ensevelies sous la neige se traduit surtout par une augmentation de la fonte durant les épisodes de chaleur ainsi que par une intensification des processus métamorphiques tôt dans la saison. Cependant ces impacts étaient extrêmement localisés et restreints à l’environnement très proche des branches. Pour cette raison, il a été difficile de quantifier l’impact des branches ensevelies sur le budget radiatif terrestre, d’autant plus que les concentrations de carbone suie élevées (185 ng g^{-1}) dans le manteau neigeux d’Umiujaq ont accentué l’incertitude quant à l’effet relatif de ces deux processus sur l’albédo.

Finalement, comme notre paramétrisation pour modéliser l’albédo a été développée sur la base de données provenant d’un seul site, nous croyons qu’il serait nécessaire de la tester de manière plus générale, avec des données provenant d’autres endroits. De cette manière, elle pourrait ensuite être intégrée aux modèles de surface continentale, ce qui permettrait d’inclure un effet réaliste de l’arbustation actuelle et future de l’Arctique sur les scénarios climatiques locaux et globaux.

Abstract

Arctic warming is causing an expansion of deciduous shrubs in the Arctic tundra biome. By modifying albedo, shrubs affect the temperature of the atmosphere, snowpack and permafrost, potentially increasing permafrost thawing and snow melting, and forming a powerful feedback to global warming. The most prominent impact of shrubs is a reduction of surface albedo when dark branches protrude above the bright snow surface. Additionally, complex snow-shrub interactions modify snow redistribution during windy conditions and increase snowmelt rates during warm spells. Thus, snow over shrub-covered tundra may have different physical and optical properties, leading to further modification of surface albedo. Finally, shrub branches buried in snow may still have an impact on the radiation budget because they can absorb light rays which generally penetrate deeper than 10 cm into the snowpack. To study and quantify the snow-shrub-light interactions, we collected a unique dataset comparing snowpacks with and without shrubs. For every site sampled, we measured *in situ* spectral albedo (400–1080 nm) and recorded snow physical properties and irradiance profiles. These data were acquired in a low Arctic site near Umiujaq, Northern Quebec, Canada (56° N, 76° W), during several field campaigns in autumn and winter. Based on these field data and a dataset of branch sizes and vertical distribution, a simple yet accurate parameterization for modeling albedo of mixed snow-shrub surfaces was developed and validated. This new parameterization had an accuracy of 3 %, can be used in a predictive way, and is easy to implement in earth system models.

We uncovered important insights on snow-shrub-light interactions. Surface darkening by protruding branches was wavelength-dependent, and decreased albedo early in the snow season by 55 % at 500 nm and 18 % at 1000 nm. Changes in snow physical properties that were significant enough to impact albedo only occurred in conjunction with extreme weather events like after blizzards or during warm spells. Thus, the direct impact of darkening from shrubs likely dominates over the indirect impact from changes in snow

physical properties, however the latter may gain in importance if extreme weather events become more frequent as Arctic warming progresses. The impact of buried branches was very localized, increasing snow melting during warm spells and enhancing snow metamorphic processes early in the season in the direct vicinity of branches. However, quantifying the impact of buried branches on the radiation budget was challenging due to their highly localized effect and because of high black carbon concentrations in the snowpack at our study site, which reached 185 ng g-1.

We suggest that future research test the parameterization developed here more broadly, as this study was based on data from just one study site. The parametrization can then be implemented into land surface models, allowing for reliable estimates of the effect of current and projected Arctic shrubification on global and regional warming.

Table of Contents

Liste of Tables

Liste of Figures

List of Acronyms

The acronyms used in this PhD thesis are listed below.

Acronym	**Meaning**
BAI	*Branch Area Index*
BC	*Black Carbon*
DF	*Degree of Freedom*
DUFISSS	*DUal Frequency Integrating Sphere for Snow SSA measurement*
IPCC	*Intergovernmental Panel on Climate Change*
LAI	*Leaf Area Index*
LAP	*Light Absorbing Particles*
LME	*Linear Mixing Equation*
LSM	*Land Surface Model*
MAE	*Mass Absorption Efficiency*
NLS	*Nonlinear Least-Square regression*
RMSE	*Root Mean Square Error*
SBDART	*Santa Barbara DISORT Atmospheric Radiative Transfer*
Snow MCML	*Monte Carlo modeling of light transport in multi-layered tissues, for snow*
SOLEXS	*SOLar EXtinction in Snow*
SSA	*Specific Surface Area*
SZA	*Solar Zenith Angle*
TARTES	*Two-Stream Analytical Radiative TransfEr in Snow*
ZOI	*Zone Of Interest to determine extinction coefficients from SOLEXS profiles*

List of Notations

The notations used in this PhD thesis are listed below together with a description.

Notations	Description
$\Gamma_{snow\text{-}free}$	(snow-free) vegetation fraction used in Liston and Hiemstra (2011)
α_{mix_obs}	Measured mixed surface albedo
$\alpha_{mix\_obs,corr}$	Measured mixed surface albedo corrected with scaling factor *A*
α_{mix_calc}	Mixed surface albedo calculated with the LME
α_{snow}	Snow albedo parameter in the LME
α_{sn_obs}	Measured snow albedo at shrub-free sites
$\alpha_{sn\_obs,\ corr}$	Measured snow albedo at shrub-free sites corrected with scaling factor *A*
α_{sn_TARTES}	Snow albedo calculated with TARTES using SSA from shrub-free sites
α_{veg}	Shrub albedo parameter in the LME
$\alpha_{veg\_y,}$ α_{veg_o}, α_{veg_y+o}	Shrub albedo measured by Juszak et al. (2014) for young branches (α_{veg_y}), old branches (α_{veg_o}) and an average of young and old branches (α_{veg_y+o})
χ	Weighting factor in the LME
χ_{adj}	Weighting factor deduced with a least-square approach using measured albedo
χ_{calc}	Weighting factor calculated with allometric approach
ω_{rod}	The albedo of the measuring rod in SOLEXS
A	Scaling factor, used to correct measured spectral albedo
$BAI_{exposed}$	Branch Area Index of branches protruding above the snow
BAI_{total}	Total Branch Area Index before snow burial
C	Bending factor in exposed-vegetation function

DF_{glob}, DF_{loc}	Degree of freedom for the local (*loc*) and global (*glob*) regression used to establish the BAI–H_{veg} allometric equation
E_{snow}, E_{LAP}, E_{rod}, E_{shrub}	Material-specific extinction of snow, impurities, the measuring rod and shrubs
F	F-ratio calculated with an F-test to compare the quality of fit between the local model and the global model, see also Eq. (3.3)
H_{veg}	Shrub height, cm
H_{snow}	Snow height, cm
I_{log}	Log-irradiance profiles measured with SOLEXS
SSE_{glob}, SSE_{loc}	Error sum-of-square for the local (*loc*) and global (*glob*) regression used to establish the BAI–H_{veg} allometric equation
a, b	Fitted coefficients in allometric equations
d	Shape factor in exposed-vegetation function
d_{opt}	Optical snow grain diameter
k	Backscattering factor
k_{e_calc}	Extinction coefficient, calculated as a function of snow physical properties and impurities
k_{e_meas}	Extinction coefficient, determined with linear regression from SOLEXS measurments
f_{exp}	Exposed-vegetation factor

I dedicate this thesis to Gloria Brea Morales.
I whish I could share this work with you.

Snowflakes are one of nature's most fragile things,

but just look what they can do when they stick together.

Vista M. Kelly

Acknowledgements

Moving to another country to start a PhD thesis is, quite frankly, a crazy endeavor. There is a new language to be learned, a new culture to be discovered, new ties of friendship to be formed and old ones to be kept alive over a long distance. And then there is the science itself. I could not have survived all of this without a great group of people around me!

The first thank you goes to my supervisor, Florent Dominé. You created the conditions for this project to happen, you supported my work financially and you guided me through the obstacles I encountered during my thesis. I also want to give you here the award as the cook of the best ‘northernmost’ tartiflette and ‘northernmost’ apple pie. Next, I want to thank my co-supervisors, Ghislain Picard and Stéphane Boudreau. Ghislain, you were an invaluable adviser and your input on snow optics always improved my work – thank you for that. Stéphane, you helped me out a lot with data on Arctic shrubs, your specialized knowledge on the flora of the Arctic tundra, and last but not least, with much encouraging words.

The field work was an essential part of this thesis, and I want to thank all the people who contributed to make this extraordinary arctic experience possible. I am very grateful to the Centre d’Études Nordiques (CEN) for providing and maintaining the Umiujaq research station. The communities of Umiujaq and Pond Inlet were amazing hosts, and they helped me out of several tight spots during the field work. A special thank you goes to Mathieu, you were a great field partner and friend in numerous arctic adventures! You always waited patiently with me for good lighting conditions to measure albedo, no matter how cold it was. Thank you also to Laurent Arnaud, for your advice and for your logistical skills.

Finally, I want to thank my family and friends. Most of all, Frédéric LeTourneux, you were always by my side, with comfort food, a big hug and an endless stream of encouraging words – thank you so much for your support! I also want to thank the infamous group of Downtown Partyeurs, in who’s company I could recharge my batteries, and the group at the

Cabane à Jack – you made the last weeks of writing so much easier. My last but very big thank you goes to Germany to my family and my old friends: thank you for your text messages, your visits and for just being there!

Avant-propos

This document is a synthesis of my scientific work which has been published, or is in preparation to be published, as scientific articles. The articles are integrated in chapters 2, 3 and 4, justifying the format « thèse – article » of this thesis. Each article chapter was extended by a preamble to make the understanding of the manuscript easier. Writing a thesis in the format « thèse – article » creates some redundancy concerning the description of the study sites, the applied methodologies and the mathematical equations. On the other hand, the chosen format allows that every chapter is read independantly.

The scientific article in Chapter 2 has been published in the peer-reviewed *Journal of Climate* on 15 January 2020 under the open access licence (Belke-Brea et al. 2020). I am first author of this article, was responsable for the field work and the analysis of the data. The co-authors of the article are F. Domine, M. Barrere, G. Picard, L. Arnaud.

The scientific article in Chapter 3 has been accepted by the peer-reviewed *Journal of Hydrometeorologie* on 10 August 2020. I am first author of this arcticle and I was responsible for most of the field work and the developement of the new method presented in the article. The co-authors of the article are F. Domine, S. Boudreau, G. Picard, M. Barrere, L. Arnaud and M. Paradis.

The manuscript in Chapter 4 is in preparation to be submitted to the peer-reviewed journal *Biogeosciences*. I am the first author of this mansucript and I was responsible for the field work as well as the analysis of the field and model data. Model simulations in this article were performed by Ghislain Picard. The co-authors of the manuscript are F. Domine, G. Picard and L. Arnaud.

Introduction

Snow surfaces – the cooling element in the Earth's climate system

Snow is a ubiquitous feature of the Northern Hemisphere and may cover up to 49 % of the land surface at its maximal extent in January (Lemke et al. 2007, Déry and Brown 2007). Snow extent is largest at high northern latitudes, where snow covers the ground for most of the year (7–10 months of the year; Callaghan et al. 2012, Barry and Hall-McKim, 2014). Initial research on snow was mainly conducted at lower latitudes because of its importance for water management, for the outdoor industry (e.g. ski) and for detailed avalanche forecasting. However, since 1990, the observed increase in atmospheric CO_2 which is resulting in global warming has increasingly lead researchers to investigate the fundamental role played by snow on the global climate. A question of interest is how changes in snow cover, particularly in the Arctic where snow cover has the largest extent, may positively feedback on global warming.

The importance of snow to the climate system is mainly due to its high reflectivity (albedo) of solar radiation (Figure 0.1). Snow-covered areas increase the planetary albedo, so that a large portion of solar radiation is reflected into space rather than being absorbed by the Earth's surface. Large expanses of snow-covered areas therefore have an overall cooling effect on the planet. However, rising temperatures due to global warming reduce the extent and duration of the global snow cover, which in turn reduces the cooling effect of snow, and amplifies global warming (Derksen and Brown 2012). As temperatures continue to increase, snow cover decreases further, establishing a powerful positive feedback loop called the snow-albedo feedback.

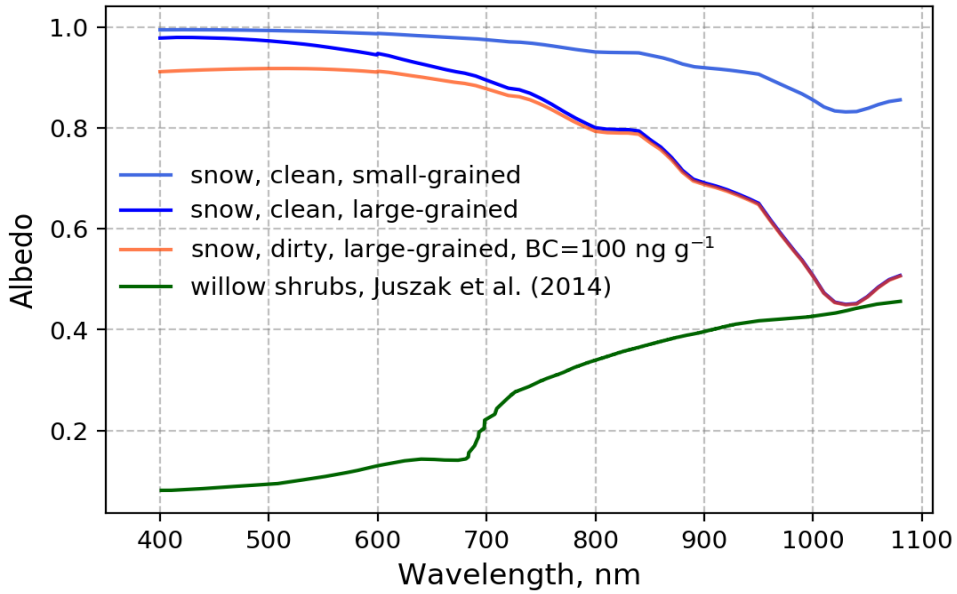

Figure 0.1 Overview of different spectral albedo plots, including the high albedo of pure and small-grained snow and the lower albedo of dirty and large-grained snow. Dirty snow is mixed with 100 ng g^{-1} of black carbon (BC). This graph shows the range of albedo values for snow covered surfaces. All snow albedo plots were calculated using the radiative transfer model TARTES (Libois et al. 2013). Also shown is the albedo of Betula nana shrubs as measured in Siberia by Juszak et al. (2014). Shrub albedo is considerably lower than snow albedo, particularly in the visible range.

The snow-albedo feedback is only partly caused by the loss of snow cover: an equally important role may be attributed to the natural variation of snow albedo (Fernandes et al. 2009, Picard et al. 2012). These variations range between 0.6 and 0.85 in the broadband (350–1000 nm) and depend on snow physical properties such as snow density as well as size and shape of snow grains. Snow grain size is a particularly important determinant of snow albedo, because the larger the grains the higher the probability for light to be absorbed (Figure 0.1) (O'brian and Munis 1975, Warren 1982). The reason for the natural variation of snow albedo is that grain size in the snowpacks changes over time, a process called snow metamorphism (Sommerfeld and LaChapelle 1970, Grenfell and Maykut 1977). Snow metamorphism is driven by meteorological parameters, like wind and temperature, and can have opposite effects on snow grain size. For example, in the Arctic strong winds roll snow grains over the ground abrading them and thus creating layers of small rounded grains (Schmidt, 1984, Domine et al. 2007). In contrast, when temperatures are around 0°C, melt-freezing events can produce snow layers composed of melt-freeze

crystals which have particularly large grain sizes. Because light absorption depends on grain size, snow albedo of wind-drifted small grains is high compared to albedo of a melt-freeze layer with large grains (Figure 0.1). As climate warms air temperatures increase in the Arctic, and snow precipitation, wind patterns and snow melt events change which will impact Arctic snow metamorphism processes and affect snow albedo values.

Another factor that further amplifies the snow-albedo feedback is the warming-induced transition from herb, moss and lichen tundra to shrub tundra which has been observed in the Arctic in the last decades (Tape et al. 2006, Ropars and Boudreau 2012). Erect shrubs can impact winter surface albedo by several processes. The most obvious one results from branches which have low albedo (Figure 0.1) and that protrude above the snow causing a darkening of the formerly bright snow surface (Figure 0.2). In addition, branches that are buried in the snowpack also absorb incoming light and reduce albedo because snow is a translucent medium into which light penetrates up to tens of centimeters (Warren 1982, France et al. 2011, Picard et al. 2016, Tuzet et al. 2019). Finally, complex snow-shrub interactions can alter snow metamorphism and snow grain size, which ultimately changes snow albedo. To calculate the radiative effect of shrub expansion at specific sites or on a pan-Arctic scale, simple linear mixing equations (LME) were used in previous studies (Sturm et al. 2005, Liston and Hiemstra 2011, Ménard et al. 2014). With these LMEs, the albedo of mixed snow-shrub surfaces is calculated as a function of snow and shrub albedo and a factor that weights snow and shrub albedo with respect to the surface they each cover. However, it remains unclear whether or not this simplified linear-mixing approach is suitable as a parameterization of mixed surface albedo because there are few broadband and no spectral albedo *in situ* measurements against which the model could be validated. Current LMEs neglect the effect of buried branches and of snow-shrub interactions, which may introduce significant inaccuracies to the LME calculations. Moreover, the weighting factor used to weight snow and shrub albedo is deduced from ground-based, airborne, or satellite imagery analyses. Since the imagery is required for the model to work, we cannot currently use this model in any predictive way.

In conclusion, modeling the effect of shrubs on albedo and the radiation budget is still subject to large uncertainties. Indeed, the linear mixing equation, which has been

implemented in most climate and land surface models, has hardly been tested, there is no validated method to calculate the fractional surface covered by branches (i.e. the weighting factor described above), and there are no quantitative estimates of neither the impact of buried branches nor the indirect effects of snow-shrub interactions on snow albedo. As such these effects are neglected in current modeling approaches. The goal of this thesis is to increase the understanding on shrub-light-snow interactions, and to use the acquired knowledge to develop a validated modeling approach that accurately calculates the albedo of mixed snow-shrubs surfaces. This is done in three steps. 1) The linear mixing equation is verified using unique *in situ* measurements of both spectral albedo and snow physical properties. Furthermore, the *in situ* measurements are used to quantify the effect of snow-shrubs interactions on snow albedo. 2) An allometric approach is developed to calculate the weighting factor from snow and shrub height. 3) The buried-branch effect is analyzed in irradiance profiles measured in snowpacks with shrubs.

Figure 0.2 Contrast of a bright snow surface and a mixed snow-shrub surface darkened by protruding branches in Umiujaq.

Chapter 1

Context and literature overview

1.1 Brief introduction to the Earth's climate system and its dynamics

1.1.1 Climate and the role of the radiation budget

Climate is a set of meteorological variables, like air temperature or the amount of precipitation, which describes the typical range of weather conditions of a region. Understanding its origin and development is crucial as it forms the natural environment in which human society evolves (Xu et al. 2020). The Earth's climate is produced by a world-spanning system. This system consists of a complex network of energy, mass and momentum fluxes flowing between the Earth's five major biophysical spheres: the atmosphere, hydrosphere, cryosphere, biosphere and lithosphere. The initial driver for all those fluxes is the radiation energy the Earth receives from the Sun (e.g. Eddy 1977, Kopp and Lean 2011).

The radiation energy the Earth receives from the Sun at the top of the atmosphere corresponds roughly to 340 W m^{-2}, but only a fraction of this incoming radiation remains in the Earth's system (Figure 1.1., yellow arrows, Stephens et al. 2012). Note that 340 W m^{-2} is a global surface average, which takes into account the spherical shape of the Earth. The flux emitted by the sun is acctually 1361 W m^{-2}, and thus incoming radiation for a specific geographical location at a specific time of the year can be larger than 340 W m^{-2}. The magnitude of the fraction of incoming radiaiton that remains in the Earth's system depends on the Earth's reflectivity. Reflectivity is usually described by the albedo parameter, which is the Latin word for 'whiteness'. Albedo is measured as the ratio of reflected vs. total

incoming radiation. Albedo values thus vary on a scale from 0 to 1, where 0 corresponds to a black body that absorbs all incoming radiation, and 1 to a white body that reflects all incoming radiation. The current planetary albedo has a mean value of 0.3 which indicates that one third, or 102 Wm^{-2} of the incoming solar radiation is reflected by the Earth's surface and atmosphere and is lost into space (Vonder Haar et al. 1981). The remaining 238 Wm^{-2} are absorbed in the atmosphere (32 %) and the Earth's surface (68 %) (Stephens et al. 2012). Generally, the solar radiation absorbed by an object increases its temperature, and is thus radiated out as heat. The planetary albedo is the most important factor controlling the net amount of absorbed solar radiation, consequently its value directly regulates global temperatures.

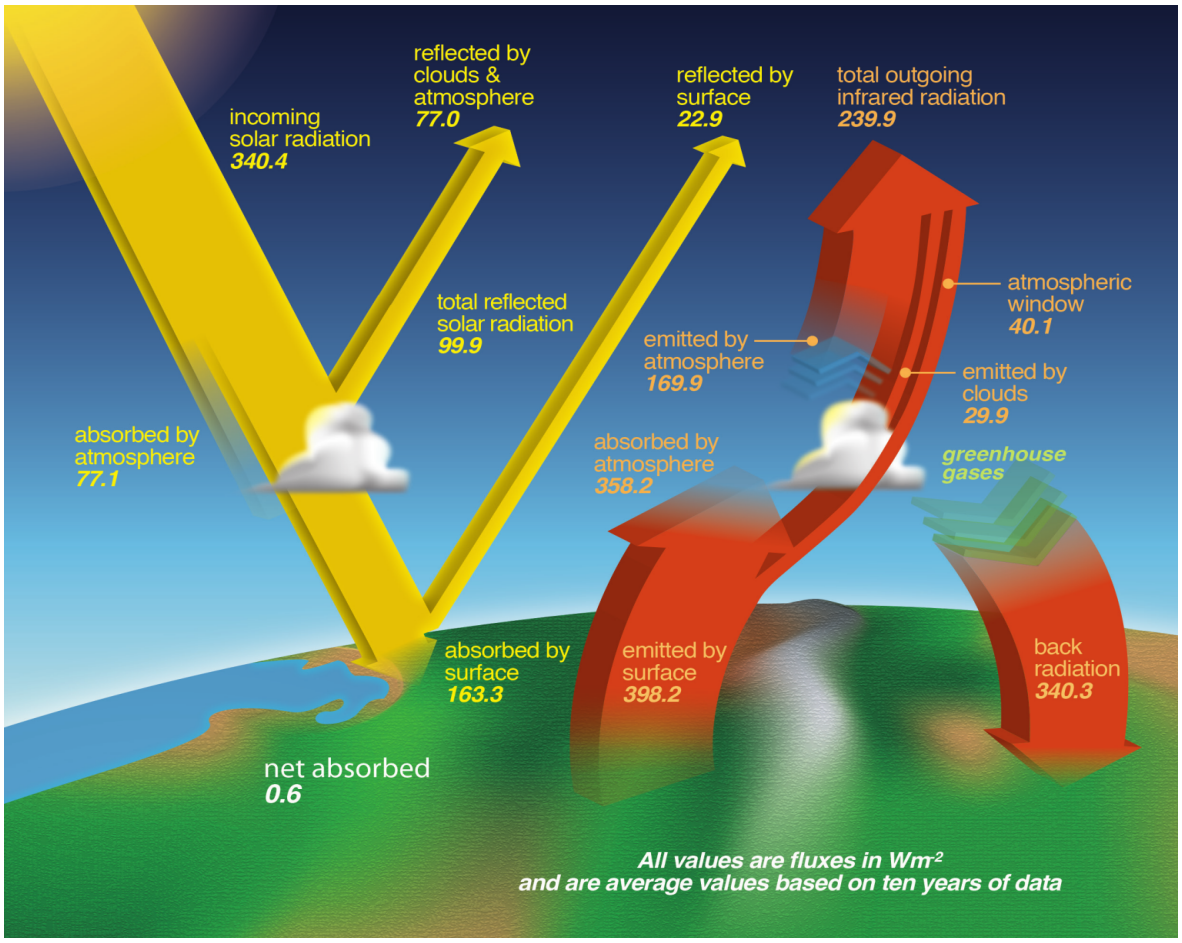

Figure 1.1. Schema of the Earth's radiative fluxes. Solar radiation is shown as yellow arrows and terrestrial radiation as red arrows. Image source: http://science-edu.larc.nasa.gov/energy_budget/ quoting Loeb et al. 2009 and Trenberth et al. 2009.

Every object with a temperature above absolute zero (0K, -273°C) emits radiation (Stefan–Boltzmann law). Thanks to the warming effect of the Sun, the Earth's temperature is well above absolute zero, causing the Earth to emit radiation in the infrared spectrum (6 000–20 000 nm, Figure 1.1., red arrows). This terrestrial radiation is important for global climate because its interactions with the Earth's atmosphere play a crucial role in increasing global temperatures. Calculations have shown that if the Earth had no atmosphere, the warming effect of the Sun would only manage to keep the mean global temperature at -15°C, 30K lower than the current average of 15°C (Berger and Tricot 1992). This is because the Earth's atmosphere is highly absorbent for the terrestrial infrared radiation. Consequently, almost 90 % of the radiation emitted from the Earth's surface is absorbed as it crosses the atmosphere and is radiated back to the Earth's surface, increasing its temperature (Ramanathan 1988, Stephens et al. 2012). This process is commonly known as the greenhouse effect (Poynting 1907, Ramanathan 1988). The absorbing agents in the atmosphere are gas molecules of water vapor (H_2O_{vap}), carbon dioxide (CO_2), and methane (CH_4) (Tyndall 1861, Arrhenius 1896, Berger and Tricot 1992). The net strength of the greenhouse effect depends on the global concentration of those greenhouse gases in the atmosphere. The greenhouse effect is the most important factor controlling the net amount of absorbed infrared radiation and its magnitude directly regulates global temperatures.

In summary, the planetary albedo and the greenhouse effect are the two principal mechanisms controlling the net amount of absorbed radiation. Together, they determine the Earth's net radiation budget and regulate global temperatures. Therefore, changes in either the strength of the greenhouse effect or the value of planetary albedo modify the radiation budget, influence global temperatures and have direct implications for global climate.

1.1.2 Climate change and its implication for human society

The radiation budget of the Earth varies at different timescales and this causes the Earth's climate to change as well. During the past few millions of years at least, long-term variations have been cyclic and have happened on scales of 21 000 to 100 000 years (Hays et al. 1976). These long-term variations are forced by regular changes in the Earth's orbit around the Sun (Milankovich 1948, Imbrie and Imbrie 1980). More specifically they are forced by changes in the axis tilt, in the shape of the orbit around the Sun (eccentricity) and

the Earth's position relative to the Sun during the spring equinox (precession). These orbital effects modify the amount and timing of solar radiation reaching the Earth. The cyclical variation in incoming radiation results in regular alterations in climate between glacial (cold) and interglacial (warm) periods (Hays et al. 1976). These regular climate alterations are called the Milankovich cycles, after the Serbian astronomer who drew the link between the amount of incoming solar radiation and the Earth's climate and predicted cyclical climate changes (Milankovich, 1948). Short-term variation in the radiation budget, and thus in climate, can also be caused by internal forcing mechanisms. These internal mechanisms modify the planetary albedo or change the strength of the greenhouse effect by altering the concentrations of greenhouse gas in the atmosphere. Multiple processes can act as internal forcing mechanisms and result in abrupt global climate change. Those include large volcanic eruptions, meteorite impacts (Crowley 2000) and large-scale changes in the land surface (Pielke et al. 2002, Bright et al. 2017). Changes to the land surface may be caused by biological changes such as large-scale shifts in vegetation patterns or variations in the physiology of photosynthetic plants (Jahn et al. 2005, Claussen 2009, Bonan 2008). It may also be caused by geophysical processes impacting the distribution of water and land or the extent of snow-covered surfaces (Claussen 2009, Chapin et al. 2005, Callaghan et al. 2012). Since climate is highly sensitive to a vast array of factors occurring at different spatiotemporal scales, it is highly dynamic.

Today's climate belongs to a long-term interglacial period called the Holocene (11 700 BC – today) which has undergone several short-term climate variations since the onset of human civilization (Cowie, 2013). According to historical records, the success or failure of previous human civilizations has been closely linked to the climatic variations they experienced (Cullen et al. 2000, Chepstow-Lusty et al. 2009). Periods of climate change were often marked by chaos and economic difficulties. The best documented historical climate change and related impact on humans is the transition from the Medieval warm period (900 to 1200 AC) to the Little Ice Age (1550 – 1750 AC). Historical records of food prices and climatic conditions show that changes in temperature caused an 8-fold increase in wheat prices (Cowie, 2013). The consequence were several famines happening across Europe which caused the death of over 1.5 million people. It is thought that these famines were particularly severe because the agricultural system was still embedded in the Medieval

warm period mode, indicating a lack of adaption on the part of society (Büntgen et al. 2011). Current climate records show that today's civilization is on the verge of a new climate change and, looking back to the past, we can expect that it will impact our societal and economic structures if we fail to develop efficient adaption strategies (IPCC 2013, Xu et al 2020).

Current global temperatures are increasing significantly, and climate today is 1K hotter than it was during the reference period 1950–1980 (Figure 1.2; IPCC 2013). Surface temperatures have been measured by scientists in a systematic way since 1880 and the resulting long-term time series allow to determine today's temperature anomalies with a high level of certainty. Temperatures have been continuously increasing since 1970 and the warming trend has intensified in the last decade with years 2014, 2015 and 2016 each setting new heat records. The observed increases in temperature are caused by a higher concentration of greenhouse gases in the atmosphere, particularly by an increase in carbon dioxide (CO_2) (Berger and Tricot 1992). Continuous recordings of the concentration of atmospheric CO_2 date back to 1958. Those recordings were started by David Keeling in the Mauna Loa Observatory, Hawaii, where CO_2 concentrations are still measured today (Keeling et al. 1976). The so-called Keeling curve reveals a steep increase in CO_2 concentrations from 320 ppm in 1960 to a current value of 414 ppm in February 2020 (Figure 1.2; NOAA, ESRL). It is today scientific consensus that this extreme increase in atmospheric CO_2 is the result of human activity since the industrial revolution, mainly caused by fossil fuel burning and cement production (IPCC, 2013). Consequently, the currently observed global warming is also human-made.

As global temperatures rise, other indicators of climate change are starting to emerge. These warming-induced changes modify the environment and have already started to impact the functioning of socio-economic structures. For example, melting mountain glaciers have been observed on every continent impacting the ski tourism industry and the economy of mountain communities (IPCC, 2013). The global sea level is rising at a rate of 3.2 mm yr^{-1} since 1993 due to climate warming, and this threatens island countries as well as cities built along the coasts (IPCC, Chruch et al. 2013). As a consequence of climate change, the frequency of extreme weather events is increasing, with devastating

consequences on property, food and water security, but also directly causing the death of thousands of people annually (Coumou and Rahmstorf 2012). These events highlight the need for policymakers to develop adaption strategies, create solutions to limit CO_2 emissions, and find ways to mitigate climate change impacts to allow for a gradual adaption process. To aid policymakers in their task, the climate research community regularly releases an assessment report on the scientific basis of climate change and on projected climate change scenarios and future risks (the IPCC report). An indispensable tool for the climate projections in the IPCC report are Earth System Models (ESMs), which couple the Earth's five major biophysical spheres to represent complex climate processes. Climate research has been putting much effort into developing sophisticated ESMs that allow for reliable forecasts of climate change in the next decades and centuries.

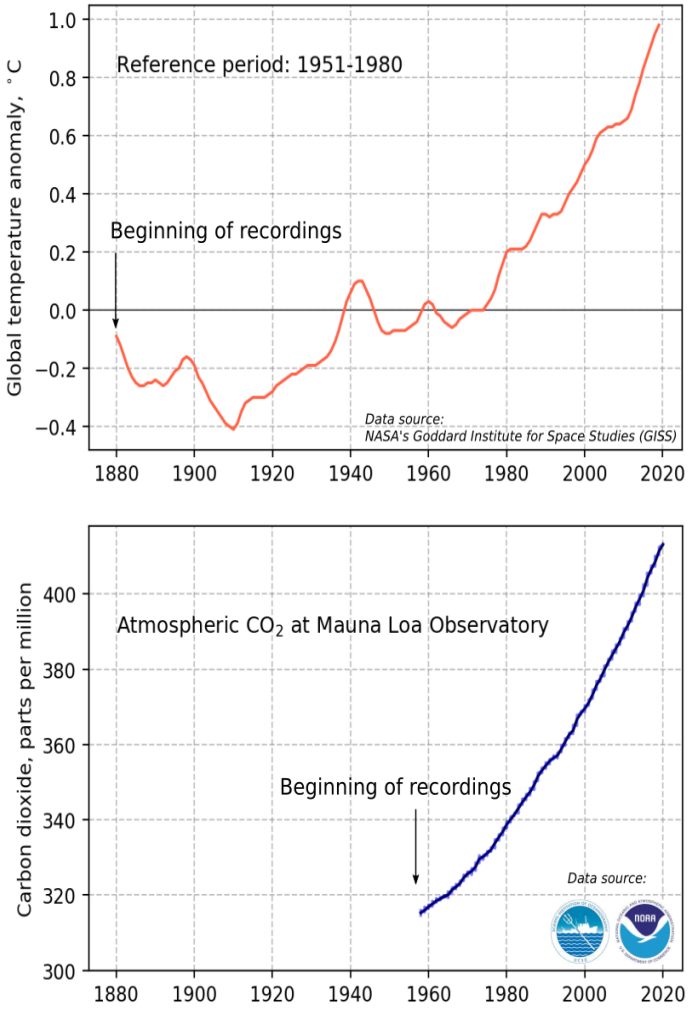

Figure 1.2. Global temperature anomalies (upper graph) measured from 1880 to present and increase in the atmospheric CO_2 concentration (lower graph) measured at the Mauna Loa Observatory, Hawaii. Atmospheric CO_2 concentrations increased steeply since the onset of measurements in 1960 and global temperatures have been rising since the 1970s. Data sets to create the image were taken from NASA, NOAA and the UCSD institution of oceanography.

The performance of climate models has increased significantly since the human-induced global warming became scientific consensus in the 1990s. However, it is still challenging to accurately project climate change, because the Earth's climate system is highly complex and climate results from a myriad of intertwined processes. Increases in temperature are currently provoking a cascade of major changes in all five biophysical spheres, which in turn feedback on global climate by either impacting the planetary albedo or modifying greenhouse gas concentrations. These feedbacks can go in different directions and can

either amplify or reduce global warming. Many of these feedbacks are not well understood and their role in climate models is therefore greatly oversimplified. Of particular importance are climate change processes in the Arctic tundra because they have the potential to generate powerful feedback loops. However, processes in the Arctic tundra are still poorly understood because of the limited infrastructures for science, the prohibitive expedition costs and the harsh fieldwork conditions which all hamper the gathering of high-quality quantitative data, especially in winter.

1.1.3 Climate change and climate feedbacks in the Arctic tundra

Temperatures are increasing twice as fast in the Arctic compared to the rest of the planet (Figure 1.3; Overland and Wang 2016). Due to this amplified warming, climate change is quickly modifying bio-geophysical processes in the Arctic tundra, and these modifications are feeding back to global warming through several powerful positive feedback loops (Loranty et al. 2012). Among the most important feedbacks are the snow-albedo feedback and the permafrost feedback.

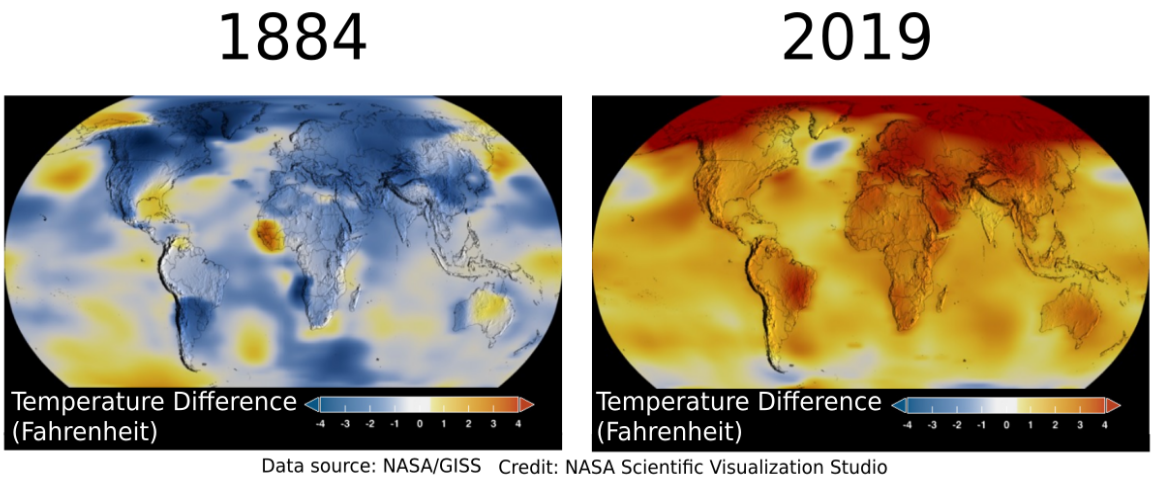

Figure 1.3. Global temperature change over the time period 1884 to 2019, which highlights the amplified Arctic warming. Temperature differences are shown compared to a baseline average from 1951 to 1980.

1.1.3.1 Arctic tundra climate feedbacks

In the Arctic tundra, snow covers the ground during up to 10 months of the year and stretches over 17.8 million km^2 (Callaghan et al. 2012, Barry and Hall-McKim 2014). As snow surfaces have high broadband albedo (0.6 to 0.85 in the visible to near-infrared range from 350 to 1000 nm) (Grenfell and Maykut 1977), large areas covered by snow increase the global planetary albedo and act as cooling elements in the Earth's climate system. The current increase in temperatures, however, increases snow melting and satellite data has shown that June snow cover in the Arctic has declined by 13.4 % per decade since 1967 (Estilow et al. 2015, Mudryk et al. 2017). Moreover, snow-cover duration in spring has shortened by up to 3.9 days per decade (Brown et al. 2017). A reduction in snow cover extent and duration warms the underlying surfaces, which then causes further snow melting, creating the positive snow-albedo feedback (Serreze et al. 2009). The snow-albedo feedback has been implemented in climate models, and is estimated to increase the net radiation budget by 0.1 – 0.22 W m^{-2} (Flanner et al. 2011). A second, less obvious factor responsible for surface albedo changes in the Arctic tundra is the high variability of snow albedo, which fluctuates between 0.6 and 0.85 depending on the snow physical properties in the surface layer of the snowpack (Grenfell and Maykut 1977). Snow physical properties at the surface of the snowpack are largely determined by meteorological parameters like air temperature, precipitation rates and wind speed. As climate changes in the Arctic, those meteorological parameters are also changing. Consequently, snow physical properties, and thus snow albedo, are expected to change as well (Fernandes et al. 2009). However, this effect has received little attention and its potential impact on global climate is unclear because snow physical properties cannot be accurately calculated by current available models (Barrere et al. 2017).

The second important feedback is the permafrost feedback. Permafrost, i.e. soils that remain frozen for at least two consecutive years, makes up most of Arctic soils and is thought to store large amounts of organic carbon (i.e. between 1460 to 1600 Pg; Schuur and Mack 2018). In non-permafrost soils, organic carbon is introduced from plants into the soils where it is decomposed by microorganisms and re-emitted into the atmosphere as CO_2 or

methane (CH_4). The frozen state of permafrost soils prevents this decomposition, and organic carbon is stored rather than re-emitted into the atmosphere as greenhouse gases. While frozen, Arctic soils are a carbon sink that reduces the global atmospheric greenhouse gas concentrations. Their impact is particularly important because permafrosts covers 24 % of the exposed land surface in the Northern Hemisphere (Schuur and Mack 2018). However, with current Arctic warming, permafrost soils are thawing on a pan-Arctic scale, potentially turning from a carbon sink to a carbon source (Serreze et al. 2000, Schaefer et al. 2011, IPCC 2013). As permafrost thaws, the stock of organic carbon becomes accessible to microorganisms and start to be decomposed into CO_2 and CH_4 (Schuur et al. 2008). This in turn increases greenhouse gas concentrations and the strength of the greenhouse effect which results in further warming and more intense permafrost thawing. A positive feedback is thus formed between permafrost and global warming (Schuur et al. 2015, Schaefer et al. 2014). This permafrost feedback is expected to have an important effect on global climate because it could triple the amount of greenhouse gases in the atmosphere, should all stored carbon be released (Tarnocai et al. 2009, Koven et al. 2011). However, there is much uncertainty on the rate of permafrost thawing which depends, among other factors, on air temperatures and, in winter, on the insulating properties of the snowpack (Sturm et al. 2001, Zhang 2005). It is known that the insulation of a snowpack is determined by its physical properties (Sturm and Benson 1997). However, as it is currently not possible to simulate snow physical properties of Arctic snowpacks (Barrere et al. 2017), large uncertainties are introduced to projected permafrost thawing rates and the magnitude of the permafrost feedback. A better understanding of the evolution of the Arctic snowpack and its insulating properties is crucial to determine the magnitude of the permafrost feedback.

1.1.3.2 Warming-induced vegetation shifts in the tundra biome

In response to temperature increases in the Arctic, a large-scale vegetation shift is happening in the tundra biome. This shift has been visible on satellite images as a greening trend since 1980. Vegetation greenness in satellite images is determined with the Normalized Differenced Vegetation Index (NDVI), which is calculated from spectral reflectance in red (580–680 nm) and near-infrared bands (725–1100 nm) (Jia et al. 2009, Ju and Masek 2016). The greening is thought to be caused by an increase in shrub abundance

(Myers-Smith et al. 2011, McManus et al. 2012), which is supported by plot-scale evidence from numerous studies. Those studies have reported shrub expansion from sites around the circumpolar Arctic, in northern Alaska (Sturm et al. 2001, Tape et al. 2006), Arctic Russia (Frost and Epstein 2014), northern Scandinavia, Arctic Canada (Lantz et al. 2013, Fraser et al. 2014) and subarctic Québec (Ropars and Boudreau 2012, Provencher-Nolet et al. 2014). Expanding shrub species included alder (*Alnus spp.*), willow (*Salix spp.*) and birches (*Betula spp.*). The expansion seems to manifest itself in different ways: through increases in growth resulting in taller shrubs, through an infilling of previously existing shrub patches or through a general northward advance of the shrub line (Myers-Smith et al. 2011). Shrub expansion has been positively associated with the tundra's warming trend, an association also supported by long-term warming experiments that documented an increase in deciduous shrubs with increased temperatures (Chapin et al. 1995, Elmendorf et al. 2012). Shrub growth is further increased at sites where the landscapes have been disturbed through fire and permafrost degradation (Myers-Smith et al. 2011). As warming in the Arctic continues, those disturbances of the Arctic landscape are expected to become more frequent. It is thus very likely that shrubs will continue to expand into the tundra biome.

The expansion of shrubs into the tundra biome constitutes a major change for the Arctic ecosystem. For example, shrubs impact the tundra's hydrological and nutritive cycles, modify the exchange of energy and matter between land and the atmosphere and influence other flora and fauna living in the Arctic tundra. During the snow season, shrubs impact snow accumulation patterns increasing snow height when protruding branches trap wind-blown snow and impact also the tundra's radiation budget with important implication for global and regional climate (e.g. Roche and Allard 1996, Sturm et al. 2005, Loranty et al. 2011, Barrère et al. 2018). Moreover, shrub-snow interactions change snowmelt timing and wind-driven snow accumulation and erosion patterns, and thus alter the microstructure of the snowpack and snow albedo (Roche and Allard 1996, Sturm et al. 2005, Pomeroy et al. 2006, Marsh et al. 2010). Before we proceed to evaluate the complex mechanisms of shrubs impacting snow and the tundra radiation budget, a theoretical understanding of the evolution of snow physical and optical properties in a shrub-free snowpack is necessary.

1.2 Theoretical background on snow physical and optical properties

1.2.1 Snow metamorphism

Snow metamorphism refers to all physical processes which affect snow grain size, shape, and density after precipitation and is driven by climatic variables such as wind, precipitation and temperature. In general, climatic characteristics in the Arctic feature strong winds and a rapid cooling of the atmosphere in autumn and early winter. This establishes a strong temperature gradient in the snowpack between the warm soils (temperatures around 0°C) and the cold atmosphere (temperatures as low as -30°C). Based on these climatic conditions, two main metamorphic processes can be distinguished: a) temperature-gradient metamorphism (Sturm and Benson 1997) and b) wind-driven (mechanical) metamorphism.

Temperature gradient metamorphism

Temperature gradients in a snowpack provoke a gradient in water vapor pressure (P H_2O), because P H_2O increases with temperature (P H_2O ~165 Pa at -15°C and ~610 Pa at 0°C). The high temperature gradients found in the Arctic snowpack in autumn generate strong P H_2O gradients which cause sublimation at the top of snow crystals. The generated water vapor then moves along the temperature gradient, and condenses at the colder base of overlying crystals. Overall, this generates an upward water vapor flux which transfers mass from the base to the top of the snowpack, resulting in grain growth. Temperature-gradient metamorphism creates faceted crystals (Figure 1.4a) which, once grain size exceeds 1–2 mm, become hollow, cup-shaped crystals called depth hoar that can reach up to 3 cm in size (Akitaya 1974). The mass transport associated with upward water vapor fluxes results in snow layers with low densities (typically between 200–350 kg m^{-3}; Sturm and Benson 1997, Domine et al. 2007).

Wind-driven metamorphism

Freshly precipitated snow has small grain sizes and is easily re-transported when wind speed is >5 m s^{-1}. Transported by wind, grains roll and bounce over the ground, which results in their fragmentation, abrasion and sublimation and forms small rounded grains of 0.2 to 0.3 mm in diameter (Figure 1.4b) (Domine et al. 2007). Wind-drifted snow

accumulates at the lee-side of obstacles and in depressions, forming dense wind-packed snow layers. The density of the wind packs depends on wind speed but is generally high, ranging between 300 and 600 kg m^{-3} (Domine et al. 2011).

High snowpack densities were observed to restrain temperature-gradient metamorphism for two main reasons. First, dense snow has a high thermal conductivity, so heat gets easily transmitted through the snowpack, preventing the establishment of a strong temperature gradient. Second, as grains are densely compacted, there is only limited room for grain growth which inhibits the formation of large faceted crystals and depth hoar. However, although Arctic tundra snowpacks are often dense, because meteorological conditions are often windy, layers of faceted grains and depth hoar form in autumn when the soils are still warm and strong temperature gradients establish in thin snowpacks (Domine et al. 2007). Later in the season snow layers do not metamorphize as much because snowpacks are thicker and soils have cooled which greatly weakens temperature gradients. This forms the typical two-layered structure often found in tundra snowpacks: a basal depth hoar layer overlain by wind-packed snow layers.

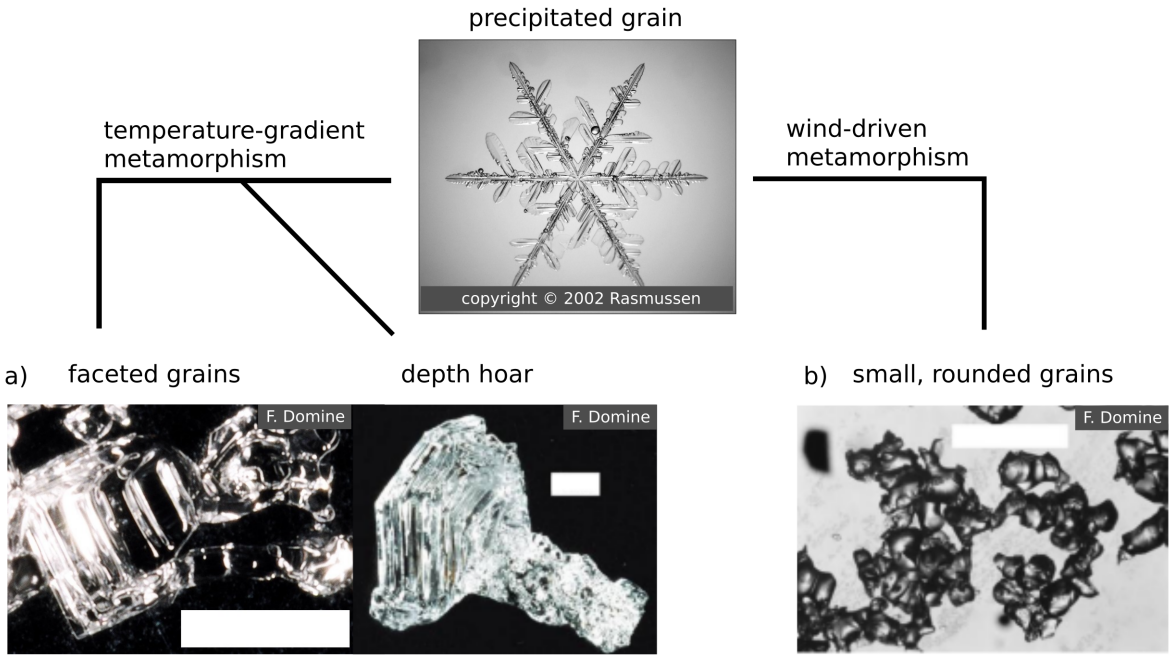

Figure 1.4. Shape of snow grains after metamorphism. White scale bars on photographs are 1 mm. a) faceted grains and depth hoar created by temperature-gradient metamorphism. b) small, rounded grains created by wind-driven metamorphism.

1.2.2 Snow-light interactions

A snowpack is made up of a collection of snow grains and air-filled voids (for now, let's assume that there are no impurities). When a light beam travels through a snowpack and encounters a snow grain, energy is removed from the beam, either by absorption when it passes through a snow grain, or by scattering when crossing an air-grain boundary (Figure 1.5). In the visible and near-infrared spectrum, snow is a highly scattering medium, so most snow-light interactions are scattering events. On the scale of an individual snow grain, light is mostly scattered forward (Figure 1.5), meaning that the probability for light to continue its propagation within 5–10 degrees of the forward direction after a scattering event is high (Figure 1.6; Warren 1982). In contrast, a Lambertian surface scatters light homogeneously in all directions and backwards scattering transmits light in the direction opposite to the incoming one (Figure 1.6). Because each snow grain in the snowpack scatters light forward, light penetrates profoundly into the snowpack and experiences multiple scattering events, before it is finally absorbed or, more likely, re-emerges at the surface. Each scattering event changes the light direction so the path that light travels before exiting the snow surface is long (up to several meters for pure snow with no impurities) (Picard et al. 2016). Snow-light interactions are hence not limited to the surface but are the result of multiple interactions with snow grains within the snowpack. As a rule of thumb, it is assumed that most interactions important for snow albedo occur in the upper 10–20 centimeters of the snowpack (Grenfell 2011, France et al. 2011). However, measured vertical irradiance profiles showed that significant light intensities exist down to 40 cm, and it is only at depths >40cm that light intensity becomes too weak to be measured (Tuzet et al. 2019).

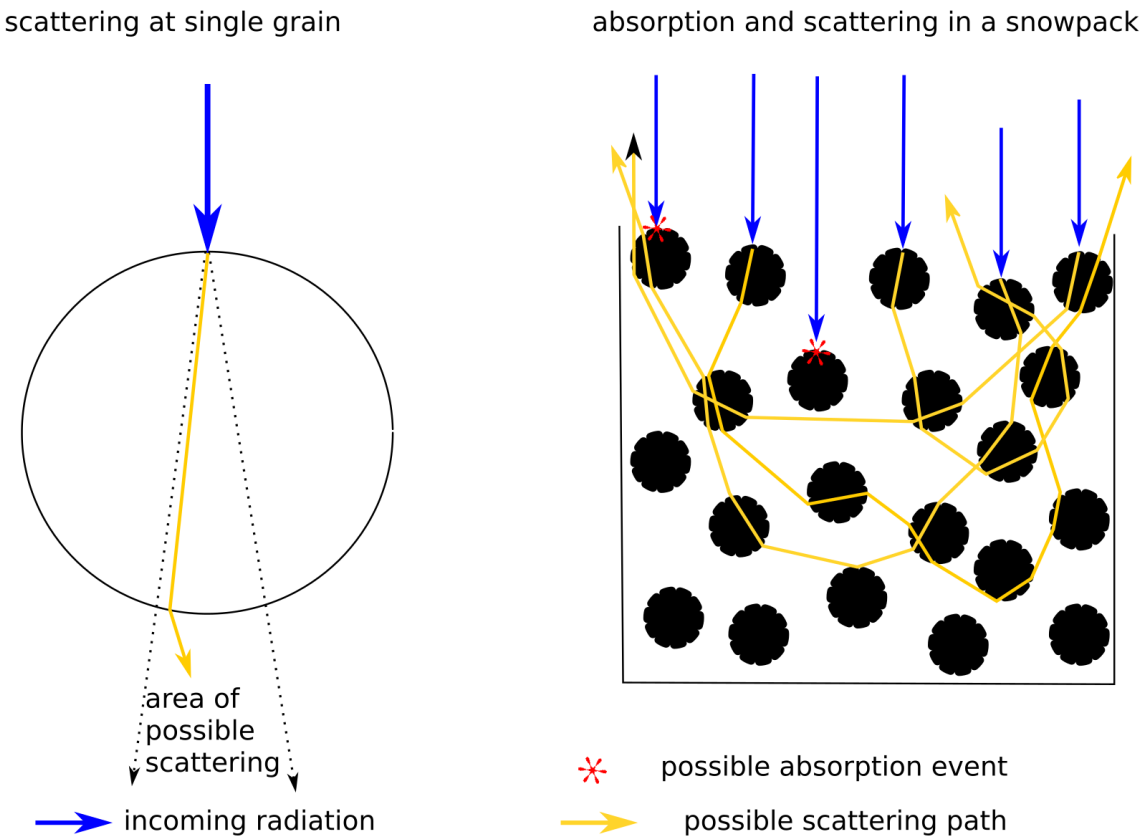

Figure 1.5. Sketch of light scattering at a single grain (left) and of scattering and absorption within a snowpack (right). The yellow arrow on the left shows one possible path light takes within the area of scattering for a single grain. The yellow arrows on the right side show possible paths that incoming light can take when penetrating the snowpack before re-emerging at the surface.

In contrast to scattering, light absorption by snow in the visible and near-infrared spectrum is weak and strongly wavelength dependent. Absorption happens when light travels through a snow grain, which consists of ice, and absorption behavior is thus controlled by the ice absorption coefficient. Ice absorption coefficients have been estimated from light transmission measurements (Warren and Brandt 2008, Picard et al. 2016) and show a strong wavelength-dependence. In the visible spectrum (350–780 nm), light absorption by snow is low, with a minimum value of ~10^{-2} m^{-1} at 400–450 nm (Picard et al. 2016), from which point on light absorption increases continuously from 450 nm to the near infrared (Figure 1.7a). The ice absorption coefficient is responsible for the main spectral features of snow albedo: at minimal ice absorption, between 400 and 450 nm the albedo is close to 1 – light is almost entirely scattered. From 450 nm to the near infrared, absorption increases and

albedo decreases continuously (Figure 1.7b, black curve) (e.g. (Grenfell and Maykut 1977).

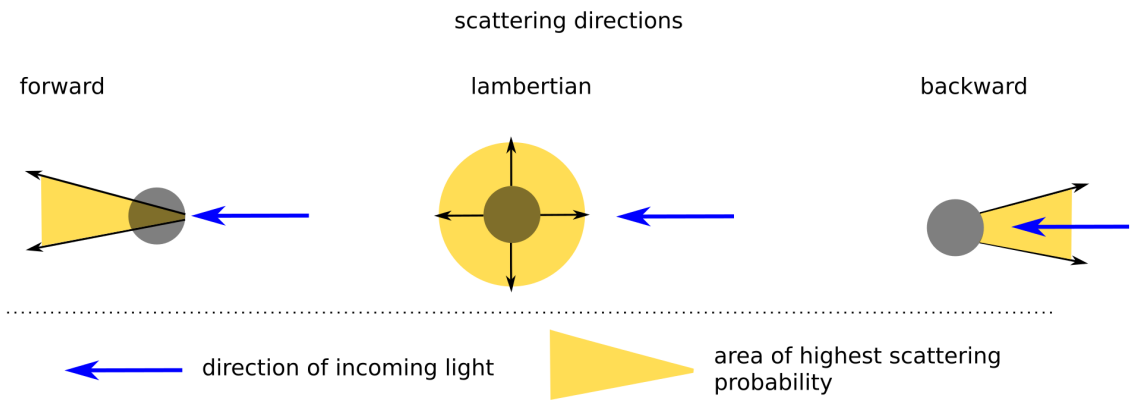

Figure 1.6. Sketch of different scattering behaviors. Snow has a strong forward scattering.

In addition to the ice absorption coefficient, snow albedo is also a function of the macroscopic properties of the snowpack and the spectral composition and direction of incoming radiation. In particular, deviations from the typical curve of snow albedo (Figure 1.7b, black curve) are caused by variations in snow physical properties or the presence of light-absorbing impurities in the snowpack. External factors, like changing cloud cover and solar zenith angles, affect spectral and broadband albedo values by modifying the spectral composition or direction of incoming light. These effects are detailed in the next section.

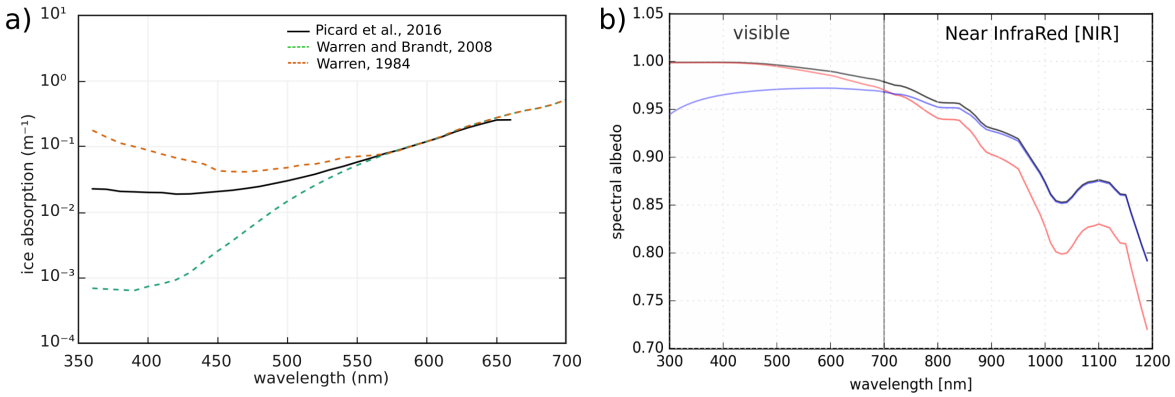

Figure 1.7. a) measured absorption coefficient for ice (from Picard et al. 2016). b) typical albedo curve for a pure snow surface (black), a pure snow surface with large grains (red) and a snow surface with impurities (blue) as calculated with snow radiative transfer model TARTES.

1.2.2.1 Albedo changes induced by snow physical properties

Snow specific surface area (SSA)

It has long been known that the size and shape of snow grains have an important impact on broadband albedo (350–1000 nm) (e.g. Grenfell and Maykut, 1977, Warren 1982, Gallet et al. 2009, Picard et al. 2012). However, determining snow grain size is difficult, because snow particles in nature have a variety of non-spherical shapes and measuring their maximal extent with handlens or binoculars is subject to large uncertainties. In more recent studies, the specific surface area (SSA) of the snowpack has been used as an alternative to grain size (Legagneux et al. 2002, Libois et al. 2013). SSA is the surface area of the snow-air interface per mass unit, and it is expressed in square meters per kilogram (m^2 kg^{-1}). High SSA values indicate a fine-grained snow layer with a high surface-to-mass ratio, while low SSA values indicate a coarse-grained snow layer. SSA is proportional to the optically effective diameter of snow d_{eff}, and it can thus be used to calculate albedo in models or to study the interaction between grain size and albedo. SSA and d_{eff} are related by:

$$SSA = 6 / \rho_{ice} d_{eff}, \quad (1.1)$$

where ρ_{ice} is ice density (=917 kg m^{-3}). *In situ* measurements and simulations showed that high SSA values correspond to high albedo values, and low SSA to low albedo values (Gallet et al. 2009).

SSA in natural snowpacks varies widely both temporally and spatially because of snow metamorphism and this, in turn, causes albedo of snow surfaces to be highly variable as well. High SSA values (~150 m^2 kg^{-1}, Domine et al. 2007) and high broadband albedo (0.85 in the range 350–1000 nm) are associated to fresh, dendritic snow which consists of delicate and thin grains and has thus a very high surface-to-mass ratio (Grenfell and Maykut, 1977). Once snow grains are deposited they start to transform, and SSA and albedo decrease. Lowest SSA and albedo values were found for melt-freeze layers with SSA ~2 m^2 kg^{-1} (Domine et al. 2007) and broadband albedo as low as 0.6 (integrated in the spectrum 350–1000 nm) (Grenfell and Maykut, 1977). A change in albedo of 20 % has a considerable influence on the surface energy budget because the amount of incoming solar energy is important (several hundreds of W m^{-2} during daylight hours).

The magnitude of the SSA-impact on albedo is wavelength-dependent (O'brian and Munis 1975, Warren, 1982). It is more pronounced in the near infrared, but negligible for the visible spectrum (Figure 1.7b, red curve). For low SSA, and associated large grains, the pathlength of a photon through the grain is prolonged compared to small grains. This path-prolongation increases the probability of absorption for a photon which crosses the large grain, an effect which is more important in the near infrared where ice has higher absorption coefficients. In the visible, ice absorption is very weak and the effect of a longer path is thus neglectable.

Impurities

Impurities like black carbon (BC) and mineral dust are often found to be mixed in snowpacks in nature (Wiscombe and Warren 1980, Grenfell et al. 1994, Grenfell and Light 2002, Doherty et al. 2010). The absorption coefficients of light-absorbing impurities are much higher than those of ice in the visible spectrum and moderately higher in the NIR. The significantly higher absorption in the visible spectrum results in a strong reduction of albedo but this effect is weaker or even undetectable in the NIR (Figure 1.7b, blue curve) (Wiscombe and Warren, 1980). Note that impurities are usually fine particles that are evenly-distributed in a snow layer and their effect is expected to be different from that of erect vegetation like shrubs.

1.2.2.2 Albedo changes induced by external factors

To accurately interpret albedo measurements, the effect of external factors must also be considered. For clear sky conditions, snow albedo depends on the solar zenith angle (SZA). Albedo is comparatively low when SZA is low (i.e. when the sun is high in the sky) and increases with increasing SZA (i.e. when the sun approaches the horizon). This effect is explained by the forward scattering behavior of snow grains. Because scattering events are closer to the surface for grazing angles, light re-emerges more rapidly and the path that light travels in the snowpack before reaching the surface is shorter (Figure 1.8). As mentioned above, absorption occurs when light passes through grains, therefore, shortening the light path through the snowpack also reduces the probability of absorption and increases albedo (Warren, 1982). This effect is only relevant for clear skies when most incoming light

is directional.

For overcast conditions, clouds scatter and absorb light before it reaches the snow surface. The consequence of scattering in clouds is that incoming light during overcast conditions is diffuse (i.e. incoming from all directions). The effective zenith angle for purely diffuse light was found to be about 50° (Wiscombe and Warren, 1980). Thus clouds cause albedo to increase for SZA < 50° and to decrease for SZA > 50°, albedo variations which are negligible in the visible but important in the near infrared (Wiscombe and Warren, 1980, Warren 1982). The absorption in clouds modifies the spectral distribution of incoming radiation at the snow surface. Clouds shift the spectral distribution of radiation towards the visible spectrum causing an increase in broadband albedo that covers the visible and near-infrared spectrum (Grenfell and Maykut 1977, Wiscombe and Warren 1980). The spectral shift occurs because, like snow, clouds absorb radiation in the near-infrared spectrum whereas radiation in the visible spectrum is mostly scattered and re-merges from the cloud to the Earth's surface.

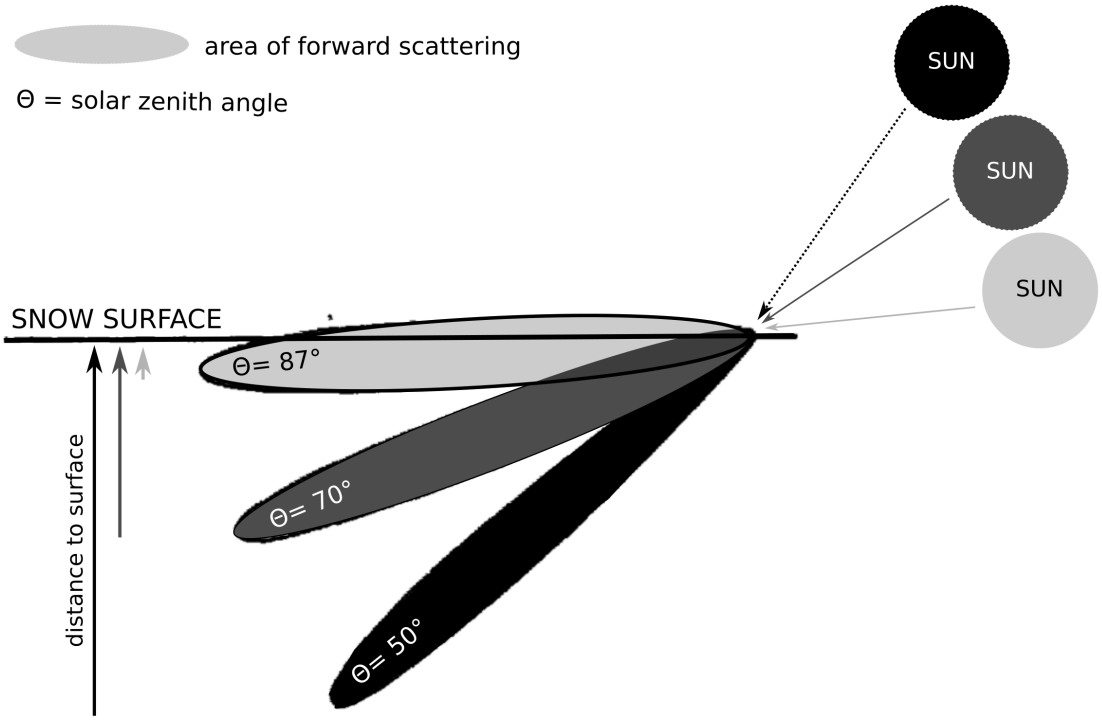

Figure 1.8. Modified sketch from Warren (1982) of the impact of the Solar Zenith Angle (SZA). The deeper penetration at low SZA increases the pathlength in the snow, therefore increasing the probability of absorption and decreasing albedo.

1.3 Shrub-induced changes in winter surface albedo

As mentioned in section 1.3.1, the ongoing expansion of shrubs in the Arctic tundra is expected to have far-reaching consequences on surface albedo and the winter radiation budget. Three shrub-induced processes affect the winter radiation budget: 1) the darkening of bright snow surfaces, 2) the increase of light absorption inside the snowpack by buried branches, and 3) changes in snow albedo through shrub-snow interactions.

1. Surface darkening by protruding branches

The first and most obvious change in albedo is caused by surface darkening. Shrubs have a significantly lower broadband albedo than snow (0.1–0.4 vs. 0.6–0.85 in the spectral range 350–1000 nm), therefore when they protrude above the snow in autumn and spring, they mask the high reflectivity of snow and reduce the surface albedo. Ground-based measurements, remote sensing and modeling studies in Yukon (Pomeroy et al. 2006, Bewley et al. 2010), the Northwest Territories (Marsh et al. 2010), Alaska (Sturm et al. 2005), northern Scandinavia (Cohen et al. 2013) and the pan-Arctic (Loranty et al. 2011) have all shown that shrub branches above snow decrease the surface albedo, sometimes by up to 30 %. Consequences of the surface darkening are changes in the radiation budget and associated increases in air and soil temperatures.

Several modeling studies have quantified the effect of shrub-induced albedo reductions on the tundra's radiation budget and on air and soil temperatures (e.g. Strack et al. 2007, Lawrence and Swenson 2011, Bonfils et al. 2012). Strack et al. (2007) estimated the changes in the energy budget in Alaska from May to June caused by a 50 % increase in shrub expansion for 1 m tall shrubs. They found that this could increase net radiation at the surface by 28 W m^{-2}, heating the atmosphere by 6K. Bonfils et al. (2012) simulated year-round changes in the net radiation budget as well as in air and soil temperatures caused by an increase in small (0.5 m) and tall (2 m) shrub abundance. They found tall shrubs (2 m) responsible for an additional absorption of up to 45 W m^{-2} and low shrubs (0.5 m) up to 25 W m^{-2} of solar radiation. This leads to an average increase in annual soil temperature north of 60°N of 1.84K for tall and 0.66K for short shrubs and an increase in air temperature of 2K and 4K, respectively. These simulations show that shrub-induced albedo reductions

potentially have large impacts on Arctic temperatures and climate. Shrubs may also accelerate permafrost thawing and snow melting by significantly increasing air and soil temperatures. This would then increase the strength of the permafrost and snow-albedo feedbacks, resulting in accelerated global warming.

The main problem of all those modeling approaches is that the parametrization used to calculate albedo of mixed surfaces is rather basic and has not yet been properly validated due to a lack of field data on shrub architecture and on albedo of mixed surfaces. Apart from the lack of robust validation, the current modeling parameterization also neglects the effect of buried branches and of near-surface snow-shrub-light interactions.

2. The effect of buried branches

The influence of shrubs is not limited to branches protruding above the snow because incoming radiation penetrates the snowpack and buried branches may thus also interact with incoming radiation. Buried branches contribute to the snowpack darkening by reducing surface albedo further (in addition to protruding branches), but they can also impact the thermal regime of the snowpack. The absorbed radiation is mostly transformed into heat, warming branches and the snow in their vicinity causing an overall temperature increase in the snowpack. This snowpack warming can then accelerate snow melting and in turn affect the magnitude of the snow-albedo and permafrost feedbacks. Additionally, snowpack warming can modify the temperature gradients within the snowpack and influence snow metamorphism (c.f. section 2.1) and snow physical properties.

3. Near surface snow-shrub interactions

Finally, shrubs can impact snow albedo by modifying snow SSA through near-surface (0–10 cm) snow-shrub interactions. These modifications are complex, can have opposite impacts and depend on meteorological conditions. During windy conditions, protruding branches trap small-grained wind-blown snow with high SSA, which accumulates in small snow mounds around shrubs and increases snow depth (Roche and Allard 1996, Sturm et al. 2000, Domine et al. 2016, Barrère et al. 2018). Field observations of Sturm et al. (2000) showed that branches trapping snow can increase snow depth by as much as 35 cm and that

the effect of increased snow depth can, in some cases, be observed up to 10 m downwind of shrubs. Because wind-blown snow has small grains and high SSA, it has also very high albedo. On the other hand, during warm spells the presence of shrubs increases snow melting because protruding and buried branches warm the atmosphere and the snowpack. When temperatures drop after these warm spells, snow refreezes and forms large melt-freeze crystals, with low SSA and low albedo. These shrub-induced modifications in snow albedo will have corresponding impacts on the snow-albedo feedback.

To our knowledge, neither the effect of buried branches nor the shrub-induced effects on snow albedo have been studied. Therefore, this works aims to investigate all three effects in order to obtain an accurate parameterization for the modeling of albedo of mixed surfaces.

1.3.1 Parameterizing albedo of mixed surfaces

Mixed surfaces have three characteristics that make it difficult to establish a parameterization of albedo. The first one is that mixed surfaces are highly dynamic, the second one is that snow albedo varies constantly as a function of snow physical properties and the third is that snow is translucent and snow-shrub-light interactions are not limited to the surface. The dynamics of mixed surfaces are due to continuous snow accumulation and melting which respectively buries or exposes shrubs. As the amount of protruding branches changes, albedo of the surface changes as well. In order to capture this variability, one would need to continuously monitor and calculate mixed surface albedo and other necessary parameters throughout an entire season. Given the remote location of the Arctic, this can be logistically infeasible and models often rely on limited data to estimate albedo. The second characteristic, the natural variation in snow albedo, means that snow albedo cannot be assigned a constant value but that it has to be recalculated every time snow physical properties change. Most models account for those changes by calculating snow albedo as a function of time, assuming that the small grains of fresh snow grow continuously with time and, consequently, that snow albedo decreases regularly as snow ages. However, this does not necessarily account for the complex snow metamorphism processes in the Arctic tundra. This is particularly true when the metamorphic processes are further complicated by the presence of shrubs. To accurately compute mixed surface

albedo, the dynamics of mixed surfaces needs to be simulated, the variation of snow albedo needs to be implemented, and the effect of buried branches on light absorption needs to be considered.

The common way to parametrize the albedo of mixed surfaces is by using a linear mixing equation (LME). Sturm et al. (2005) were the first to calculate the albedo of snow-shrub surfaces (α_{mix}) with an LME of the form:

$$\alpha_{mix} = (1 - \chi) \cdot \alpha_{snow}(t) + \chi \cdot \alpha_{veg}, \tag{1.2}$$

where α_{veg} is the shrub albedo, α_{snow} is the snow albedo and χ is a weighting factor. Sturm et al. (2005) assumed that α_{veg} is a known, constant parameter and that α_{snow} is a function of time (t). Mixed surface albedo (α_{mix}) was then calculated by using the weighting factor χ to weigh snow and shrub albedo with respect to the fractional surface they each cover.

The main difficulty in using Eq. (1.2) lies in determining accurate weighting factors. This difficulty arises from the dynamics of mixed surfaces due to snow accumulation or melting. As shrubs get buried or exposed, the fractional surface they cover changes resulting in highly variable weighting factors. In Sturm et al. (2005), weighting factors were determined through the analysis of images they had taken in the field. However, this approach is impractical when the LME is to be used in large-scale studies or to simulate albedo for an entire snow season because it would require that images are available for the whole season. In some cases, it might be possible to use satellite imagery, but the acquisition is often complicated by the presence of clouds, especially in the Arctic. Moreover, using image analysis for weighting factor determination prevents the LME to be used in a predictive way.

Liston and Hiemstra (2011) developed an alternative approach where the high temporal variability in χ is modeled as a function of vegetation height and snow depth. More specifically, they determined χ as the product of the (snow-free) vegetation fraction ($\Gamma_{snow-free}$) and the fraction of branches protruding above the snow (f_{exp}):

$$\chi = f_{\exp} \cdot \Gamma_{snow-free}. \tag{1.3}$$

The high temporal variability is accounted for through the fraction of protruding branches (f_{exp}). Liston and Hiemstra (2011) suggest to calculate f_{exp} from shrub height (H_{veg}) and snow depth (H_{snow}) with:

$$f_{\exp} = 1 - \left(\frac{H_{snow}}{H_{veg}} \right)^{d}, \tag{1.4}$$

where d is a shape factor indicating the shape of shrubs. In Liston and Hiemstra (2011) shrubs are assumed to have a parabolic shape and d is set to 1.

The advantage of the approach of Liston and Hiemstra (2011) is that the fraction of protruding branches (f_{exp}) can be continuously calculated for an entire snow season if snow depth and shrub height values are available. Snow depth values are usually calculated in climate and land surface models as a function of meteorological and topographical data. Shrub height is assumed to be constant and is determined from summer field measurements. However, a limitation of Liston and Hiemstra's (2011) approach is the uncertainty concerning the value of the shape factor d (Eq. 1.4). This shape factor is set to 1 based on the assumption that shrubs have a parabolic shape. However, there is no information on Arctic shrub architecture and this assumption therefore remains unverified. A second problem in Eq. (1.4) is that shrub size is assumed to be constant throughout the winter. This, may not always be the case because tall shrubs with small branches (1.3–5 cm in diameter), can bend under heavy snow loads (Sturm et al. 2005, Pomeroy et al. 2006, Marsh et al. 2010, Ménard et al. 2014).

The problem of simulating shrub-bending was addressed by Ménard et al. (2014) who presented a first biomechanical shrub-bending model. Shrub-bending events observed in the field happened fast and could occur overnight. This means that surfaces whose albedo is dominated by shrubs can transform into a highly reflective snow surface within one day, with strong influences on net radiation (Sturm et al. 2005). In spring, the opposite effect happens. During snow melt, branches can suddenly spring up, converting a snow-dominated surface into a shrub-dominated one, with the potential of reducing local broadband albedo from 0.85 to 0.3 (Pomeroy et al. 2006). Ménard et al.'s (2014) shrub-bending model is driven by meteorological data and computes a shrub-bending parameter

(*C*) based on shrub structure and elasticity properties. Ménard et al. (2014) used the bending model to further refine the albedo parameterization of Liston and Hiemstra (2011) by implementing the shrub bending parameter *C* into Eq. (1.4):

$$f_{\exp} = 1 - \left(\frac{H_{snow}}{C \cdot H_{veg}} \right)^{d}. \qquad (1.5)$$

Ménard et al. (2014) could not directly verify the accuracy of their calculated bending parameter *C* nor confirm the improvement provided by Eq. (1.5) as no quantitative field data on shrub architecture was available. Instead, they compared calculated surface albedo values, obtained with Eq. (1.2), Eq. (1.3) and Eq. (1.5), with measured albedo values. The fit between the two albedo values was used as a proxy to verify the accuracy of *C* and Eq. (1.5). Their root mean square errors lie between 0.07 and 0.2, showing that the model works well for some sites but less so for others. This highlights the need to better understand the sources of variability affecting the model's error.

In addition to the shape factor *d*, other potential error sources are the simplified representation of snow albedo of snow mixed with shrubs, the light absorption by buried branches and the uncertainty pertaining to the determination of the (snow-free) vegetation fraction $\Gamma_{snow\text{-}free}$. The latter is required as input in Eq. (1.3) and is often determined from Leaf Area Indexes (LAI) or, more rarely, from Branch Area Indexes (BAI). LAI values are available from satellite or remote sensing data, but they may not be representative of winter conditions when shrubs have no leaves. In this case, BAI values are more precise but literature on BAI is poor and BAI values are rarely available. Moreover, determining BAI from remote sensing data again prevents the mixed surface albedo parameterization to be used in a predictive way. A method to calculate BAI for Arctic shrubs would therefore be more useful.

In most climate and land surface models, mixed surface albedo is calculated by a combination of Eqns.(1,2 and 4), sometimes with and other times without the bending factor *C*. The shape factor *d* is generally set to 1, $\Gamma_{snow\text{-}free}$ is taken from LAI values, snow albedo is either a constant value or a function of time and the effect of buried branches is generally neglected. To my knowledge, the only verification of this approach is the study of

Ménard et al. (2014) who reported that calculated mixed surface albedo had a precision between 7 and 20 %. A change of 20 % in albedo values would have a tremendous influence on the surface energy budget because the amount of incoming solar energy is important (several hundreds of W m^{-2} during daylight hours). A large-scale phenomenon like shrub encroachment in the Arctic which has the potential to increase soil and air temperatures by 2 to 6K (Strack et al. 2007, Bonfils et al. 2012) and which could strongly influence the magnitude of the snow-albedo and permafrost feedbacks should be better quantified.

1.4 Objectives and organization of the thesis

The overarching objective of this work is to develop and validate a method that can accurately simulate the albedo of mixed surfaces in tundra environments. The method needs to be easily implemented into current land surface and climate models and the calculations must be based on easy-to-measure parameters. The development of such a method is essential to quantify the impact of the ongoing shrubification on the surface radiation budget in the Arctic tundra and to estimate the potentially strong positive feedbacks on global climate warming. The method developed here is based on the previous works of Sturm et al. (2005), Liston and Hiemstra (2011) and Ménard et al. (2014). Their parameterizations are developed further in a stepwise approach.

Step 1 (Chapter 2): The first step in this work was to conduct a suitability test in order to verify whether or not a Linear Mixing Equation (LME) with a form as shown in Eq. (1.2) is suitable to calculate mixed surface albedo. For this purpose, mixed surface albedo was computed using Eq. (1.2) and the results were verified with a large dataset of measured spectral albedos. In addition, snow albedo (α_{snow}) was calculated as a function of measured snow physical properties using the snow radiation model TARTES, rather than determining α_{snow} as a function of time. To identify the influence of shrubs on snow albedo, α_{snow} was calculated with physical properties measured at shrub-free sites and at sites with snow and protruding branches. The α_{snow} at shrub-free sites vs. α_{snow} at sites with snow and protruding branches were compared to determine the significance of shrub-induced snow albedo variations.

Step 2 (Chapter 3): A unique dataset on the architecture of *B. glandulosa* shrubs was used to validate Eq. (1.5) and, more specifically, to determine the value of the shape factor *d*. The data on shrub architecture was also used to establish an allometric equation that can be used to compute BAI values from Arctic shrub height. Estimated BAI values can then be used to obtain $\Gamma_{snow\text{-}free}$ in Eq. (1.3). This allometric equation allows using the LME parameterization in a predictive way as BAI values are no longer bound to remote sensing data. Finally, mixed surface albedo calculated with the improved LME approach (using the new value for *d* and the established allometric equation) was validated with a large data set of measured spectral albedo values.

Step 3 – Chapter 4: Step three was dedicated to the study of snow-shrub-light interactions inside the snowpack in order to determine the influence of buried branches on light absorption. For this, irradiance profiles measured in shrub-free snowpacks were used to determine the influence of light absorbing impurities. Then, considering the effect of impurities, the influence of buried branches was investigated in vertical irradiance profiles measured in mixed snowpacks. To our knowledge, this were the first measurements of irradiance in mixed snowpacks and they were used to characterize the influence of buried branches on radiative transfer in snow.

The remainder of this document is structured as follows. Chapters 2, 3 and 4 show the scientific results as indicated in the stepwise approach explained above. To avoid repetition, I did not include an extra chapter about the climatic and environmental conditions at the study site and the experimental data acquisition, because this information is given in the 'Methods' sections of each chapter. The thesis is completed with a general conclusion and an outlook on how the results of this thesis can be put into use and the new scientific questions that result from this work.

Chapter 2

Article 1:
Impact of shrubs on surface albedo and snow specific surface area at a low arctic site: *in situ* measurements and simulations

2.1 Preamble

This chapter presents the first part of our results and has the principle aim to validate the Linear Mixing Equation (LME) as a suitable tool to calculate albedo for mixed surfaces with shrubs and protruding branches. As such, this chapter is the foundation for the next chapter (Chapter 3), where the LME approach is improved.

The results have also been published as scientific article: Belke-Brea, M., Domine, F., Barrere, M., Picard, G., and Arnaud, L. (2020). Impact of shrubs on surface albedo and snow specific surface area at a low arctic site: in-situ measurements and simulations. *Journal of Climate*, https://doi.org/10.1175/JCLI-D-19-0318.1.

2.2 Résumé

Dans l'Arctique, les branches d'arbustes qui percent le manteau neigeux modifient l'albédo de la surface, et pourraient ainsi affecter la fonte et les propriétés isolantes de la neige. Nous avons mesuré l'albédo spectral (400-1080nm) de quatre sites (3 avec arbustes, 1 sans arbustes) près d'Umiujaq (56.5°N, 76.5°W), Canada. Tôt dans la saison nivale, la réduction de l'albédo d'une surface causée par les arbustes varie avec la longueur d'onde et atteint 55% à 500nm et 19 % à 1000nm. Ceci représente 70Wm^{-2} supplémentaires d'énergie

absorbée en moyenne par une surface avec arbustes. Nous avons ensuite simulé l'albédo spectral avec précision à l'aide d'une équation linéaire de mélange (linear mixing equation), et avons obtenu des valeurs très proches de nos observations. Nous concluons que cet outil est approprié pour paramétriser l'albédo de surfaces mixtes dans les modèles climatiques, et recommandons fortement que les surfaces mixtes soient considérées dans les projections climatique futures.

2.3 Abstract

Erect shrubs in the Arctic reduce surface albedo when branches protrude above the snow and modify snow properties and in particular specific surface area (SSA). Important consequences are changes in the land surface-atmosphere energy exchange and the increase of snow melting in autumn, possibly inducing reduced soil thermal insulation and in turn permafrost cooling. Near Umiujaq (56.5°N, 76.5°W) in the Canadian Low Arctic where dwarf birches (*Betula glandulosa*) are expanding, spectral albedo (400–1080 nm) under diffused light and vertical profiles of SSA were measured in November and December 2015 at four sites: three with protruding branches, and one with only snow. At the beginning of the snow season (8 November), shrub-induced albedo reductions were found to be wavelength-dependent and as high as 55 % at 500 nm and 18 % at 1000 nm which, integrated over the measurement range (400–1080 nm), corresponds to 70 W m^{-2} of additionally absorbed energy. The impact of shrubs is not just snow darkening. They also affect snow SSA in multiple ways, by accumulating snow with high SSA during cold windy precipitation and favoring SSA decrease by inducing melting during warm spells. However, the impact on the radiation budget of direct darkening from shrubs likely dominates over the indirect change in SSA. Spectral albedo was simulated with a linear mixing equation (LME) which fitted well with observed spectra. The average root-mean-square error was 0.009. We conclude that LMEs are a suitable tool to parametrize mixed surface albedo in snow and climate models.

2.4 Main text

2.4.1 Introduction

With climate warming, shrubs are expanding on the Arctic tundra, (Tape et al. 2006, Myers-Smith et al. 2011, Ropars and Boudreau 2012) changing its winter surface from undisturbed snow to a mixed surface of snow and protruding branches. This mixed surface has a lower albedo in the visible than undisturbed snow (Sturm et al. 2005, Loranty et al. 2011) positively feeding back on regional and global climate warming (Sturm et al. 2001, Loranty and Goetz 2012). Quantifying the shrub-albedo feedback and its impact on future climate can be done by implementing parametrizations of mixed surface albedo in climate models (Bonfils et al. 2012, Loranty and Goetz 2012, Pearson et al. 2013). A commonly used parametrization is a linear mixing equation (LME) (Sturm et al. 2005, Marsh et al. 2010) where mixed surface albedo α_{mix_calc} is calculated by weighting snow albedo α_{sn} and shrub albedo α_{veg} proportionally to the surface area covered by each:

$$\alpha_{\mathrm{mix\_calc}} = (1 - \chi)\,\alpha_{\mathrm{sn}} + \chi\alpha_{\mathrm{veg}}, \tag{2.1}$$

where χ is a weighting factor. Despite its common application, the performance of this parametrization has only been validated with broadband albedo measurements (Sturm et al. 2005, Ménard et al. 2014) and has never been tested for spectral albedo due to the lack of validation data since, to our knowledge, spectral albedo has never been measured from the ground over mixed surfaces in the Arctic. Multispectral reflectance measurements from satellites are available but their use for testing albedo data is delicate since mixed surfaces are not lambertian.

Shrub albedo spectra, α_{veg}, are easy to obtain because they can be measured directly in the field in autumn after leaf fall but before snowfall and used in winter since branch albedo is consistent throughout the year. However, it is more complicated to determine the snow-only albedo spectra, α_{sn}, in the presence of shrubs because, albedo being hemispherically integrated, the footprint of a sensor inevitably comprises protruding branches and albedo

measurements can thus only record the mixed reflectance of snow and protruding branches. Contact probes could be attempted but they measure directional reflectance rather than albedo (Painter et al. 2007) and their size is often too large for the dense branch network encountered. Measuring α_{sn} over adjacent shrub-free sites is not necessarily a solution because protruding branches can locally modify the physical properties of snow, which in turn affect snow albedo.

The main snow physical property that influences albedo and is affected by shrubs is the snow specific surface area (SSA), which is simply related to the optical grain diameter, d_{opt}, by:

$$\mathrm{SSA}=\frac{6}{\rho_{\mathrm{ice}}\, d_{\mathrm{opt}}}, \tag{2.2}$$

where ρ_{ice} is the ice density, 917 kg m^{-3} at 0°C (Warren 1982, Domine et al. 2007). Snow with larger SSA scatters light more efficiently and thus has a higher albedo, especially in the near-infrared spectrum (750 – 2500 nm) (Warren 1982). Fresh snow has the highest SSA but this parameter changes continuously in space and over time because of snow metamorphism which modifies the size and shape of snow grains (Taillandier et al. 2007).

At the surface, the principal drivers for snow metamorphism are meteorological variables, mostly wind speed and temperature. For air temperatures <0°C, wind accelerates the decrease in SSA of fresh snow (Cabanes et al. 2003), but can increase the SSA of aged snow (Domine et al. 2009). Shrubs reduce wind speed at the ground surface, causing snow to accumulate there (Sturm et al. 2001, Liston et al. 2002, Essery and Pomeroy 2004, Pomeroy et al. 2006, Marsh et al. 2010, Domine et al. 2016). For air temperature >0°C, snow melting leads to very low SSA values (Domine et al. 2007). Melting is accelerated by the presence of shrubs because branches with low albedo absorb light, heat up and emit radiation in the thermal infrared, causing the surrounding snow to melt (Sturm et al. 2005, Pomeroy et al. 2006, Marsh et al. 2010, Barrere et al. 2018). Shrub-induced increases in

snow accumulation and melting likely cause snow SSA, and therefore albedo, in mixed surfaces to be different from that of shrub-free tundra. In those cases accurate α_{sn} spectra can only be obtained by computing them as a function of measured SSA rather than by measuring them over shrub-free sites.

In this study we present the first ground-based spectral albedo measurements (400–1080 nm), taken over mixed surfaces of snow and dwarf birches (*Betula glandulosa*) near Umiujaq, Northern Quebec. We used the measured spectra to determine the suitability of the commonly used LME to simulate spectral albedo of mixed surfaces. We also test the sensitivity of the LME performance to the choice of α_{veg} by using four different input spectra. Finally, we test whether computing α_{sn} as a function of measured SSA improves the performance and accuracy of the LME in predicting albedo compared to simulations where α_{sn} was derived from snow albedo measurements at an adjacent pure snow site. With this study we want to test the suitability of the LME to calculate albedo of mixed surfaces with snow and shrubs and we hope to contribute to a better understanding of the complex shrub-snow-albedo interactions which would allow a more accurate quantification of the shrub-albedo feedback.

2.4.2 Methods

2.4.2.1 Study sites

The research area is located in the low Arctic in the glacier-shaped Tasiapik Valley next to the village of Umiujaq in Northern Quebec (Figure 2.1). An Automatic Weather Station (AWS) records hourly averages of meteorological variables in the valley since 1997. The mean annual air temperature (1997 – 2015) is -3°C (CEN 2016). Snow storms are frequent from October until December, and wind speeds can reach 22 m s^{-1} during these events. For the 2012-15 period, around 20 % of recorded wind speeds exceeded 5 m s^{-1} (CEN 2016), the approximate threshold for snow drifting (Vionnet et al. 2013).

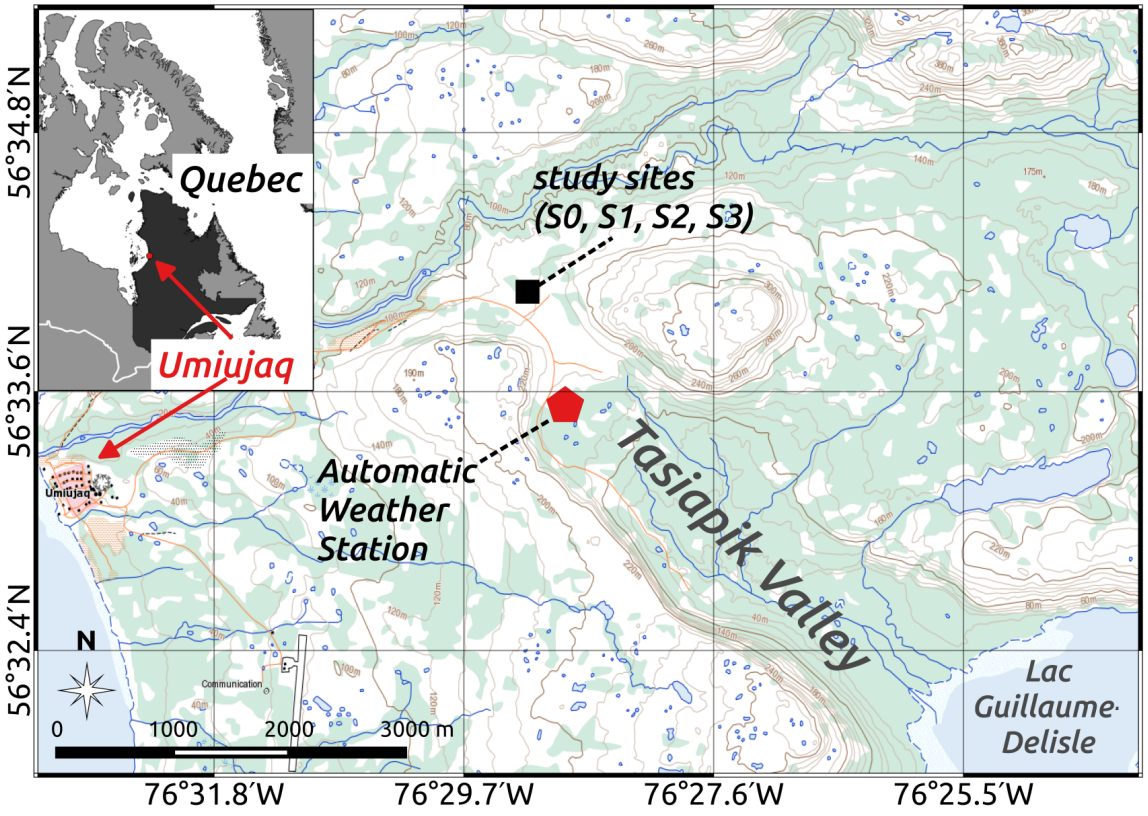

Figure 2.1. Location of study sites and automatic weather station in the Tasiapik Valley near Umiujaq in Northern Quebec, Canada. Map source: Natural Resources Canada (http://atlas.gc.ca/toporama/en/index.html).

The Tasiapik Valley lies in the forest-tundra ecotone (Payette, 1976) which is characterized by trees in wind-sheltered depressions and lichen and shrubs of varying height covering the wind-exposed uplands (Grégoire and Bégin, 1993). The main shrub species are dwarf birch (*Betula glandulosa*) and willow (mostly *Salix glauca* and *S. planifolia*), which have been expanding and replacing lichen patches of mostly *Cladonia spp.* in the last decade (Ropars and Boudreau 2012, Provencher-Nolet et al. 2014). For this study, we selected four sites located on the upper part of the Tasiapik Valley (Figure 2.1). The first (S0) is a lichen site and the three others are characterized by *Betula glandulosa* shrubs of different heights: ~36 cm (S1), ~80 cm (S2) and ~120 cm (S3). The four sites lay within 50 m of each other and had similar topographical and meteorological conditions.

2.4.2.2 Experimental methods

Field work took place during two campaigns, one in late summer (September) and one in autumn (late October to December) 2015. The late summer campaign was conducted to acquire spectral albedo over shrubs (α_{veg}) before the start of the snow-season but after most leaves had already fallen. Later, during the autumn campaign, we designated the four study sites (S0 in lichen and S1-S3 in shrubs) where we measured time series of spectral albedo (α_{sn_obs} at S0 and α_{mix_obs} at S1-S3). We also measured SSA for snow albedo computations (α_{sn_TARTES}) for which we used the snow radiative transfer model TARTES (Libois et al. 2013).

Spectral albedo measurements

Spectral albedo was calculated as the ratio of spectral reflected over incident radiation which were measured with the Solalb instrument. Solalb is a simpler and mobile version of the Autosolexs instrument described in Picard et al. (2016b). Basically it consists of a cosine light collector, which is attached to one end of a 2 m long, rotatable metallic arm. Incident and reflected radiation are captured by orienting the metallic arm towards the sky and towards the ground, respectively. However, since they are not measured simultaneously, incoming radiation can fluctuate during the acquisition period, particularly during overcast conditions. Fluctuations were monitored by a photodiode and measurements for which fluctuations exceeded 1 % were discarded. The leveling of the instrument during data acquisition is critical within 0.2° and was measured by an electronic inclinometer attached close by the cosine collector. Radiation was captured by the light collector, and transmitted through an optical fiber to a MayaPro spectrometer from Ocean Optics® which has an effective resolution of 3 nm and a spectral range from 200 to 1120 nm. However, we only used the 400 to 1080 nm range because data in 200 to 400 nm and 1080 to 1120 nm ranges had a low signal-to-noise ratio and were discarded. A first order butterworth filter was applied to all spectra to remove variations with intensity amplitudes of 0.05 or lower. The butterworth filter was provided by the Python scipy.signal.butter function and used with a cutoff frequency of 0.05.

A detailed description of the design and characterization of the home-built Solalb's light collector can be found in Picard et al. (2016b). It is important to note that the collector's

response for radiation with a zenith angle >70° introduces an uncorrectable error of ±15 % to the measurements (Picard et al. 2016b). This is problematic because in the Arctic, in autumn and winter, solar zenith angels (SZA) are generally larger than 70°. In order to avoid such errors, measurements were only taken during overcast conditions, when radiation is coming from every direction in the sky, and with a maximal contribution around 45° in zenith angle, a range where the cosine collector is excellent. These conditions also greatly limit the impact of the surface slope (Wei-Liang Lee et al. 2011).

SSA measurements

Snow SSA was measured together with spectral albedo at each of the four study sites. It was measured in the upper 10 cm of the snowpack along vertical profiles with a 1 cm resolution using the DUFISSS instrument detailed in Gallet et al. (2009). Briefly, infrared reflectance of snow samples is measured at 1310 nm using an integrating sphere and SSA is calculated from that reflectance with a fairly simple algorithm.

In order to model snow albedo of a multilayer snowpack with TARTES, it is necessary to know the snow density profiles in addition to the SSA profiles of the snowpack (Libois et al. 2013). However, density could not be measured in the field due to short measuring days and harsh measuring conditions. Instead, based on 5 years of simultaneous measurements of density and SSA at this site, we determined an SSA-density correlation for surface snow, similar to the approach of Domine et al., (2007) which we used to estimate density. The correlation is shown in Figure 2.2.

Albedo calculations from SSA measurements

TARTES is a radiative transfer model which allows the determination of snow albedo of a multi-layered snowpack with known snow physical properties (Libois et al. 2013). It is available from https://pypi.org/project/tartes/. We use the updated ice absorption spectrum from Picard et al. (2016a) which is higher in the visible range than in Warren and Brandt 2008. Every snow layer with a given thickness is characterized by its SSA, which we measured, and by snow density, which was determined with the empirical correlation shown in Figure 2.2. Layer thickness was set to 1 cm, the resolution of the SSA profiles,

except for the bottom layer which was set to 1000 cm to exclude influence of underlying soil. Illumination conditions were set to 100 % diffuse.

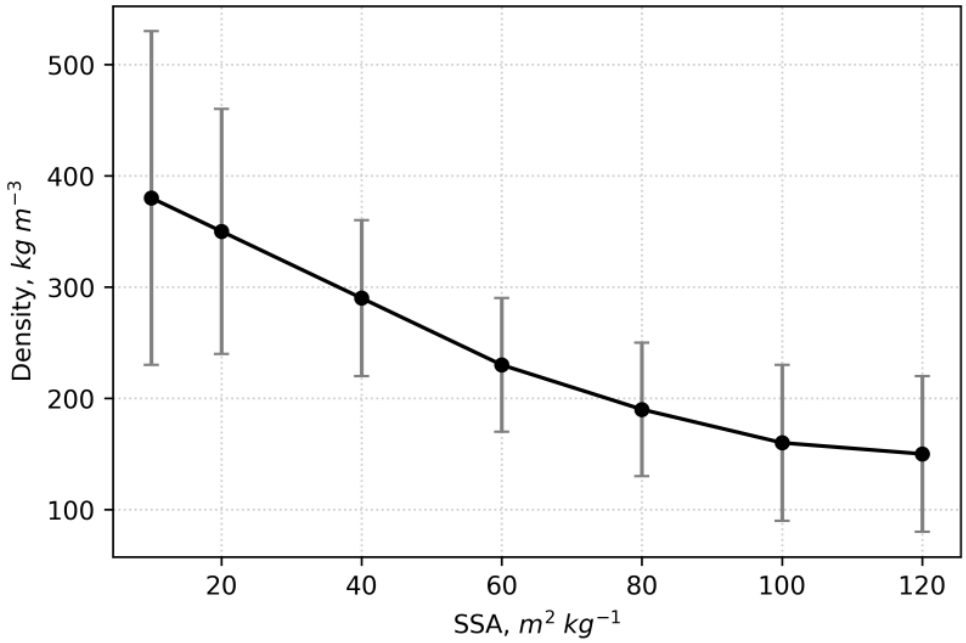

Figure 2.2. Empirical correlation of snow density and SSA for surface snow based on 5 years of snow measurements near Umiujaq.

2.4.2.3 Measured albedo correction

The comparison between measured and simulated albedo can be biased because measured albedo is often subject to artifacts such as variations in illumination, shadows cast by the instrument and operator, slopes of the surface, etc. To account for these wavelength-independent artifacts, we followed the approach of Picard et al. (2016b) and introduced a free, wavelength-independent scaling factor *A* which was used to correct observed albedo (α_{mix_obs}):

$$\alpha_{\text{mix\_obs, corr}}(\lambda) = A^{-1}\alpha_{\text{mix\_obs}}(\lambda). \quad (2.3)$$

The scaling factor *A* was obtained by calculating a theoretical, artifact-free snow albedo (α_{sn_TARTES}) for the pure snow site S0 using measured SSA, estimated density (see Figure 2.2)

and the radiative transfer model TARTES. *A* was retrieved by fitting α_{sn_TARTES} and α_{sn_obs} using a linear least squares method (provided by the Python scipy.optimize.least_squares function), which minimizes the squared difference between α_{sn_TARTES} and α_{sn_obs}. Assuming *A* is the same for all measurements taken on a given day, the values retrieved for S0 can then be used to correct the observed spectra at shrub sites S1-S3.

2.4.2.4 Simulating mixed surface albedo with a Linear Mixing Equation (LME)

To investigate the suitability of the LME (Eq. (2.1)) to simulate mixed surface albedo (α_{mix_calc}), we designed a modeling approach where we consider α_{sn} and α_{veg} to be known parameters and the proportion parameter χ to be adjustable. The best-fitting χ is retrieved by matching α_{mix_calc} to the corrected spectra measured at the shrub sites ($\alpha_{mix\_obs,\ corr}$). The fit is performed with a linear least squares method and the performance of the LME is assessed by determining the fit quality between α_{mix_calc} and $\alpha_{mix\_obs,\ corr}$, i.e. the root-mean-squares error (RMSE).

The performance of the model was tested for four α_{veg} spectra. The first was an average of five measurement taken with Solalb near Umiujaq during the summer campaign in 2015 over dwarf birches (*Betula glandulosa*) with various understories, i.e. moss, lichen and dead leaves (Appendix A, Figure A1). The average has a low maximal standard variation of 0.01 in the visible (400–750 nm) and 0.02 in the near infrared (750–1080 nm) suggesting that different types of understory had little influence on albedo. In addition to the Umiujaq spectrum (α_{veg_umi}), we used two spectra from Juszak et al. (2014) who employed a contact probe to measure branch reflectivity of young (α_{veg_y}) and old (α_{veg_o}) dwarf birches (*Betula nana*) in Siberia. For the fourth spectrum, we calculated the average of α_{veg_y} and α_{veg_o} to obtain a mixed reflectivity of young and old branches (α_{veg_y+o}). Figure 2.3 depicts the four different spectra.

To calculate α_{sn} in mixed surfaces with TARTES we had to make the following assumptions: (1) SSA at each site is relatively homogeneous and the measured profiles are therefore representative for the entire area of the site. (2) Snow SSA and density are

correlated, so the profile of the latter can be deduced from the measured profiles of SSA (Figure 2.2). (3) The impurity content is negligible and assumed to be zero. (4) Illumination conditions were always 100 % diffuse. These assumptions allow calculating a theoretical albedo α_{sn_TARTES} for each shrub site and day of albedo measurements.

An alternative approach is to use snow albedo measured over shrub-free surfaces and to simply assume that snow albedo in mixed and pure snow surfaces resemble each other enough to be considered the same. To test this second approach, an additional simulation was run with the measured snow albedo from the S0 lichen site (α_{sn_obs}).

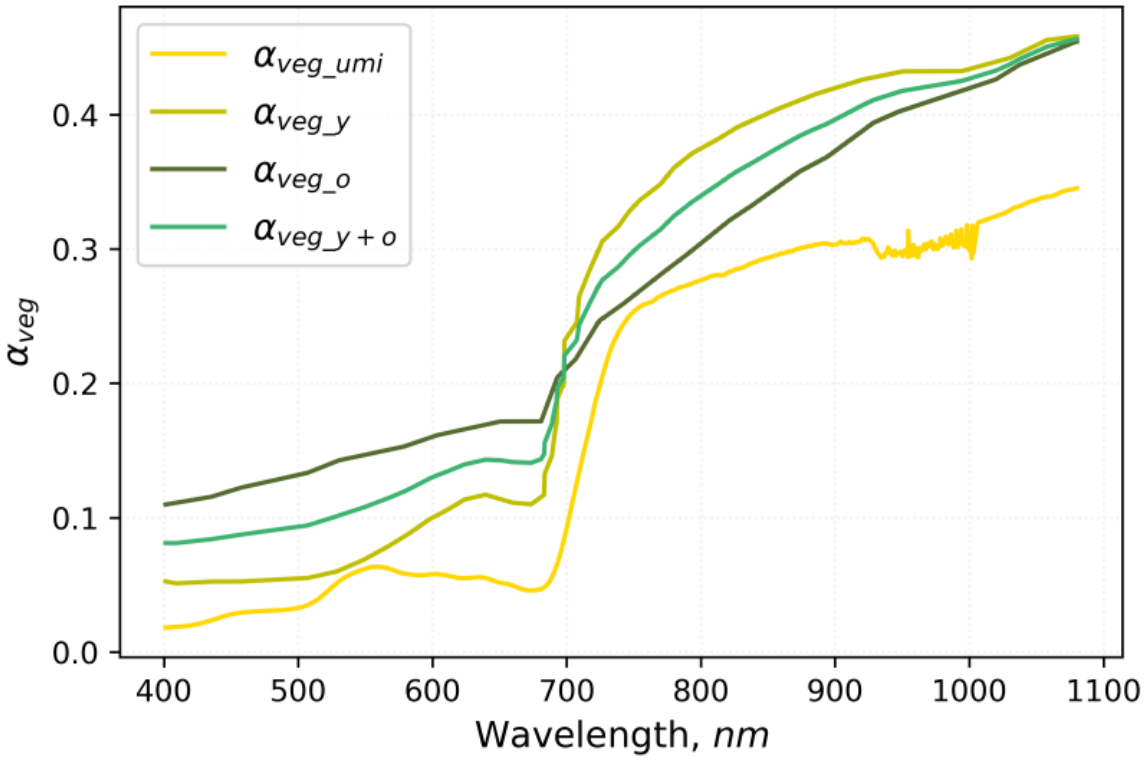

Figure 2.3. Four shrub albedo spectra used as α_{veg} input parameter for simulations with the LME (Eq. (2.1)). The spectra include (1) the average of five albedo spectra measured in late summer 2015 near Umiujaq (α_{veg_umi}) over Betula glandulosa shrubs, (2) two measurements conducted by Juszak et al. (2014) with a contact probe in Siberia for young (α_{veg_y}) and old (α_{veg_o}) branches of Betula nana shrubs and (3) one average spectra of Juszak's young and old branch spectra (α_{veg_y+o}).

2.4.3 Results

2.4.3.1 Spectral albedo of mixed and pure snow surfaces

Adding up the four study sites we obtained 44 valid spectral albedo measurements. Representative spectra for each site are shown in Figure 2.4 for 8 November, 22 November and 2 December. Over that period, snow depth at S2 and S3 increased from around 40 to 69 cm (S2) and 79 cm (S3), decreased slightly from 35 to 24 cm at S1 and remained steadily around 20 cm at S0 (Table 1). Shrub-induced albedo decreases were wavelength-dependent and more pronounced in the visible spectrum than in the near-infrared spectrum (Figure 2.4). For example, on 8 November, the albedos at 500 nm for S0 and S3 were 0.92 and 0.37, respectively, representing an albedo reduction of 55 %. On the other hand, at 1000 nm measured albedo was 0.69 for S0 and 0.51 for S3, representing a reduction of only 18 %. Albedo in the visible at S2 and S3 increased gradually in the time span from 8 November to 2 December. On 2 December, albedos in the visible at all sites were still within 10 % meaning that the formation of a highly reflective pure snow surface at S2 and especially at S3 was delayed by more than a month compared to the lichen site S0. Comparing S1 and S0, spectra were within 6 % throughout the study showing that small shrubs of ~36 cm had a limited effect on albedo.

Table 2.1. Snow depth in cm at the lichen site S0, small shrub site S1 (~36 cm), the medium shrub site S2 (~80 cm) and the tall shrub site S3 (~120 cm). Snow depth was measured with a snowprobe.

Date	S0	S1	S2	S3
08 Nov. 2015	15	35	40	44
22 Nov. 2015	21	29	56	65
02 Dec. 2015	15	24	69	79

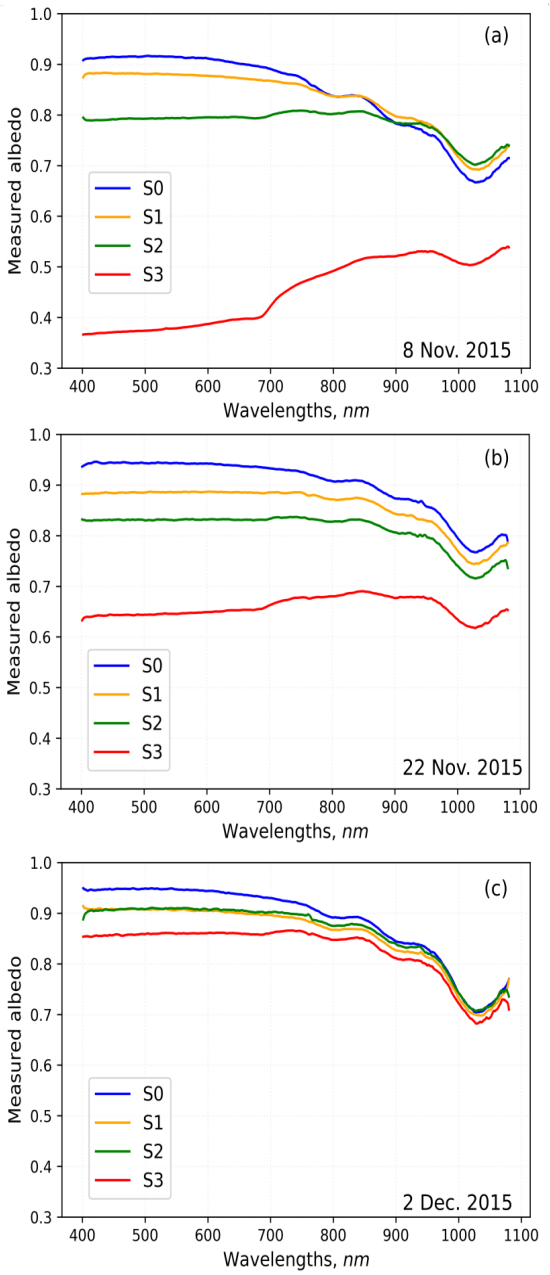

Figure 2.4. Comparison of spectral albedo measured in Umiujaq on 8 Nov. (a), 15 Nov. (b) and 22 Nov. (c) 2015 at four different sites (S0 - S3). S0 is a lichen site with a pure snow surface, S1-S3 are shrub sites with shrubs of different heights: ~36 cm (S1), ~ 80 cm (S2) and ~ 120 cm (S3).

2.4.3.2 Shrub-snow-SSA interactions under different meteorological conditions

Weather in autumn 2015 was characterized by strong winds, warm spells or a combination of both, as detailed in Barrere et al. (2018). During those meteorological conditions shrubs had a visible effect on the surface snow layer (Figure 2.5). Warm spells caused extensive snow melting around protruding branches (Figure 2.5a) while windy conditions caused the

preferential accumulation of wind-blown snow around shrubs, forming distinct snow mounds (Figure 2.5b) whereas shrub-free areas retained a hard and icy surface.

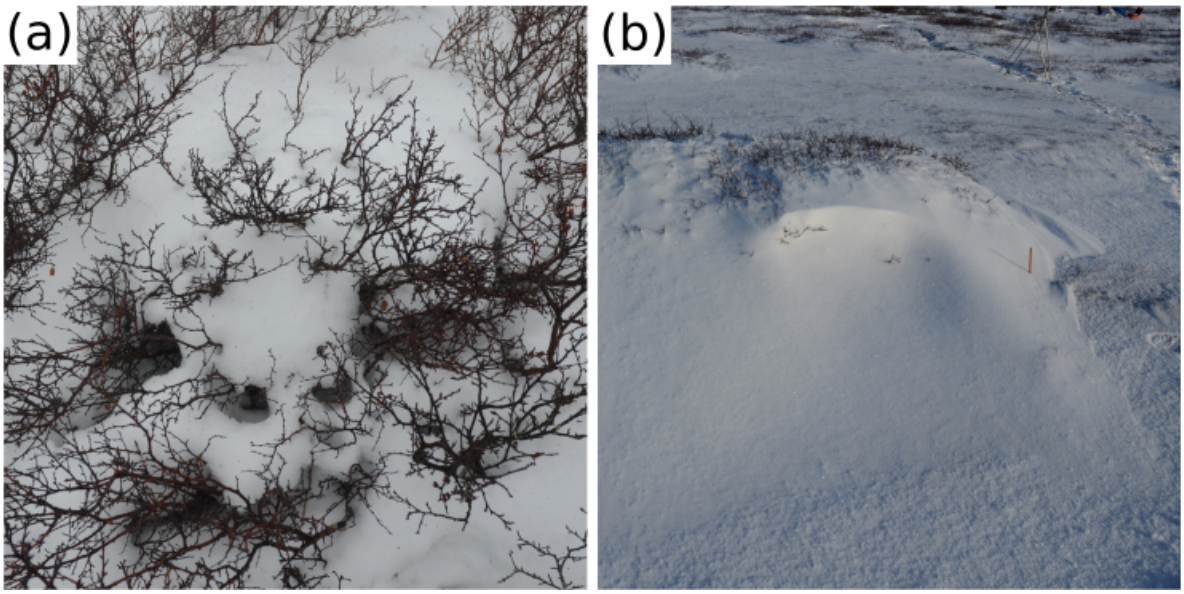

Figure 2.5. Photographs taken during the autumn campaign illustrating snow-wind-melting interactions. (a) increased melting in shrubs during the warm spell on 6 and 7 Nov. (b)

After warm spells or windy conditions, SSA profiles (0 to -10 cm from surface) varied between mixed and pure snow surfaces. Figure 2.6 shows SSA profiles for S0, S1, S2 and S3 measured on 8 November, 15 November and on 22 November, each day preceded by different meteorological conditions. Before 8 November, air temperatures were above freezing, it rained and winds were strong (6 and 7 November). In the night from 7 to 8 November there was a blizzard during which temperatures dropped to -5°C. On 8 November wind calmed down, temperatures varied between -2°C and -5°C and there was sunshine in the morning and light precipitation in the afternoon. SSA profiles were measured in the afternoon of 8 November (Figure 2.6a) and show very low values at S3 (5–15 m^2 kg^{-1}) but high values in the upper 4 cm at S2 (35–62 m^2 kg^{-1}). At S0 only SSA at 0 cm is high (42 m^2 kg^{-1}), the rest of the profile has values similar to S3. Instrument problems prevented SSA measurements at S1 on 8 November. The highest wind speeds of the season (16 m s^{-1}) were measured during a blizzard on 13 and 14 November during which

temperatures increased from -10°C to -5°C. SSA measured on 15 November at shrub sites S1, S2 and S3 had significantly higher surface values (60–78 m^2 kg^{-1}, Figure 2.6b) than SSA at S0 (10 m^2 kg^{-1}), where snow had been eroded down to an icy layer. Before 22 November, temperatures were below freezing and fresh snow precipitated without wind and the SSA profiles had similarly high values at all sites (64–89 m^2 kg^{-1}, Figure 2.6c).

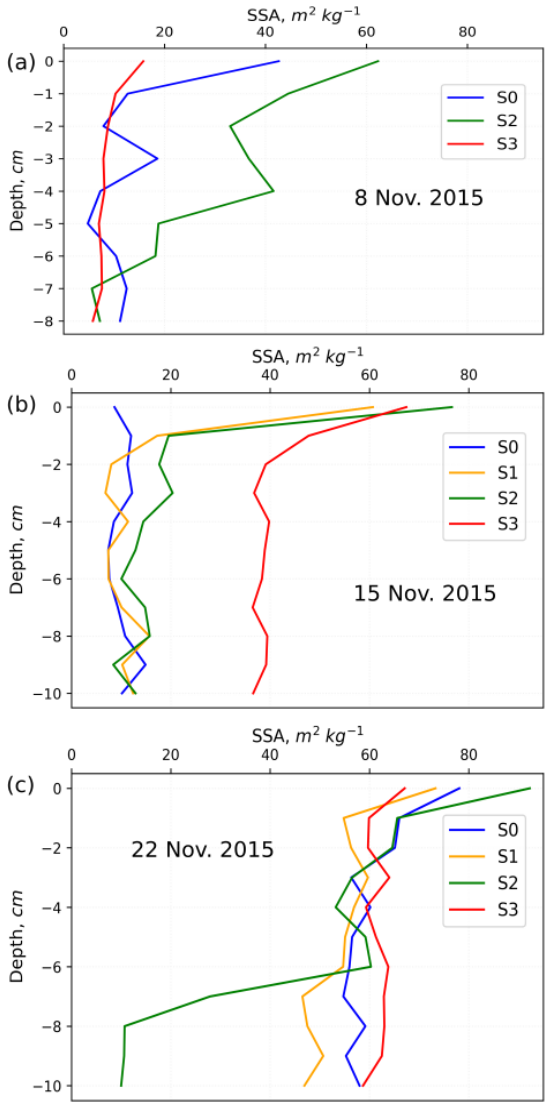

Figure 2.6. SSA profiles measured for the upper 10 cm of the snowpack near Umiujaq on 8 Nov. (a), 15 Nov. (b) and 22 Nov. (c) 2015 at the four different study sites S0 to S3. Different meteorological conditions, preceded the three days: before 8 Nov. temperatures were close to 0 °C and we observed melting. Before 15 Nov. wind speeds were extremely high (16 m s^{-1}) and before 22 Nov. snow precipitated under cold and calm conditions. Instrument problems prevented SSA acquisition at S1 on 8 Nov.

2.4.3.3 Retrieval of scaling factor *A*

Scaling factors were retrieved for 13 S0 albedo measurements (α_{sn_obs}) using theoretical snow albedo (α_{sn_TARTES}) calculated with TARTES and the vertical SSA profiles obtained at S0 for every measuring day. Figure 2.7a highlights how measured albedo (α_{sn_obs}, black) had lower values than the theoretical spectra (α_{sn_TARTES}, red) due to the influence of artifacts. Introducing *A* allowed the correction of α_{sn_obs} so that it matched the theoretical spectrum α_{sn_TARTES} ($\alpha_{sn\_obs,\ corr}$, blue). The fits achieved between the 13 corrected and theoretical spectra ($\alpha_{sn\_obs,\ corr}$ and α_{sn_TARTES}) were good and had a mean RMSE of 0.013. The retrieved *A* values are plotted in Figure 2.7b which were similar for all days and ranged between 0.96 and 0.97, except for the 8 November when values were around 0.94. To correct albedo measured over mixed surfaces (α_{mix_obs}), we used the mean *A* value averaged for every measuring day.

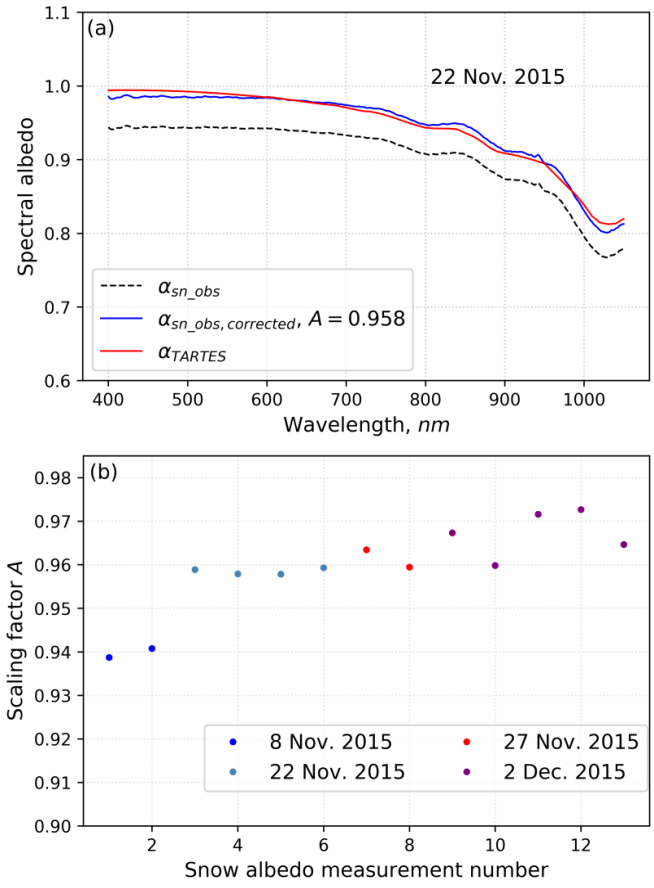

Figure 2.7. Determination of the scaling factors used to correct artifacts in measured albedo. (a) Spectral snow albedo observed at the lichen site S0 on 22 Nov. α_{sn_obs} (black) is the measured snow albedo. α_{sn_TARTES} (red) is the theoretical snow albedo computed with TARTES from the SSA profiles. $\alpha_{sn\_obs,\ corrected}$ (blue) is the measured spectrum after correction with A=0.958. (b) Deduced scaling factors for all 13 snow albedo measurements taken at S0 during the autumn campaign 2015 in Umiujaq.

2.4.3.4 LME simulations

The performance of the LME was tested with 31 $\alpha_{mix\_obs,\ corr}$ spectra and, in most cases, returned a good fit between observed and simulated albedo. In most cases the RMSE varied significantly with the choice of α_{veg} and best fits were usually obtained with the branch reflectivity measurements of Juszak et al. (2014). Figure 2.8 shows four examples to present the fits achieved between observed (black) and simulated (red) spectra with the best-fitting α_{veg}, and also to present the variations introduced by the choice of α_{veg} (blue, green and yellow). Naturally, those variations were more pronounced in tall shrubs (S3) and early in the snow season (8 November) because of the proportionally larger contribution of α_{veg} to the total surface albedo. All simulations in Figure 2.8 were run with snow albedo spectra obtained with TARTES (α_{sn_TARTES}).

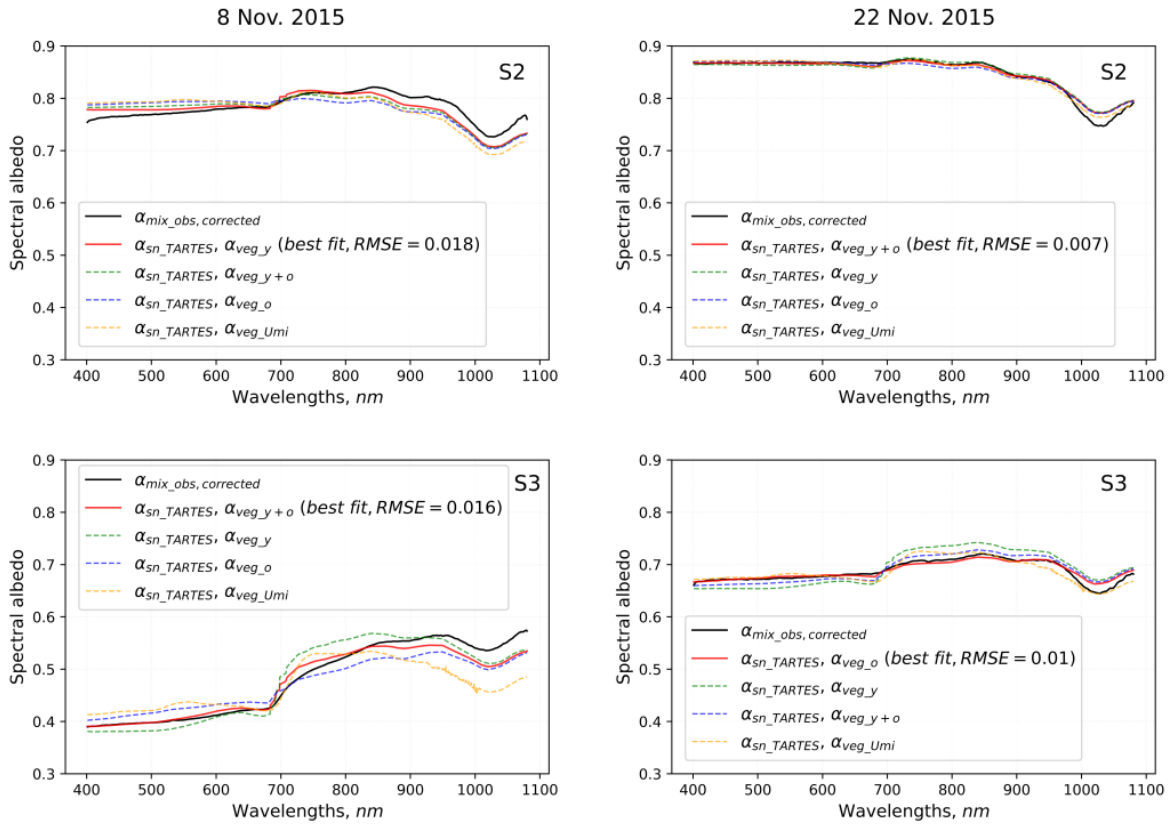

Figure 2.8. Illustrating the fit between observed albedo at shrub sites S2 and S3 ($\alpha_{mix\_obs,\ corrected}$, black) and simulations with the LME (Eq. (2.1)). Simulations in red used the best-fitting α_{veg} spectra, all other colors (green, blue and yellow) are simulations with alternative α_{veg} spectra. α_{veg_o} and α_{veg_y} are old and young branch reflectivity (Juszack et al. 2014), α_{veg_y+o} is the average spectra of old and young branches and α_{veg_Umi} is the average of five albedo spectra measured near Umiujaq. All simulations used snow albedo computed with TARTES (α_{sn_TARTES}).

Variations induced by the two approaches for snow albedo estimation, i.e. calculation with TARTES (α_{sn_TARTES}) vs. measurements at S0 (α_{sn_obs}), were surprisingly small for most days and the average RMSE was only slightly better for simulations using α_{sn_TARTES} (0.009) than for those using α_{sn_obs} (0.012). The RMSE was only averaged for simulations made with the best-fitting α_{veg}. To analyze the impact of the two approaches at different wavelengths, we calculated the residuals per wavelength between the 31 observed spectra and the corresponding simulations run with α_{sn_TARTES} and α_{sn_obs}, respectively, and show their average in Figure 2.9. For both cases, mean residuals were similar at most wavelengths, but the standard deviation, indicated by the red and blue shaded areas in the graph (Figure 2.9), were larger for simulations using $\alpha_{sn\_obs,}$ especially in the range 950 – 1080 nm. Those large variations were caused by simulations for days when SSA values for mixed and pure snow surfaces were different, such as on 8 November, because this is when the simplified approach (using α_{sn_obs}) cannot return accurate snow albedo spectra reducing LME performance (i.e. larger residuals).

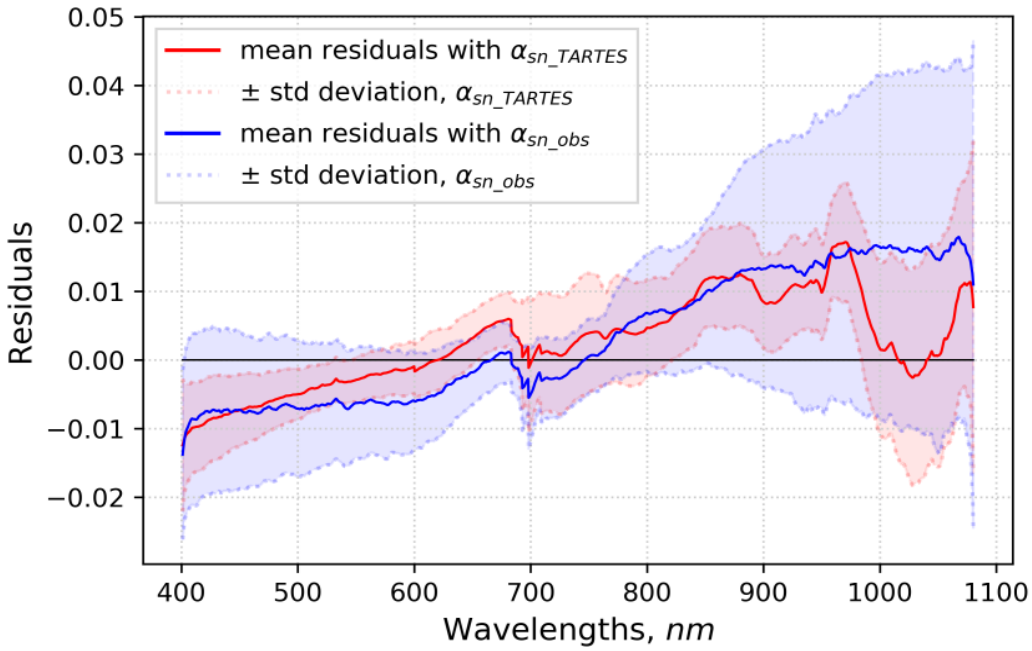

Figure 2.9. Average residuals (solid line) and their standard deviation (dashed line and shaded area) per wavelength for LME simulations conducted with a snow albedo parameter computed with TARTES (α_{sn_TARTES}, red) and a snow albedo parameter derived from snow albedo measurements at S0 (α_{sn_obs}, blue).

2.4.4 Discussions

2.4.4.1 Impact of shrubs on spectral mixed surface albedo

In the visible spectrum (400–750 nm) where branches are highly absorbent (albedo 0.05–0.1, Figure 2.3), and snow highly reflective, shrubs strongly reduced albedo by up to 55 % compared to pure snow surfaces where albedo was almost 1 (S3 vs. S0 in Figure 2.4a). In the near-infrared (750–1080 nm) branches are less absorbent (albedo around 0.4, Figure 2.3) and pure snow less reflective (albedo generally 0.55–0.85), shrub-induced albedo reductions were therefore only up to 18 % (S3 vs. S0 in Figure 2.4a). A peculiarity on 8 November is the higher near-infrared albedo at S2 than at S0. The increase is probably produced by the higher snow SSA due to the recent snowfall, and hence reflectance, at S2 (Figure 2.6a) which counterbalanced the absorption of protruding branches.

Overall however, shrub-induced albedo reductions were significant and, at S3, delayed most of the surface brightening associated with the formation of a pure snow layer by a full month which has an important impact on the tundra surface shortwave radiation budget. To quantify the amount of absorbed radiation at S0, S2 and S3 on 8 November and 2 December we multiplied incoming radiation with measured spectral albedo. Incoming radiation was not taken from Solalb measurements because we did not conduct an absolute calibration of the spectrometer signal. Instead, it was determined with SBDART, a model that computes plane-parallel radiative transfer in the Earth's atmosphere (Ricchiazzi et al. 1998). Here, the model atmosphere was set to the implemented version for sub-arctic winter and a cloud layer was introduced stretching from 1 to 2 km height with an optical thickness of 4 at 550 nm to simulate overcast measuring conditions. Incoming radiation for 8 November and 2 December at local noon are shown in Figure 2.10a and spectra of absorbed energy for S0, S2 and S3 are shown in Figure 2.10b (8 November) and c (2 December). On 8 November and compared to S0, additionally absorbed energy integrated over 400–1080 nm was 70 W m^{-2} at S3 and 13 W m^{-2} at S2, which are significant for the surface energy budget. On 2 December this amount was reduced to 6 W m^{-2} and 2 W m^{-2} at S3 and S2, respectively, due to the lower amount of protruding branches because of increased snow depth and because of the smaller amount of incoming radiation. Since the

spectrometer used in this study registers radiation only up to 1080 nm, the values calculated here are a lower limit of additional absorption and calculations considering the entire solar spectrum should return even higher values.

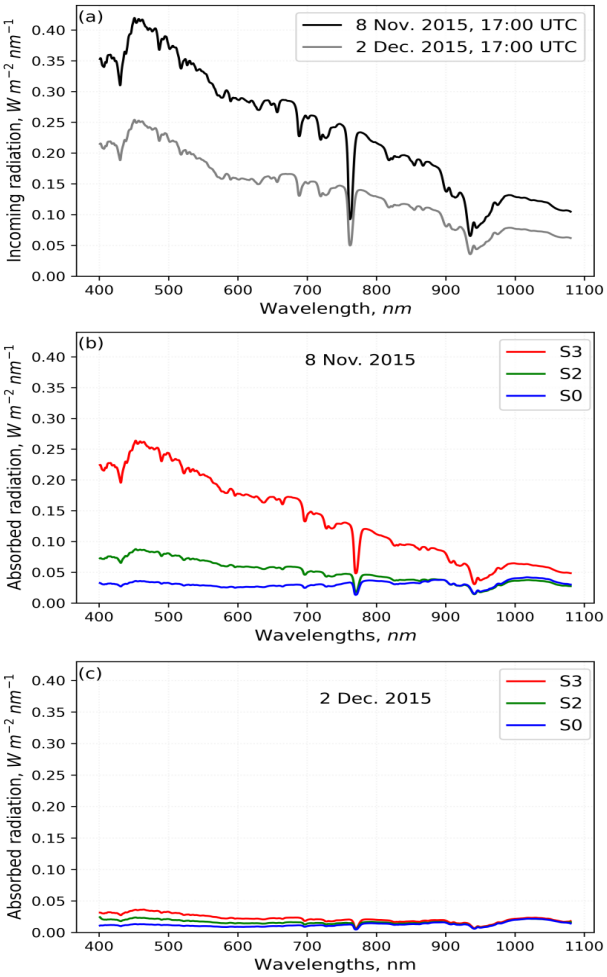

Figure 2.10. Spectral incoming radiation for 8 Nov. and 2 Dec. at 17:00 UTC as calculated with SBDART for overcast conditions (top) and spectra of absorbed radiation (middle and bottom) for the lichen site S0 (blue), medium shrub site S2 (green) and tall shrub site S3 (red).

In addition to the overall impact on the surface energy budget, potentially important effects arise from the fact that most additional absorption is localized in branches which consequently heat up. As a first consequence, branch heat-up increases surface

temperatures which could modify the land surface-atmosphere energy exchange compared to pure snow, affect air temperature and establish a biogeophysical feedback to climate (Sturm et al. 2005, Pomeroy et al. 2006, Loranty and Goetz 2012). Secondly, branch heat-up may affect the heat flux through the snow and therefore the thermal regime of permafrost by impacting melting events, snow metamorphism and depth hoar formation in autumn which determine the insulating properties of the snowpack that persist all winter (Domine et al. 2016, Barrere et al. 2018). In particular during warm spells, which are becoming more frequent in autumn (Hansen et al. 2014), heated branches locally amplify snow melting (Figure 2.5a) and increase the formation of melt-freeze layers in the snowpack (Barrere et al. 2018). Melt-freeze layers have high thermal conductivity (Domine et al. 2016, Barrere et al. 2018) and are therefore poor insulators contributing to permafrost cooling in winter (Barrere et al. 2018). When it is too cold for melting, a horizontal temperature gradient establishes between heated branches and colder snow which enhances depth hoar formation near branches. Depth hoar usually has a low thermal conductivity and is a good insulator (Domine et al. 2012, 2016) limiting permafrost cooling during winter. However, the radiative effect is locally limited and the most important factor for enhanced depth hoar formation in shrubs is probably due to the lack of snow compaction described in Domine et al. (2016). In conclusion, the temperature evolution in the Arctic tundra and the concomitant frequency of melting events seems to be the controlling factor for the magnitude of the impact of shrub-induced albedo reductions and branch heat-up on climate and on the thermal regime of permafrost.

2.4.4.2 Shrub impact on snow-wind-melt interactions and SSA

Shrub-induced increases in melting during warm spells and preferential accumulation of wind-driven snow in cold weather have been observed here and in numerous studies (e.g. Sturm et al. 2001, Marsh et al. 2010, Domine et al. 2016). This suggests that snow SSA at the surface, which is influenced by melting and wind-driven redistribution (Domine et al. 2012), is modified by protruding branches. On 8 November SSA distribution at S0, S2 and S3 was complex, probably due to the combined effect of high temperatures and rain on 6 and 7 November, a blizzard in the night 7/8 November and sunshine on 8 November. SSA

at S3 was low (5–15 m^2 kg^{-1}), likely because rain and high temperatures on 6 and 7 November produced a melt-freeze layer. It is however difficult to understand why SSA did not increase after the blizzard, which had been the case at S2 where SSA is higher (62 m^2 kg^{-1} at the surface) and, to a lesser extent, at S0 (42 m^2 kg^{-1} at the surface). A possible explanation is the sunshine in the morning of 8 November that may have caused radiative heating of branches which at S3, where the branch network is densest, melted the snow layer that precipitated during the blizzard. On 15 November, after strong winds, SSA was lower at S0 (~ 10 m^2 kg^{-1}) than at S1, S2 and S3 (61–78 m^2 kg^{-1} at the surface, Figure 2.6b) which is the expected distribution because protruding branches increase aerodynamic roughness, reduce wind speed (Essery and Pomeroy 2004, Beringer et al. 2005) and cause fresh snow with high SSA to accumulate whereas at pure snow surfaces fresh snow is scrapped off exposing the underlying melt-freeze crust with low SSA. Before 22 November, temperatures were below freezing and fresh snow precipitated without wind. These conditions caused no particular shrub-induced snow-wind-melting interactions and the corresponding SSA profiles had similarly high values at all sites (64–89 m^2 kg^{-1}, Figure 2.6c).

The presented data highlights important and complex shrub-SSA interactions, but more detailed measurements are needed to fully understand and quantify the SSA-shrub-albedo effect. Studying shrub-SSA interactions is important because SSA controls the near-infrared albedo of snow (e.g. Dumont et al. 2017) and thus impacts the radiation budget of snow and snowpack temperatures in autumn.

2.4.4.3 Suitability of LME to model mixed surface albedo

Overall, observed and calculated mixed surface albedo matched well with a mean RMSE of 0.009 (Figure 2.8). The essential preparative step to obtain a good match was to correct artifacts in measured albedo through a scaling factor *A*. This factor *A* was consistently between 0.96 and 0.97, except for one day (Figure 2.7b), suggesting a systematic error probably caused by the shadow cast by the operator and measuring device. We performed calculations of the shadow in the footprint of the sensor (set at 1 m above the snow surface)

due to the operator modeled as a fully absorptive vertical rectangle (200 cm high and 60 cm wide) at a given distance from the sensor. Results show shadowing factors ranging from 0.962 to 0.976 for distances of 1.5 – 2 m which agree well with our *A* factors. Note that the presented LME validation is restricted to diffuse conditions as direct light complicates the problem because χ becomes a function of the solar zenith angle.

Best fits were found using branch albedo α_{veg} measured by Juszak et al. (2014) (Figure 2.3) which appears strange because it was measured in Siberia on *Betula nana* shrubs while our study was conducted in the Eastern Canadian Arctic with *Betula glandulosa* shrubs. Juszak et al. (2014) used a contact probe which possibly acquired more representative branch albedo than our hemispherically integrated measurements which record a bulk signal of branches, some remaining leaves and the understory. This underlines the importance of obtaining pure branch albedo spectra.

Overall, using α_{sn_obs} or α_{sn_TARTES} had little influence on the fit quality despite the possible difference of SSA in snow in presence of branches. Measuring snow albedo over adjacent pure snow surfaces, like here S0, therefore in most cases seems an acceptable approximation to determine α_{sn}. Exceptions are periods with extreme weather conditions, like warm spells or extreme winds, when surface SSA at mixed surfaces varied significantly from SSA at pure snow surfaces. Those conditions are expected to become more frequent in the Arctic with climate warming (Hansen et al. 2014). The performance of simulations with α_{sn_TARTES} may have been biased by our assumption that SSA profiles measured at one point were representative for the whole site area because snow SSA varies in space, especially under windy conditions (Domine et al. 2002) and probably when heated branches cause local melting.

Additional assumptions for the calculation of α_{sn_TARTES} were that impurities were negligible, that SSA and density were correlated and that conditions were 100 % overcast. The impurity assumption may seem unlikely as waste burning around Umiujaq provides a source for soot and strong winds could transport mineral-dust to the snow. However, if

there was an impact of those impurities it was probably included in the coefficient *A* and the correct determination of quantity and type of impurities would require to sample and analyze the snow or to use vertical absorption profiles (Tuzet et al. 2019) which was beyond the scope of this paper. That SSA and snow density were correlated was shown by an empirical data set of simultaneously measured density and SSA values (Figure 2.2) and has in general been observed elsewhere (Domine et al. 2007). Although the measured density values had relatively large standard deviations, which introduces an uncertainty to the calculated snow density, the impact on snow albedo simulations is probably small in most cases. Snow density impacts snow albedo only indirectly by changing the penetration depth of light (Libois et al. 2013) which limits the impact to specific cases when the surface snow layer has high SSA values and is underlain by a layer with low SSA values. Finally, the assumption of 100 % overcast conditions can be considered legitimate because it was based on synoptic observations in the field. Moreover already small amounts of direct light increased measured snow albedo above 1 which was therefore easily detectable and, in those cases, measurements were not considered. In summary, the assumption that SSA is spatially homogeneous has probably the strongest impact on the albedo simulations here. The impact of impurities, which is probably small, is absorbed by fitting *A* and the uncertainty in snow density most likely has a comparatively small impact. We suggest therefore that future studies take several measurements of surface SSA for α_{sn_TARTES} calculations to cover spatial variability and to potentially increase the performance of the LME.

2.4.5 Conclusion

Shrub-induced decreases of mixed surface albedo are wavelength-dependent and, early in the snow season (here 8 November), as high as 55 % at 500 nm and 18 % at 1000 nm. In autumn, these albedo decreases lead to the additional absorption of 70 W m^{-2} (integrated over 400–1080 nm). The energy is mostly absorbed by protruding branches resulting in radiative branch heating which potentially feeds back on climate by modifying the land surface-atmosphere energy exchange and by increasing air temperatures. By enhancing snow melting during warm spells, branch heating also impacts the insulation properties of

snow in autumn which is an important factor for the thermal regime of permafrost. Snow melting as well as the preferential accumulation of wind-driven snow in shrubs modified surface SSA, which is a controlling factor for near-infrared snow albedo and has therefore an impact on the snow radiation budget and snow temperatures in autumn. The evolution of air temperature and the frequency of melting events with climate warming will be the deciding factor on the magnitude of the shrub-albedo effect on climate and the thermal regime of permafrost.

Shrub-induced decreases of mixed surface albedo under diffuse light conditions can be accurately simulated with a linear mixing equation. It is important to use branch albedo instead of hemispherical albedo measured over shrubs in autumn. Simulations using snow albedo measured over adjacent shrub-free sites were satisfyingly accurate (mean RMSE: 0.012) but failed during extreme weather conditions and we suggest instead to calculate snow albedo with TARTES as a function of several snow SSA measurements in shrubs.

Acknowledgements. This work was funded by the BNP Paribas foundation (APT project), NSERC through the discovery grant program to FD and the French Polar Institute (IPEV) through program 1042 to FD. We thank the community of Umiujaq for their hospitality and support in the field. We are also grateful to the Centre d'Études Nordiques (CEN) for providing and maintaining the Umiujaq Research Station. Inge Juszak kindly supplied detailed spectral data of branch albedo, shown in Figure 2.3.

References

Barrere, M., F. Domine, M. Belke-Brea, and D. Sarrazin. 2018. Snowmelt Events in Autumn Can Reduce or Cancel the Soil Warming Effect of Snow–Vegetation Interactions in the Arctic. *Journal of Climate.* 31: 9507–9518.

Beringer, J., F. S. Chapin, C. C. Thompson, and A. D. McGuire. 2005. Surface energy exchanges along a tundra-forest transition and feedbacks to climate. *Agricultural and Forest Meteorology.* 131: 143–161.

Bonfils, C. J. W., T. J. Phillips, D. M. Lawrence, P. Cameron-Smith, W. J. Riley, and Z. M. Subin. 2012. On the influence of shrub height and expansion on northern high latitude

climate. *Environmental Research Letters.* 7: 015503.

Cabanes, A., L. Legagneux, and F. Domine. 2003. Rate of Evolution of the Specific Surface Area of Surface Snow Layers. *Environmental Science & Technology.* 3: 661–666.

Domine, F., M. Barrere, and S. Morin. 2016. The growth of shrubs on high Arctic tundra at Bylot Island: impact on snow physical properties and permafrost thermal regime. *Biogeosciences Discussions.* 13: 6471.

Domine, F., J. C. Gallet, J. Bock, and S. Morin. 2012. Structure, specific surface area and thermal conductivity of the snowpack around Barrow, Alaska. *Journal of Geophysical Research Atmospheres.* 117: 1–12.

Domine, F., A. S. Taillandier, A. Cabanes, T. A. Douglas, and M. Sturm. 2009. Three examples where the specific surface area of snow increased over time. *Cryosphere.* 3: 31–39.

Domine, F., A. S. Taillandier, S. Houdier, F. Parrenin, W. R. Simpson, and T. A. Douglas. 2007. Interactions between snow metamorphism and climate: physical and chemical aspects. Proceedings of the International Conference on the Physics and Chemistry of Ice, 11th, Bremerhaven, Germany, July 23-28, 2006 27–46.

Dumont, M., L. Arnaud, G. Picard, Q. Libois, Y. Lejeune, P. Nabat, D. Voisin, and S. Morin. 2017. In-situ continuous visible and near-infrared spectroscopy of an alpine snowpack. *Cryosphere.* 11: 1091–1110.

Essery, R., and J. Pomeroy. 2004. Vegetation and Topographic Control of Wind-Blown Snow Distributions in Distributed and Aggregated Simulations for an Arctic Tundra Basin. *Journal of Hydrometeorology.* 5: 735–744.

Gallet, J.-C. C., F. Domine, C. S. Zender, and G. Picard. 2009. Measurement of the specific surface area of snow using infrared reflectance in an integrating sphere at 1310 and 1550 nm. *Cryosphere.* 3: 167–182.

Grégoire, M., and Y. Bégin. 1993. The Recent Development of a Mixed Shrub and Conifer Community on a Rapidly Emerging Coast (Eastern Hudson Bay, Subarctic Quèbec , Canada). *Journal of Coastal Research.* 9: 924–933.

Hansen, B. B., K. Isaksen, R. E. Benestad, J. Kohler, Å. Ø. Pedersen, L. E. Loe, S. J. Coulson, J. O. Larsen, and Ø. Varpe. 2014. Warmer and wetter winters : characteristics and implications of an extreme weather event in the High Arctic. *Environmental Research Letters.* 9:114021.

Juszak, I., A. M. Erb, C. Maximov, and G. Schaepman-Strub. 2014. Arctic shrub effects on NDVI, summer albedo and soil shading. *Remote Sensing of Environment.* 153: 79–89.

Libois, Q., G. Picard, J. L. France, L. Arnaud, M. Dumont, C. M. Carmagnola, and M. D. King. 2013. Influence of grain shape on light penetration in snow. *Cryosphere.* 7: 1803–

1818.

Liston, G.E., J. P. Mcfadden, M. Sturm, and R. A. Pielke. 2002. Modelled changes in arctic tundra snow, energy and moisture fluxes due to increased shrubs. *Global Change Biology.* 8: 17–32.

Loranty, M. M., and S. J. Goetz. 2012. Shrub expansion and climate feedbacks in Arctic tundra. *Environmental Research Letters.* 7: 011005.

Loranty, M. M., S. J. Goetz, and P. S. A. Beck. 2011. Tundra vegetation effects on pan-Arctic albedo. *Environmental Research Letters.* 6: 029601.

Marsh, P., P. Bartlett, M. MacKay, S. Pohl, and T. Lantz. 2010. Snowmelt energetics at a shrub tundra site in the western Canadian Arctic. *Hydrological Processes.* 24: 3603–3620.

Ménard, C. B., R. Essery, and J. Pomeroy. 2014. Modelled sensitivity of the snow regime to topography, shrub fraction and shrub height. *Hydrology and Earth System Sciences.* 18: 2375-2392.

Myers-Smith, I. H., B. C. Forbes, M. Wilmking, M. Hallinger, T. Lantz, D. Blok, K. D. Tape, M. Macias-Fauria, U. Sass-Klaassen, E. Lévesque. 2011. Shrub expansion in tundra ecosystems: dynamics, impacts and research priorities. *Environmental Research Letters.* 6: 045509.

Painter, T. H., N. P. Molotch, M. Cassidy, M. Flanner, K. Steffen. 2007. Instruments and methods - Contact spectroscopy for determination of stratigraphy of snow optical grain size. *Journal of Glaciology.* 53: 121-127.

Payette, S. 1976. Les limites écologiques de la zone hémi-arctique entre la mer d'Hudson et la baie d'Ungava, Nouveau-Québec. *Cahiers de Géographie Du Québec.* 20: 347–364.

Pearson, R. G., S. J. Phillips, M. M. Loranty, P. S. Beck, T. Damoulas, S. J. Knight, and S. J. Goetz. 2013. Shifts in Arctic vegetation and associated feedbacks under climate change. *Nature Climate Change.* 3: 673–677.

Picard, G., Q. Libois, and L. Arnaud. 2016a. Refinement of the ice absorption spectrum in the visible using radiance profile measurements in Antarctic snow. *Cryosphere.* 10: 2655–2672.

Picard, G., Q. Libois, L. Arnaud, G. Verin, and M. Dumont. 2016b. Development and calibration of an automatic spectral albedometer to estimate near-surface snow SSA time series. *Cryosphere.* 10: 1297–1316.

Pomeroy, J. W., D. S. Bewley, R. L. H. Essery, N. R. Hedstrom, T. Link, R. J. Granger, J. E. Sicart, C. R. Ellis, and J. R. Janowicz. 2006. Shrub tundra snowmelt. *Hydrological Processes.* 20: 923–941.

Provencher-Nolet, L., M. Bernier, and E. Lévesque. 2014. Short term change detection in tundra vegetation near Umiujaq, subarctic Quebec, Canada. *Geoscience and Remote Sensing Symposium (IGARSS):* 4668–4670.

Ricchiazzi, P., S. Yang, C. Gautier, and D. Sowle. 1998. SB DART : A Research and Teaching Software Tool for Plane-Parallel Radiative Transfer in the Earth's Atmosphere. *American Meteorological Society.* 79: 2101–2114.

Ropars, P., and S. Boudreau. 2012. Shrub expansion at the forest–tundra ecotone: spatial heterogeneity linked to local topography. *Environmental Research Letters.* 7: 015501.

Sturm, M., T. Douglas, C. Racine, and G. Liston. 2005. Changing snow and shrub conditions affect albedo with global implications. *Journal of Geophysical Research.* 110: 1–13.

Sturm, M., J. P. Mcfadden, G. E. Liston, F. S. Chapin III, C. H. Racine, and J. Holmgren. 2001. Snow–Shrub Interactions in Arctic Tundra : A Hypothesis with Climatic Implications. *Journal of Climate.* 14: 336–344.

Taillandier, A. S., F. Domine, W. R. Simpson, M. Sturm, and T. A. Douglas. 2007. Rate of decrease of the specific surface area of dry snow: Isothermal and temperature gradient conditions. *Journal of Geophysical Research: Earth Surface.* 112: F3.

Tape, K., M. Sturm, and C. Racine. 2006. The evidence for shrub expansion in Northern Alaska and the Pan-Arctic. *Global Change Biology.* 12: 686–702.

Tuzet, F., M. Dumont, L. Arnaud, D. Voisin, M. Lamare, F. Larue, J. Revuelto and G. Picard. 2019. Influence of light absorbing particles on snow spectral irradiance profiles. *Cryosphere*. 13: 8.

Vionnet, V., E. Brun, S. Morin, A. Boone, S. Faroux, P. Le Moigne, E. Martin, and J. M. Willemet. 2012. The detailed snowpack scheme Crocus and its implementation in SURFEX v7.2. *Geoscientific Model Development.* 5: 773–791.

Vionnet, V., G. Guyomarc'h, F. Naaim Bouvet, E. Martin, Y. Durand, H. Bellot, C. Bel, and P. Puglièse. 2013. Occurrence of blowing snow events at an alpine site over a 10-year period: Observations and modelling. *Advances in Water Resources.* 55: 53–63.

Warren, S.G. 1982. Optical properties of snow. *Reviews of Geophysics and Space Physics.* 20: 67–89.

Lee, W.-L., K. Liou, A. Hall. 2011. Parametrization of solar fluxes over mountain surfaces for application to climate models. *Journal of Geophysical Research.* 116: 1–13.

Wiscombe, W.J. and S. G. Warren. 1980. A Model for the Spectral Albedo of Snow. I: Pure Snow. *Journal of the Atmospheric Sciences.* 37: 2712-2733.

Chapter 3

Article 2:
New allometric equations for arctic shrubs and their application to calculate the albedo of surfaces with snow and protruding branches

3.1 Preamble

In the first part of the results the weighting factor in the Linear Mixing Equation (LME) has been treated as an adjustable parameter. Here, in the second part of the results, an allometric approach was developed which allows calculating the weighting factor from shrub and snow height. The new approach was validated against the spectral albedo measurements that we took at shrub sites and which were presented already in Chapter 2.

The results have also been accepted as scientific article on 10 August 2020 to the *Journal of Hydrometeorology*: «Belke-Brea, M., Domine, F., Boudreau, S., Picard, G., Barrere, M., Arnaud, L., and Paradis, M. (2020). New allometric equations for arctic shrubs and their application to calculate the albedo of surfaces with snow and protruding branches.»

3.2 Résumé

Les arbustes arctiques réduisent l'albédo de la surface en hiver lorsque leurs branches percent le manteau neigeux. Pour calculer l'albédo de ces surfaces mélangées neige-arbustes, on doit connaître l'indice de surface des branches (ISB) des arbustes arctiques. De plus, il est nécessaire de connaître la fonction qui détermine la proportion de l'ISB d'un

arbuste qui dépasse le manteau neigeux et est exposé à la lumière (fonction de végétation exposée). Cette étude utilise une analyse structurelle de 30 bouleaux glanduleux (*Betula glandulosa*) échantillonnés près d'Umiujaq, Nord du Québec pour i) déterminer la relation allométrique entre la hauteur des arbustes et l'ISB, et ii) déterminer la fonction de végétation exposée propre aux arbustes Arctiques. L'albédo spectral (400–1080nm) de surfaces mixtes a ensuite été simulé à l'aide des équations mentionnées et validé à l'aide de mesures *in situ*. Les arbustes ont été échantillonnés dans deux sites, le premier situé sur la côte et l'autre dans une vallée voisine. La relation entre hauteur des arbustes et ISB était différente pour les deux sites. Les arbustes qui poussent dans la vallée sont protégés du vent et leur valeur d'ISB était de 30 % à 50 % plus faible. La fonction de végétation exposée déterminée ici diffère des fonctions linéaires couramment utilisées dans la littérature. Ces fonctions surestiment l'ISB des branches exposées. L'albédo était simulé avec une precision de 3 % lorsqu'on utilise les relations allométriques adaptées aux conditions environnementales de notre site d'étude. Cependant, les valeurs simulées étaient constamment surestimées par rapport aux mesures sur le terrain, probablement parce que les impuretés présentes dans la neige ne sont pas considérées dans le modèle. Nous concluons que les fonctions de végétation exposée et les équations allométriques propres aux différentes espèces doivent être intégrées aux modèles pour simuler de manière satisfaisante l'albédo de surfaces mélangées neige-arbustes.

3.3 Abstract

Arctic shrubs reduce surface albedo in winter when branches protrude above the snow. To calculate the albedo of those mixed surfaces, the branch area index (BAI) of Arctic shrubs needs to be known. Moreover, an exposed-vegetation function is required to determine the BAI for protruding branches only. This study used a structural analysis of 30 *Betula glandulosa* shrubs, sampled near Umiujaq, Northern Quebec, to i) establish an allometric relationship between shrub height and BAI and ii) determine a specific exposed-vegetation function for Arctic shrubs. The spectral albedo (400–1080 nm) of mixed surfaces was then simulated with the equations derived from this study and validated with *in situ* measured spectra. Shrubs were sampled from two sites, one along the coast, the other in a nearby valley. The shrub height-BAI relationship varied between both sites. BAI values of shrubs

growing in the wind-sheltered valley were 30 % to 50 % lower. The exposed-vegetation function obtained here differed from the linear functions found in the literature. The linear functions strongly overestimated the BAI of exposed branches. Albedo was well simulated with an accuracy of 3 % when using an allometric relationship adapted to the environmental conditions of our study site. However, simulated albedo values were consistently higher than field measurements, probably because radiation absorbed by impurities and buried branches was neglected in the model. We conclude that specific exposed-vegetation and allometric equations need to be implemented in models to accurately simulate the albedo of mixed snow-shrub surfaces.

3.4 Main text

3.4.1 Introduction

Due to Arctic warming, shrub abundance and height are increasing in the tundra (Tape et al. 2006, Myers-Smith et al. 2011, Ropars and Boudreau 2012, Tremblay et al. 2012, Lemay et al. 2018) which greatly darkens snowy winter surfaces when shrub branches protrude above the snow (Sturm et al. 2005, Loranty et al. 2011, Ménard et al. 2014b). The resulting albedo reduction potentially feeds back into regional and global climate through increases in air temperature, and also has potential impacts on permafrost thawing (Sturm et al. 2001, Pomeroy et al. 2006, Loranty and Goetz 2012, Pearson et al. 2013). The magnitude and direction of those feedbacks is not yet clearly determined (Chapin et al. 2005, Barrere et al. 2018) but paleoclimatological studies found that changes in Arctic vegetation and associated variations in the surface radiation budget probably played a major role in past climate changes (de Noblet et al. 1996, Otto-Bliesner and Upchurch Jr 1997, Jahn et al. 2005). This suggests that ongoing vegetation changes may also have a significant impact on climate. It is therefore important that Land Surface Models (LSMs) and climate models implement accurate methods to calculate the albedo of mixed Arctic surfaces with snow and protruding shrub branches.

In most LSMs, mixed surface albedo (α_{mix}) is calculated with a linear mixing equation of the form:

$$\alpha_{mix} = (1 - \chi) \cdot \alpha_{snow} + \chi \cdot \alpha_{veg}, \quad (3.1)$$

where α_{snow} is the snow albedo, α_{veg} is the shrub branch albedo and χ is a factor weighting α_{veg} and α_{snow} proportionally to the surface they cover. Values for α_{veg} and α_{snow} can be taken from field measurements or calculated with snow models (Sturm et al. 2005, Ménard et al. 2014B, Belke-Brea et al. 2019). Determining χ is more challenging because its value changes constantly as snow accumulation buries shrubs especially in early winter, and snowmelt exposes shrubs in late spring. One possibility for determining χ is to analyze ground-based, airborne, or satellite images. However, mixed surface albedo can then be calculated only for specific times when images are available and it does not allow use of Eq. (3.1) in a predictive way. Moreover, image-derived χ-values depend on the viewing angle.

Another possibility is to calculate χ using the branch area index (BAI) of shrubs. In optical studies, where the interaction between branches and light is investigated, BAI is usually defined as the cross-sectional surface of branches per total considered surface area (Sjöman et al. 2015, Pokorný and Marek 2000). The problem with this approach is that literature on BAI is particularly poor, and that BAI values are rarely available because their acquisition is complex (and often destructive). In addition, indirect measurement techniques that can be used for leaf area index acquisitions are not as easily applicable (Kucharik et al. 1998). As an alternative, we suggest using allometric relationships which link BAI to parameters that are easier to measure. For example, in the Joint UK Land Environment Simulator (JULES), BAI for trees is calculated as a function of woody biomass (Best et al. 2011). However, to our knowledge, no such allometric relationship exists for Arctic shrubs, although this seems particularly important in light of the ongoing shrubification of the tundra.

In addition to the BAI values, χ-calculations require an exposed-vegetation function which determines the BAI of protruding branches only, a value that changes with the burial or exposure of shrubs. An exposed-vegetation function is implemented in most LSMs (Verseghy 2009, Wang and Zeng 2009, Liston and Hiemstra 2011, Ménard et al. 2014a, Boone et al. 2017). This function is typically linear, calculating the ratio of snow height to shrub height, giving a fraction for protruding branches between 0 and 1, where 0 means that shrubs are completely snow covered. An additional, non-linear function was suggested by

Liston and Hiemstra (2011) where shrubs are considered to be hemispheric instead of parabolic (as for the linear function). It has often been observed that shrubs bend under the weight of snow (Sturm et al. 2005b, Pomeroy et al. 2006, Marsh et al. 2010, Ménard et al. 2014b). Exposed-vegetation functions specifically applied to calculate albedo of shrub tundra have therefore been modified by a factor which simulates this effect (Sturm et al. 2005, Liston and Hiemstra 2011, Ménard et al. 2014b). However, to our knowledge, the form of the exposed-vegetation function that actually fits the shape of Arctic shrubs has never been tested due to a lack of empirical data. Studies which used the modeling approach with BAI and exposed-vegetation functions validated model suitability only by comparing measured and modeled albedo values (Sturm et al. 2005, Liston and Hiemstra 2011), creating uncertainty regarding the sources of error in the model (Ménard et al. 2014b).

This study has two objectives. The first is to develop an allometric relationship which links the BAI to shrub height and to evaluate which form of the exposed-vegetation function reproduces the shape of Arctic shrubs. For the determination of the BAI and to test the exposed-vegetation functions, we used stratified shrub samples of 30 dwarf birches (*Betula glandulosa*) harvested near Umiujaq in Northern Quebec. Of the 30 shrubs, 22 had been harvested by Paradis et al. (2016) during a summer campaign in 2013, and the remaining 8 shrubs were harvested in this study during two consecutive campaigns in autumn 2015 and winter 2015/2016 when snow was already covering the ground. The second objective is to test whether the functions established in this study can accurately calculate χ and mixed surface albedo. For this we simultaneously measured shrub height and snow height as well as mixed surface spectral albedo (400–1080 nm) during the same 2015 autumn campaign where we harvested shrubs. Shrub height and snow height data were used to calculate χ, and then input to Eq. (3.1) to simulate mixed surface albedo. Values of α_{snow} and α_{veg} were taken from Belke-Brea et al. (2019), and are described briefly in the methods section. The simulated spectra were then validated with the measured mixed surface albedo. To summarize, this study proposes a method to improve the calculation of α_{mix} in LSMs and climate models.

3.4.2 Methodology

3.4.2.1 Study site

The study area is located on the Hudson Bay coast of Nunavik near the community of Umiujaq (56°33′07″N, 76°32′57″E; see Figure 3.1), which lies at the forest-tundra ecotone (Laberge and Payette 1995). The area is rather windy and covered by lichen and shrubs. Spruces, mainly black spruce (*Picea mariana*), also grow in wind-sheltered depressions. Nunavik is one of the regions that experienced the strongest greening trend in North America over the last three decades (Ju and Masek, 2016), mainly due to the expansion of shrubs which replaced lichen patches of mostly *Cladonia spp.* (Ropars and Boudreau 2012, Provencher-Nolet et al. 2014, Gagnon et al. 2019). The main shrub species in the Umiujaq region are dwarf birch (*Betula glandulosa*) (Payette 1976) and willow (mostly *Salix glauca* and *S. planifolia*). An automatic weather station in the Tasiapik Valley (Figure 3.1) measures air temperature since 1997. The mean annual air temperature since the start of the recording until 2018 is -3°C (CEN 2018). Strong winds and snow storms in autumn and winter are frequent in this region (Barrere et al. 2018) and these mainly blow from Hudson Bay (from the west and northwest), with winds reaching up to 100 km h^{-1} (Paradis et al. 2016).

Harvesting sites of *Betula glandulosa* were spread along the coast and within the Tasiapik Valley (Figure 3.1) (Paradis et al. 2016). Spectral albedo and shrub and snow height measurements were conducted on a plateau in the upper part of the Tasiapik Valley (Figure 3.1) where *B. glandulosa* shrubs of varying height (from ~30 cm to ~120 cm) grow in isolated patches or are regrouped in bushes of larger extent. To calculate snow albedo α_{snow}, we used snow physical properties (density and specific surface area (SSA)) that were also measured at these same sites. These snow measurements have already been reported by Belke-Brea et al. (2019).

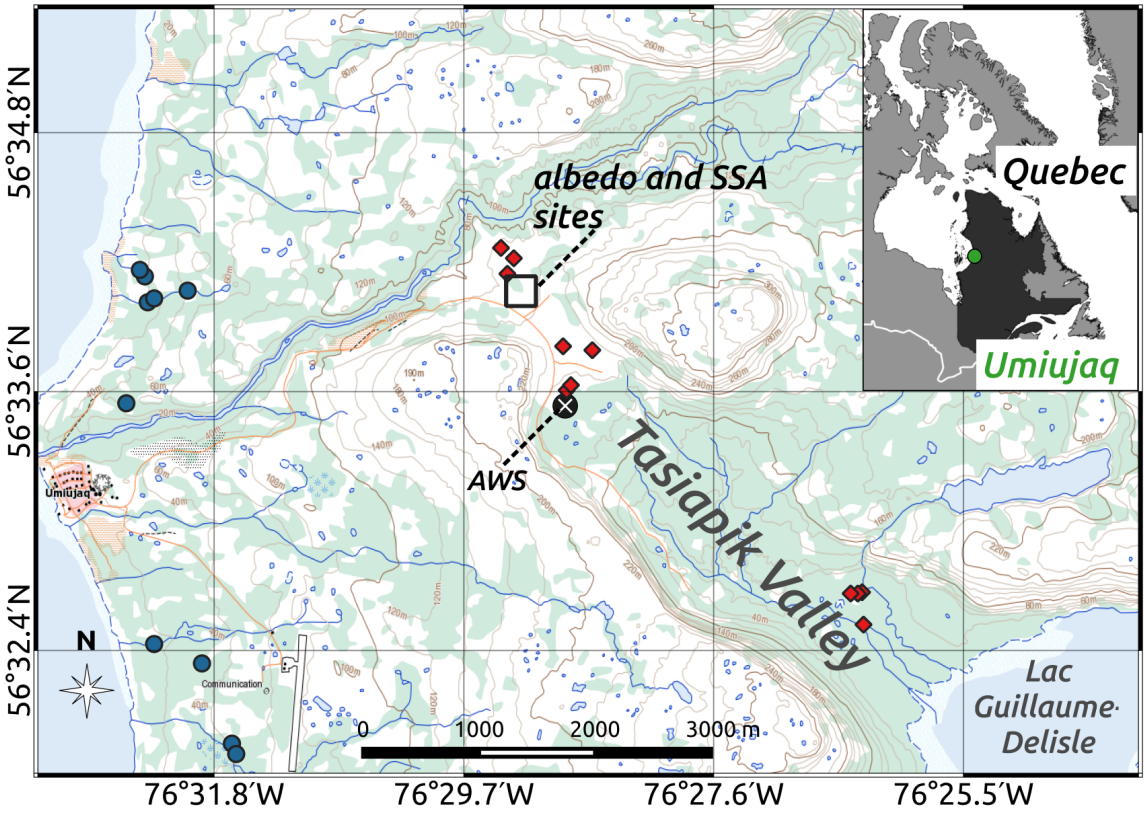

Figure 3.1. Map of the study area around Umiujaq with the albedo, height and SSA measurement sites marked with a black box and shrub harvesting locations along the coast marked with blue dots and those in the Tasiapik Valley with red diamonds. A white cross marks the position of the Automatic Weather Station (AWS).

3.4.2.2 Data acquisition

Shrub samples were mostly harvested by Paradis et al. (2016) during a campaign in August 2013. We extended the existing dataset consisting of 22 shrubs by sampling an additional 8 shrubs during two field campaigns in autumn 2015 (October to December) and winter (January) 2016, when shrubs were partly snow-covered. The snow height and shrub height data, required to calculate the weighting factor χ, as well as the spectral albedo of mixed surfaces were also obtained during the autumn campaign 2015. Autumn and winter are hereafter referred to as the snow cover period, and summer as the snow-free period.

Shrub sampling during the snow cover period

Shrub sampling during the snow cover period followed the protocol described in Paradis et

al. (2016): plastic squares 0.71 x 0.71 m^2 on each site (covering an area of 0.5 m^2) were deposited on the snow surface where shrubs were protruding (Figure 3.2). Metal poles positioned at the four corners of the plastic squares helped keep the shrubs in place even after snow removal. Branches longer than 1.5 cm were cut within each 10 cm vertical stratum (starting from the top of the shrub). The protocol for the snow cover period varied from the snow-free measurements of Paradis et al. (2016) only because snow had to be carefully removed in every stratum before cutting branches. The branch pieces harvested per 10 cm stratum were then taken to the laboratory to measure their length and diameter with electronic calipers (± 0.001 cm). Their cross-sectional surface was then calculated by assuming a cylindrical shape. We did not differentiate between stem, branches or twigs during the shrub sampling and, in this study, the term 'branch' refers collectively to all harvested woody elements.

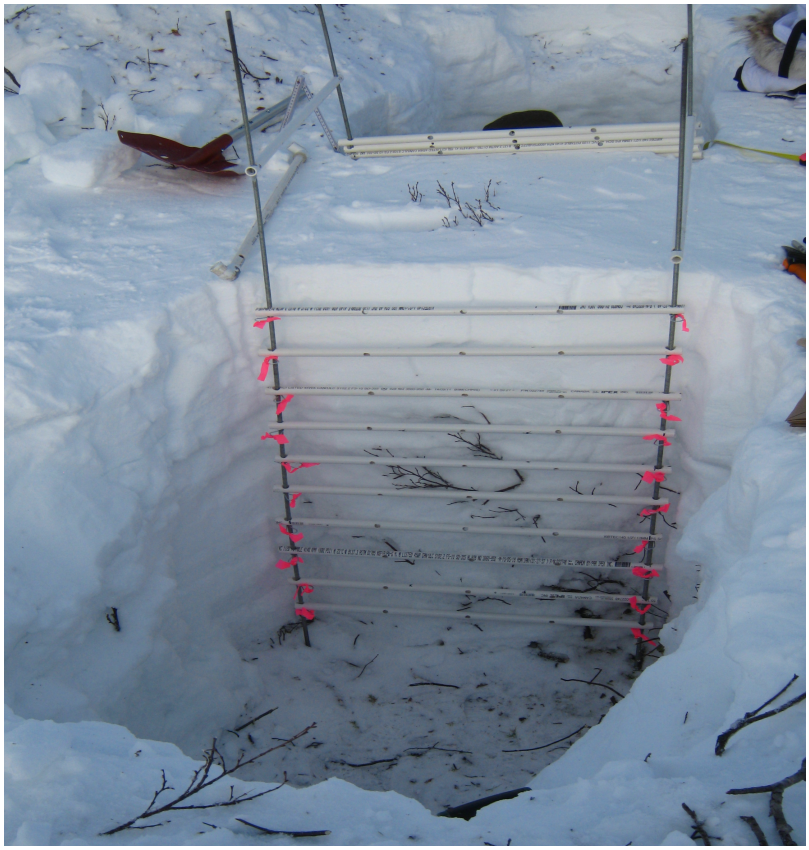

Figure 3.2. Photograph taken during shrub sampling in January 2016. Snow had to be carefully removed to cut branches within each of the 10 cm strata, which are marked by the horizontal plastic bars in the photograph.

Height and spectral albedo measurements

Snow height, shrub height and spectral albedo were measured simultaneously throughout the autumn campaign 2015. The spectral albedo data set consists of 31 spectra measured in the Tasiapik Valley over mixed surfaces. Albedo data in this study correspond to the mixed surface spectra used in Belke-Brea et al. (2019), where their acquisition was described in detail. Briefly, the spectral albedo of mixed surfaces was calculated as the ratio of spectral reflected over incident radiation. Radiation was measured with the Solalb instrument. Solalb consists of a cosine light collector attached to one end of a 2 m long, rotatable metallic arm. Radiation is measured by orienting the arm upwards to the sky or downwards to the ground, with a 0.5° accuracy using an electronic level. The acquisition of incoming and outgoing radiation takes together ca. 2 minutes. Solalb includes a MayaPro spectrometer from Ocean Optics ® with an effective resolution of 3 nm and a spectral range from 200 to 1120 nm (Picard et al. 2016, Belke-Brea et al. 2019). Only the range from 400 to 1080 nm was used as the signal-to-noise ratio was too low for the other wavelengths. The albedo spectra were smoothed using a first order butterworth filter produced with the scipy.signal.butter function in Python by setting the functions cutoff frequency to 0.05. To measure radiation, Solalb uses a home-built cosine light collector. The collector's response for radiation when solar zenith angle exceeds 70° introduces an uncorrectable error of ±15 % (Picard et al. 2016). The solar zenith angle of direct incoming light in the Arctic in autumn and winter generally exceeds 70°, consequently albedo could only be acquired during overcast days with 100 % diffuse light conditions.

Snow height and shrub height were measured with a snow probe. To avoid the disturbance of the site where we also measured albedo on several days, we only took 5 shrub height measurements. These were randomly sampled within the shrub patch. During each measurement, shrub height was determined by taking the height of the highest protruding branch in a 10 cm radius around the position of the snow probe. The average of the 5 measurements was used as input parameter for mixed surface albedo simulations.

3.4.2.3 Statistical analysis of shrub data

The statistical analysis of the shrub data aims to 1) establish an allometric relationship between shrub height H_{veg} and the total branch area index (BAI_{total}) and 2) verify which form of the exposed-vegetation function reproduces the measured data from the stratified sampling. The exposed-vegetation function is required to calculate the partial branch area index ($BAI_{exposed}$) of branches protruding above the snow. The parameters and variables used in the following equations are listed and explained in the List of Notations at the beginning of this document (pp xiv-xv).

H_{veg} – BAI_{total} allometric relationship

BAI_{total} for each sampled shrub specimen was obtained by summing the cross-sectional surface of all the specimen's branch pieces and by normalizing the summed value to 1 m^2 (i.e. multiplying it by two since the sampling quadrats were 0.5 m^2). H_{veg} has not been specifically measured for each sampled shrub specimen. It had to be deduced by taking half the height of the uppermost strata (Figure 3.2). This means that, for example, shrubs with a height of 53, 55 or 59 cm which have an uppermost stratum reaching from 50 cm to 60 cm were all considered to be 55 cm high. H_{veg} has a rough resolution of 10 cm which increases the variability of BAI_{total} values at a given height point.

The allometric equation developed to relate H_{veg} to BAI_{total} is a power function of the form:

$$BAI_{total} = a \cdot H_{\mathrm{veg}}^{b}, \tag{3.2}$$

where a and b are fitted coefficients. Allometric equations are commonly expressed as power functions. They are either fitted with a log-log regression (e.g. Bond-Lamberty et al. 2002, Jenkins et al. 2003) or a weighted nonlinear least-square regression (NLS) (Berner et al. 2015). For the log-log regression, the dependent and independent variables are logarithmically transformed so the power function can be fitted with a linear regression. The log-log transformation introduces a bias which has to be corrected with the Sprugel correction (Sprugel 1983). We performed the NLS regression with Python's scipy.optimize.least_squares function and the linear regression with the

scipy.stats.lineregress function. Using the NLS approach gave slightly better fits for the allometric regressions (i.e. lower root-mean-square errors (RMSE) and higher coefficients of determination (R^2)), so only those results are presented here.

Sampled shrubs grew in two environmentally different locations, i.e. close to the coast and within the Tasiapik Valley (Figure 3.1). We used a local model where allometric equations were established separately for valley and coastal shrubs to account for a potential location effect in the relationship between H_{veg} and BAI_{total}. In addition, we used a global model, where only one equation was established that considered all sampled shrubs. Similar to Berner et al. (2015), we used an F-test to compare the quality of fit between the two models (local vs. global). F statistics are an adaption of the analysis of variance (Motulsky and Christopoulos 2005) and consist in comparing the cumulative sum-of-squares of errors (SSE) of the local model (SSE_{loc}) with that of the global model (SSE_{glob}) by calculating an F-ratio (F) with:

$$F = \frac{\left(SSE_{glob} - SSE_{loc}\right) / \left(DF_{glob} - DF_{loc}\right)}{SSE_{loc} / DF_{loc}}. \quad (3.3)$$

DF_{loc} and DF_{glob} are the degrees of freedom for the local and global model (Motulsky and Christopoulos 2005). F values close to 1 indicate that there is no statistical difference in the fit between the local and the global model whereas larger values indicate significant differences.

The exposed-vegetation function

Eq. (3.2) allows calculating the BAI_{total} value of uncovered shrubs with known height. However, during the snow season shrubs are partly covered by snow. Eq. (3.4) is used to obtain the partial BAI of exposed branches ($BAI_{exposed}$):

$$BAI_{exposed} = f_{\exp} \cdot BAI_{total}, \quad (3.4)$$

where f_{exp} is the exposed-vegetation factor. To determine $BAI_{exposed}$ from easy-to-measure shrub height and snow height (H_{snow}), f_{exp} is related to the proportion of the shrub covered by snow (H_{snow}/H_{veg}). The exposed-vegetation function for Arctic shrubs proposed by Liston

and Hiemstra (2011) is of the form:

$$f_{\exp} = 1 - \left(\frac{H_{snow}}{C \cdot H_{veg}} \right)^{d}, \tag{3.5}$$

where d is a shape factor and C is a bending parameter. The bending parameter was introduced to simulate shrub bending in the snow cover period due to snow load (Ménard et al. 2014b). For shrub data acquired in the snow-free period, the bending parameter is irrelevant and thus set to 1 (which means no bending). However, for shrub data acquired in the snow cover period, bending may be an issue. In that case the bending parameter may have a different value than 1. To test for shrub bending we compared the stratified sampling results of shrubs harvested in the snow cover period vs. the snow-free period. Furthermore, we tested whether a shape factor equal to 1 for parabola-shaped shrubs or equal to 2 for hemisphere-shaped shrubs (Liston and Hiemstra 2011, Ménard et al. 2014a) better reproduces the empirical data obtained from the stratified shrub sampling (Figure 3.2).

Backscattering factor k

Most of the light that reaches snowy surfaces is scattered back, due to the high albedo of snow. The backscattered light illuminates protruding shrub branches from below, therefore increasing the branch surface that interacts with light. To account for this effect, we introduced a backscattering factor *k*. Values for the backscattering factor depend on the amount of incoming light reaching the snow surface, i.e. the amount of light that is not intercepted by shrub branches. Moreover, it depends on the albedo of snow (α_{sn}), which determines how much of the incoming radiation is absorbed in the snowpack. The backscattering factor is calculated from:

$$k = 1 + \alpha_{sn} \cdot \left(1 - BAI_{exposed}\right). \tag{3.6}$$

Using the shrub coverage quantified by $BAI_{exposed}$ in Eq. (3.4) allows to deduce the fraction of the snow surface that receives light (1-$BAI_{exposed}$). For α_{sn} we used, as a first approximation, a constant value of 0.9. By setting a constant value we neglected the wavelength-dependence and the natural variability of snow albedo with changing snow

physical properties. Using Eq. (3.6) is a simplified approach to determine the effect of backscattered light. More accurate *k*-values could be calculated with a 3-D radiative transfer model. However, this goes beyond the scope of this study.

Using *k* together with the exposed-vegetation factor f_{exp}, the weighting factor χ in Eq. (3.1) can finally be calculated with:

$$\chi = k \cdot f_{\exp} \cdot BAI_{total}. \tag{3.7}$$

3.4.2.4 Simulating mixed surface albedo

Mixed surface albedo was calculated with the linear mixing equation (LME) shown in Eq. (3.1). The input values for snow albedo (α_{snow}) and shrub albedo (α_{veg}) were taken from Belke-Brea et al. (2019) where their determination is described in detail. Briefly, α_{snow} was calculated with the snow radiative transfer model TARTES (Libois et al. 2013, available from https://pypi.org/project/tartes/). The model computes snow albedo as a function of snow specific surface area (SSA) and snow density. SSA is the surface area of the snow-air interface per mass unit and this variable is inversely related to the optical grain diameter of snow (Warren 1982, Domine et al. 2007). Belke-Brea et al. (2019) measured it with the DUFISSS instrument detailed in Gallet et al. (2009). Snow density was then calculated from an empirical relationship between SSA and density (Figure 2.2). α_{veg} was chosen from a selection of four shrub albedo spectra which contained three spectra measured by Juszak et al. (2014) and one spectrum measured by Belke-Brea et al. (2019). Belke-Brea et al. (2019) tested which of the available α_{veg} spectra returned the best fit between simulated and measured mixed surface albedo. Here, we use the shrub albedo spectra which Belke-Brea et al. (2019) found to return the best fit. This was, in most cases, the average reflectivity of old and young branches as measured by Juszak et al. (2014) (Figure 2.3).

The weighting factor χ was calculated from Eq. (3.2), (3.5), (3.6) and (3.7) using measured snow and shrub heights. This is a key difference with the simulations in Belke-Brea et al. (2019), where the weighting factor χ was treated as an unknown and adjusted using a linear least-squares method. Since both studies share the same data for mixed surface albedo, we consider the adjusted χ values (χ_{adj}) of Belke-Brea et al. (2019) to be reference values. χ_{adj}

values were therefore used to test the quality of the χ values (χ_{calc}) calculated here.

Finally, Belke-Brea et al. (2019) found that before simulated and measured mixed surface albedo could be compared, the latter had to be corrected for wavelength-independent artifacts, such as variations in the incoming radiation by passing clouds or shadows cast by the instrument and operator. Following Picard et al. (2016), they introduced a correction factor *A* and corrected all measured albedo spectra for those artifacts. Albedo after correction was 3–4 % higher than the initially measured values, indicating that the artifact correction is relatively small. In this study, only the corrected measured albedo spectra are used.

3.4.3 Results

3.4.3.1 H_{veg} – BAI_{total} allometric relationship

Figure 3.3 shows the H_{veg} - BAI_{total} correlation and the regression curves obtained for the local and global model. The data are distinguished for shrubs harvested along the coast (blue) and shrubs harvested in the Tasiapik Valley (red). Their distribution visibly demonstrates that the growing location had an influence on the H_{veg} - BAI_{total} correlation. Shrubs that grew along the coast had larger BAI_{total} values for the same H_{veg} than those that grew in the valley. This difference was more pronounced for larger shrubs (> 50 cm). The regression curves show a good fit with R^2 values between 0.60 and 0.79 and RMSE values between 0.10 and 0.15 (Figure 3.3). The regression curve for valley shrubs had the best fit (i.e. highest R^2 and lowest RMSE). The best-fit values for fitting coefficients *a* and *b* are listed in Table 3.1 together with their standard errors. The comparatively high standard errors for the coast shrub regression were caused by the low degrees of freedom (9) and the relatively large scatter of data points. The F-test (Eq. (3.3)) returned an F-ratio of 6.53 which has an associated *p*-value of 0.005. This means that the local model fits the sample data significantly better than the global model (Motulsky and Christopoulos, 2005). This confirms the location-dependence that was already visible in the distribution of the coastal and valley data points.

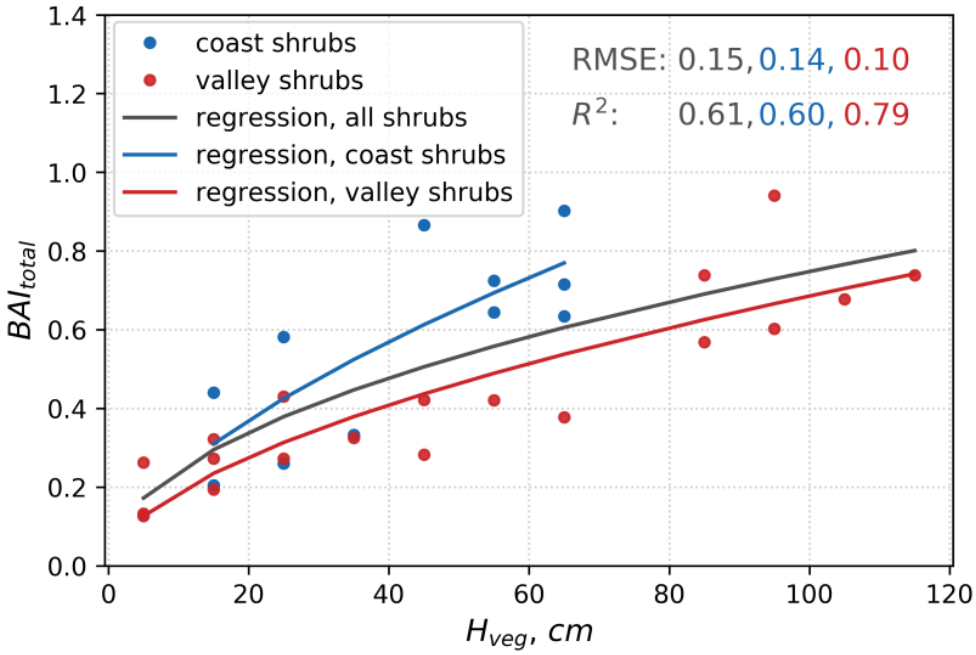

Figure 3.3. Nonlinear regression between shrub height H_{veg} and total projected branch area index BAI_{total} (Eq. 3.2) for all sampled shrubs (black), shrubs sampled at the coast (blue) and shrubs sampled in the Tasiapik Valley (red).

3.4.3.2 Exposed-vegetation function

Figure 3.4a displays the empirical correlation between f_{exp} and H_{snow}/H_{veg} which is similar for all shrubs independent of their height and has a low mean standard deviation of 0.03. There is no visible difference between shrubs harvested during the snow-free period (Figure 3.4a, blue) and those harvested during the snow cover period (Figure 3.4a, red). We expected the latter to have lower f_{exp} values due to shrub bending under snow weight. Bending of birch branches by the snow load has been observed before (Sturm et al. 2005, Pomeroy et al. 2006). However, the similarity between shrubs harvested during the snow cover and the snow-free periods (Figure 3.4a) suggests that no bending took place here – a result which is further discussed in section 4. The bending factor C in Eq. (3.5) is therefore set to 1 (meaning no shrub bending) for all subsequent calculations.

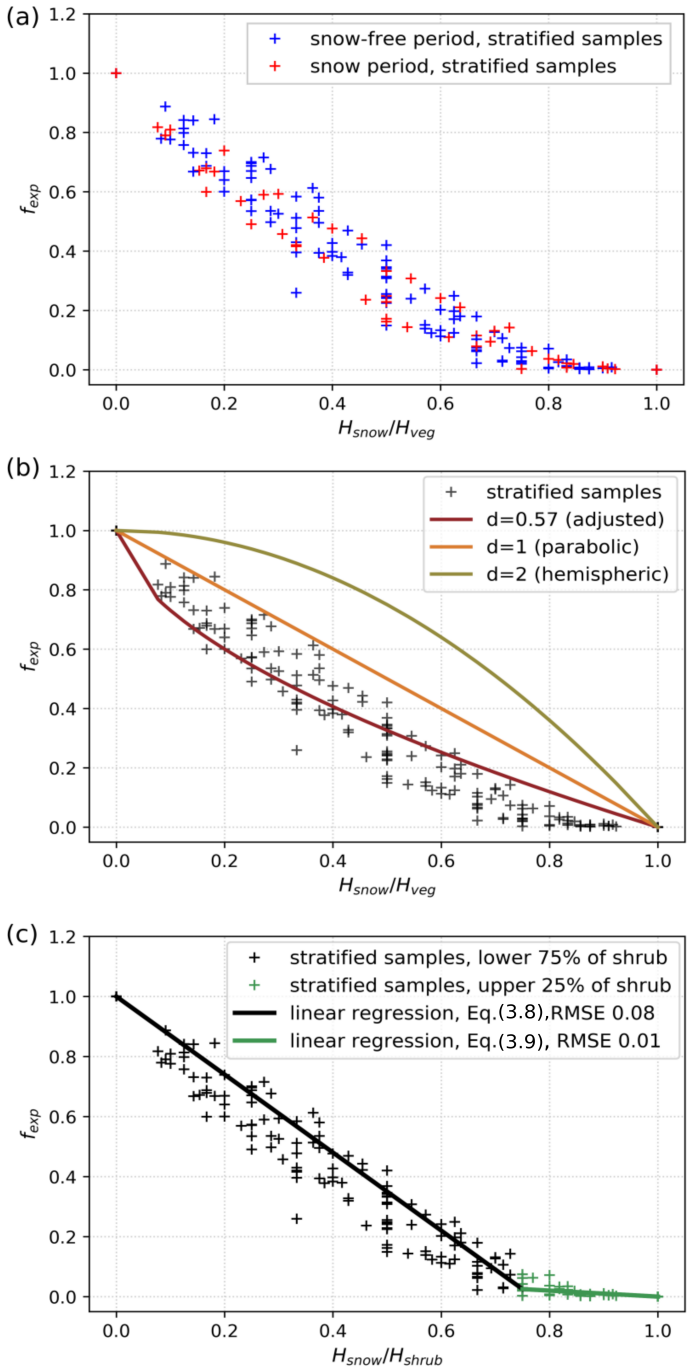

Figure 3.4. The performance of several exposed-vegetation functions is evaluated against the empirical correlation of shrub fraction covered by snow (H_{snow}/H_{veg}) and exposed-vegetation factor f_{exp}. (a) Empirical correlation determined from stratified samples. No difference is detectable between summer samples (blue crosses) and winter samples (red crosses). (b) Performance of Eq. (3.5) with a shape factor d set to 1 (orange), to 2 (dark-green) or a shape factor of 0.57 determined with a least-square approach (brown). Neither approach could accurately reproduce the empirical data (black crosses). (c) A good fit with the empirical data was achieved by using two linear regressions, one for the lower 75 % of shrubs (black) and a second one for the upper 25 % of shrubs (green).

Figure 3.4b shows the fit between the empirical data and the two versions of the Eq. (3.5) found in the literature. In these equations, the shape factor *d* is either set to 1 for parabola-shaped shrubs (orange line) or to 2 for hemisphere-shaped shrubs (dark-green line). We found that both versions largely overestimated f_{exp} and thus failed to reproduce the measured data. We therefore used a non-linear least-squares method to determine the best-fitting value for *d* and found that setting *d* equal to 0.57 returned a good fit (brown line) with a RMSE of 0.08 and R^2 of 0.95. While the fit is greatly improved, the residuals are not randomly distributed as the function underestimates f_{exp} for low H_{snow}/H_{veg} values but overestimates f_{exp} for high H_{snow}/H_{veg} values.

In order to find a well-fitting regression with randomly distributed residuals, we tested an alternative approach (Figure 3.4c) where we used two linear regression curves. The first was fitted to the stratified data from 0 (bottom) to 75 % of the shrub height. The second curve was fitted to the data from 75 % to the top. The equation for the lower part of the shrub is of the form:

$$f_{\exp} = 1 - 1.3 \cdot \left(\frac{H_{snow}}{H_{veg}} \right), \tag{3.8}$$

and that for the upper part:

$$f_{\exp} = 0.1 - 0.1 \cdot \left(\frac{H_{snow}}{H_{veg}} \right). \tag{3.9}$$

This twofold linear approach fitted the stratified shrub data very well. RMSE values were 0.08 and 0.01 and R^2 values were 0.98 and 0.71 for Eq. (3.8) and (3.9), respectively. There was no systematic pattern of overestimation or underestimation.

3.4.3.3 Weighting factors χ and simulated and observed albedo

To obtain information about the predictive power of the allometric approach, we compared weighting factors from the adjustment approach (χ_{adj}) in Belke-Brea et al. (2019) with the allometric approach in this study (χ_{calc}). The former are considered to be reference values.

Figure 3.5a shows χ_{calc} values calculated with the global allometric regression (Figure 3.3, black curve) and Eq. (3.5) using the three different shape factors, i.e. 1, 2 and 0.57. As expected from Figure 3.4b, shape factors equal to 1 and 2 largely overestimated χ_{calc}. The deduced shape factor (0.57) returned a better fit (RMSE=0.09, R^2=0.77). However, it overestimated χ_{calc} for shrubs that are almost entirely snow-covered. It also slightly underestimated χ_{calc} for shrubs protruding high above the snow. This highlights how sensitive χ_{calc} calculations are to inaccuracies in the exposed-vegetation function. Figure 3.5b shows the results of the twofold approach (Eq. (3.8) and (3.9)) used respectively with the global, valley and coast allometric regression curves shown in Figure 3.3. The overall fit was improved compared to the approach with Eq. (3.5). The valley and global regression performed similarly well and had both a RMSE of 0.04 and a R^2 of 0.94. The values calculated with the valley regression tended to be slightly lower than those calculated with the global regression. The coast regression performed less well with an RMSE of 0.08 and an R^2 of 0.80. It especially overestimated χ_{calc} values for high protruding shrubs. The similar performance of the global and the valley regression curve is not surprising. Both functions are similar due to the relatively larger number of shrubs sampled in the valley, i.e. 19 valley shrubs vs. 11 coast shrubs.

Table 3.1. Fitted coefficients for the global and location-specific allometric equations (Eq. (3.2)) and their standard errors..

	a	Δa	b	Δb
Global	0.0781	0.0289	0.4903	0.0896
Valley	0.0509	0.0197	0.5647	0.0905
Coast	0.0578	0.0452	0.6203	0.1996

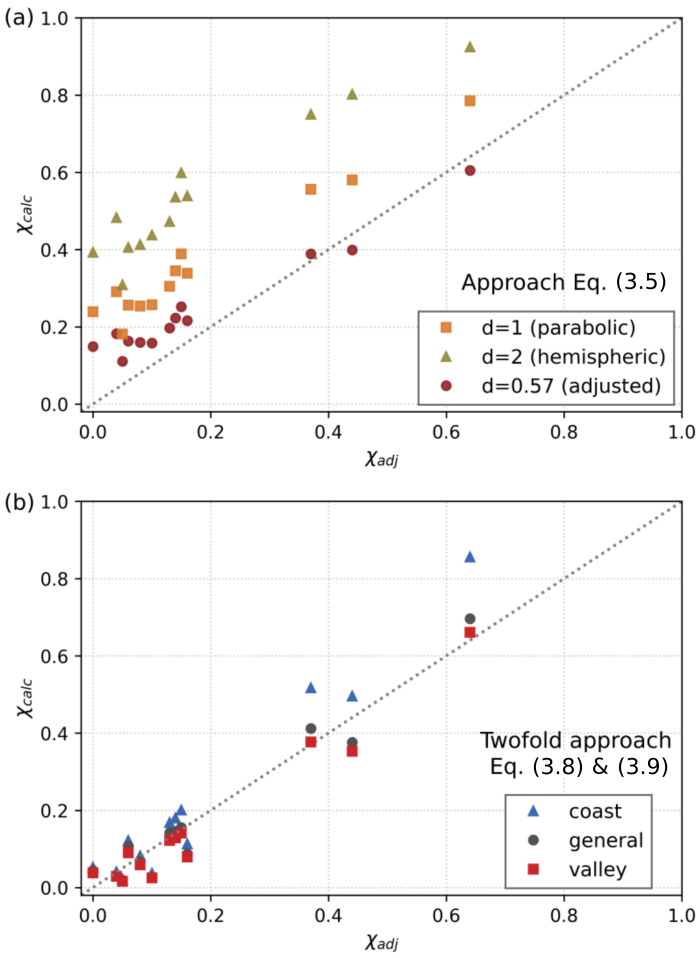

Figure 3.5. Correlation of adjusted weighting factors (χ_{adj}) and calculated weighting factors (χ_{calc}). The former were taken from Belke-Brea et al. (2019) and are considered reference values. (a) χ_{calc}-values were calculated with Eq. (3.5), the commonly used exposed-vegetation function, with a shape factor d set to 1 (orange), 2 (dark-green) or 0.57 (brown). (b) χ_{calc}-values were calculated with Eq. (3.8) and Eq. (3.9) and either the coast allometry (blue), the valley allometry (red) or the global allometry (gray). The 1:1 line had been drawn as a visual aid.

Figure 3.6 shows examples of measured and simulated albedo for 22 November 2015 when shrubs still protruded high above the snow. In Figure 3.6a we tested the model sensitivity to the choice of exposed-vegetation function. Albedo was simulated respectively with Eq. (3.5) from the literature and the new twofold approach shown in Eq. (3.8) and Eq. (3.9). For the simulation with Eq. (3.5) we set the shape factor to 1 because this corresponds to the most commonly used setting in models (Liston and Hiemstra 2011, Ménard et al. 2014a). Simulations with Eq. (3.5) strongly underestimated albedo (RMSE 0.118). In contrast, the spectra calculated with the twofold approach fitted the observed data well

(RMSE 0.007). This indicates that albedo simulations are highly sensitivity to the choice of the exposed-vegetation function. Figure 3.6b shows spectra simulated with the well-performing twofold approach and the valley, coast and global allometric equations, respectively. Using global allometry returned the best-fitting simulations (RMSE of 0.007) which was unexpected as all albedo measurements were conducted in the valley, intuitively suggesting that valley allometry should return the best-fitting simulations.

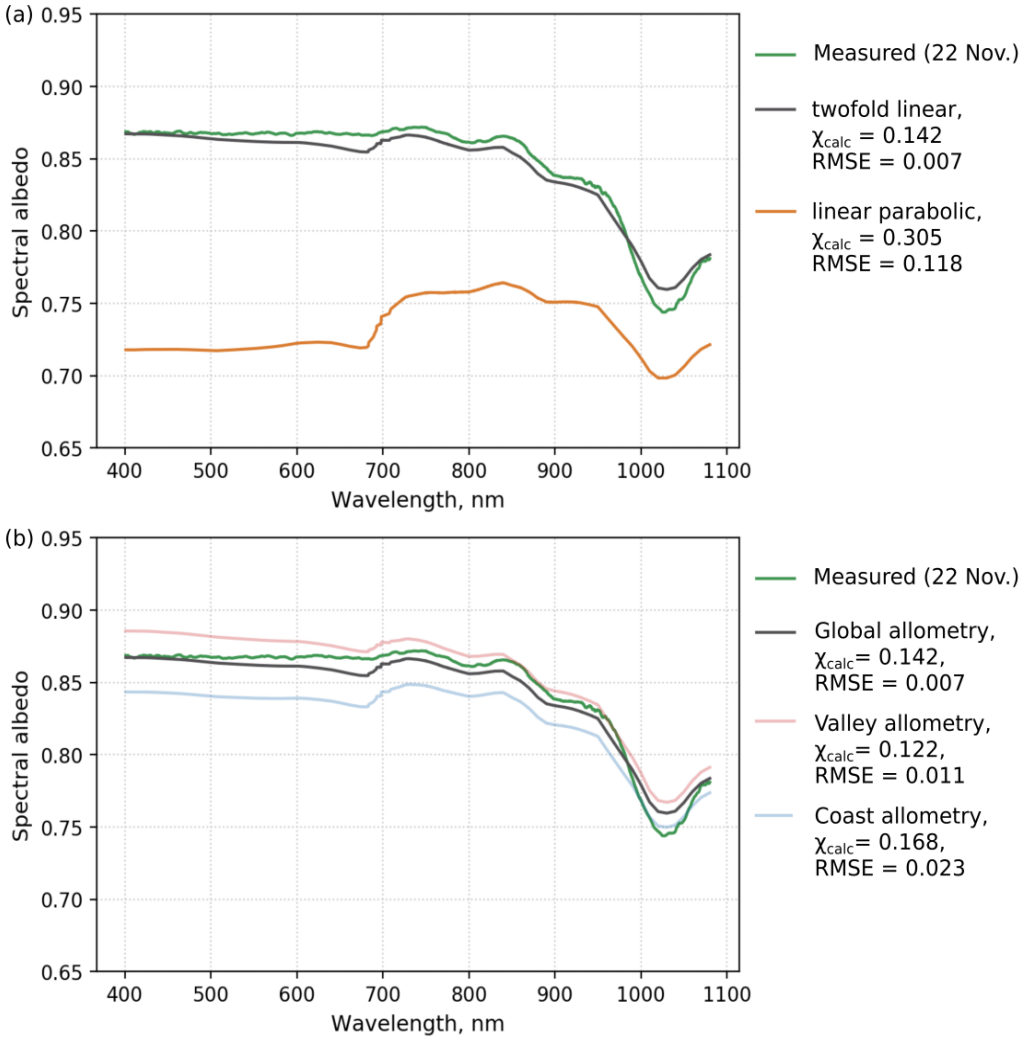

Figure 3.6. Example highlighting model sensitivity to the choice of exposed-vegetation function and allometric equation. Measured albedo, taken on 22 Nov. in the valley near Umiujaq, is shown together with (a) two spectra simulated with different exposed-vegetation functions and (b) three spectra simulated with different allometric equations. All simulated spectra in (b) were calculated using the twofold approach (shown in Eq. (3.8) and (3.9)). The best fit between measured and modeled data was achieved by using the twofold approach together with global allometry (green curve).

A more general overview of model performance was obtained by analyzing the fit of all 31 measured spectra with the corresponding simulations. Simulations were conducted with the twofold approach and either the valley, global or coast allometry. Model accuracy was good for simulations that used global and valley allometry returning average RMSE of 0.028 ± 0.017 (global) and 0.028 ± 0.019 (valley). Model accuracy decreased for simulations with coast allometry returning average RMSE of 0.042 ± 0.033. To detect patterns of systematic overestimation or underestimation, average residuals were respectively calculated for the simulations with global, valley and coast allometry (Figure 3.7). Here, positive residuals show that the model underestimates albedo ($\alpha_{mix,measured} > \alpha_{mix,model}$), while negative residuals indicate the model overestimating albedo ($\alpha_{mix,measured} < \alpha_{mix,model}$). Residuals for albedo simulated with global allometry were close to 0 at longer wavelengths (850–1080 nm) indicating a random distribution. For shorter wavelengths (400–850 nm), residuals were negative indicating that, in this part of the spectrum, simulated albedo was consistently higher than measured values. Residuals for albedo simulated with valley allometry were negative throughout the whole spectrum (400–1080 nm). This indicates a systematic overestimation of simulated albedo. Averaged over the entire spectrum, simulated albedo was increased by 1.8 % compared to measured values. The difference between simulated and measured albedo increased for shorter wavelengths reaching the maximum at 400 nm, where simulated albedo was higher by 4.0 %. In contrast, using coast allometry caused simulated albedo to be consistently lower than measured values by, on average, 1.9 %.

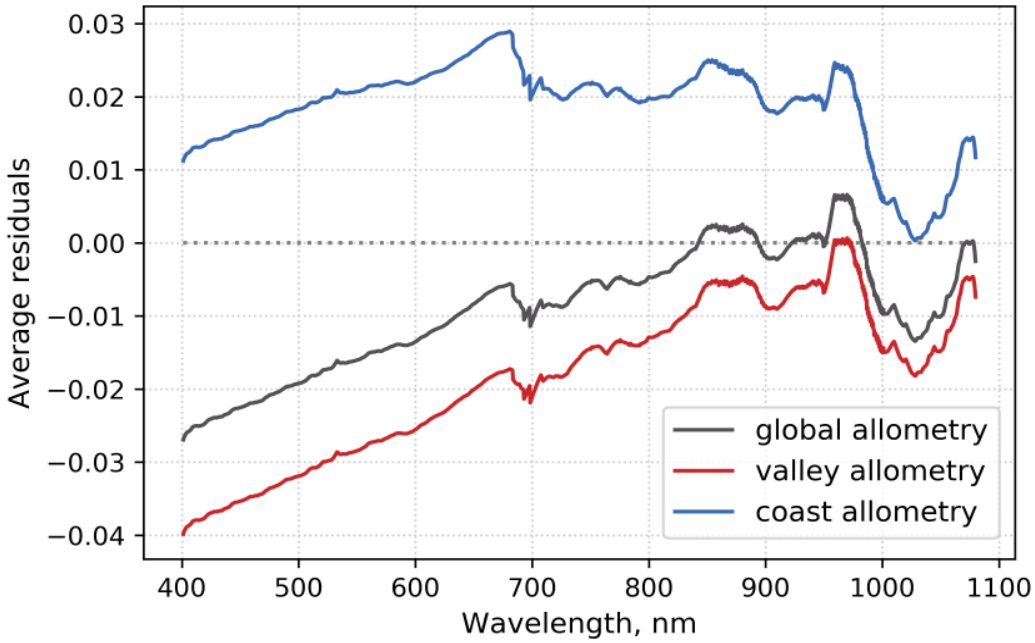

Figure 3.7. Average residuals of 31 measured albedo spectra and the corresponding simulated spectra, the latter calculated either with valley allometry (red), global allometry (grey) or the coast allometry (blue). The average residuals show that albedo was underestimated when calculated with coast allometry, slightly overestimated when calculated with global allometry and more significantly overestimated when calculated with valley allometry.

Errors propagated from the allometric equations to χ_{calc} and α_{mix} were calculated with the variance formula of Gauss using the equations shown in the Appendix B2. Using the variance formula has the advantage that the error equations have an analytical solution. However, it has the disadvantage that errors tend to be overestimated, especially when errors are propagated through several equations like in this study. Errors were therefore relatively large for surfaces with high protruding branches. For example, in Figure 3.6b the weighting factor calculated with the global allometry and the twofold approach was 0.14 and had a propagated error of ± 0.16. The error for the resulting simulated albedo (Figure 3.6b, grey curve) is wavelength-dependent and larger for shorter wavelengths. At 400 nm albedo was 0.87 with an error of ± 0.15 whereas at 1080 nm albedo was 0.78 with an error of ±0.06. We decided not to show errors in Figure 3.5 and 3.6 for the sake of readability and clarity. However propagated errors for all weighting factors calculated with the global allometry and the twofold approach are shown in Appendix B (Figure B1).

3.4.4 Discussion

3.4.4.1 Allometric relationship $H_{veg} - BAI_{total}$

The $H_{veg} - BAI_{total}$ location-specific regression curves showed a good fit with the sample data (Figure 3.3). The fit could probably be improved by sampling more shrubs, however this is difficult to realize due to the time-consuming and destructive nature of the sampling approach. Moreover, the number of shrubs sampled seemed to be high enough to determine representative $H_{veg} - BAI_{total}$ correlations as the established regression curves yielded good albedo simulations results.

A location-dependence of the $H_{veg} - BAI_{total}$ correlation was clearly visible in the sample data, despite the relative proximity of the two main harvesting sites (i.e. a distance of ~ 8 km from the village to the northwestern coast of the lake Guillaume-Delisle, Figure 3.1). In particular, we measured larger BAI_{total} values for coast shrubs. We found, by counting the branches that were cut per shrub specimen, that coast shrubs also had on average 30 % more branches indicating a denser branch network. The denser network is most likely a phenotypic response to the mechanical stress of strong coastal winds. Mechanical stress is known to increase radial growth and to result in sturdier plants (Biddington 1986, Anten et al. 2009, Onoda and Anten 2011). To test this hypothesis, we obtained wind speed data for the year 2013 from an automatic weather station located 10 m from the shore in Umiujaq and compared them to the wind speed data of 2013 recorded by the weather station in the Tasiapik Valley (Figure 3.1). Both stations used a Young anemometer which was attached at the top of a 10 m tower. Wind speed on the coast was almost always greater than in the valley. More specifically, in the valley wind speeds of >5 m s^{-1} were reached 32 % of the time whereas at the coast they were reached 56 % of the time. A figure showing the wind speed distribution curves for the coast and the valley station can be found in Appendix C (Figure C1). Other environmental and ecosystem factors like snow conditions, temperature as well as soil, water and nutrient availability could have had an additional influence on shrub growth. These observations show that it is important to consider environmental conditions of the study sites before choosing allometric equations for albedo calculations.

Here, allometric relationships were established for overcast conditions with diffuse light. In those illumination conditions, we assumed that the illuminated branch surface corresponds

simply to the cross-sectional branch surface. Calculating the illuminated surface for clear sky conditions with direct light is more complicated because the illuminated surface becomes a function of the position of the sun and the angular distribution of branches. A future study could test the suitability of the allometric approach for clear-sky albedo simulations by extending the existing data set of branch diameter and length measurements with information about the angular distribution of branches. Given the zenith angle constraint on the accuracy of optical measurements, clear sky measurements should be made in spring. Furthermore, since most shrubs are totally covered by snow before snowmelt, such measurements should be made after snowmelt started. This limits the suitable timing to a 2-week period, the exact happening of which varies from year to year, making logistical planning difficult.

3.4.4.2 f_{exp} and the exposed-vegetation function

The correlation between f_{exp} and H_{snow}/H_{veg} (Figure 3.4a) was similar for all shrubs independent of sampling location or shrub height. This was not surprising since shrubs of the same species have a resembling shape and are therefore expected to have a similar vertical distribution of branch surface area. The shape was also similar for shrubs sampled during the snow-free period and the snow cover period and it seems therefore that no shrub bending took place. This observation differs from previous studies who observed shrub bending in birches (Sturm et al. 2005A, Pomeroy et al. 2006). This difference may be because shrub bending in the literature was mainly observed for tall shrubs, with long, supple branches. This description does not fit the growth architecture of *Betula glandulosa* which had stiff branches with many ramifications. Stiff shrubs are less prone to branch bending (Sturm et al. 2005) and we suggest that they instead undergo homothetic compaction, which means that the height of branches above the ground at all points was reduced by a constant factor. Homothetic compaction would explain why there was no change in the relative vertical distribution of branch surface area. The homothetic compaction hypothesis is also concurrent with cursory observations we made during shrub sampling in winter where we saw shrubs expand after removing snow within the 10 cm vertical strata. An advantage of the presence of stiff, homothetically compacted shrubs is that it simplifies the calculation of f_{exp} and χ_{calc} and the simulation of albedo because the

bending factor in Eq. (3.5) can be set to 1.

It was tested how well the different exposed-vegetation functions reproduced the sampled f_{exp}-values (Figure 3.4b and 3.4c). We found that the commonly used exposed-vegetation function (Eq. (3.5)) strongly overestimated f_{exp}-values (Figure 3.4b), both when setting the shape factor to 1 for parabolic-shaped shrubs or to 2 for hemispheric-shaped shrubs. Using instead a fitted shape factor equal to 0.57 increased the fit. However, it still overestimated f_{exp}-values for shrubs that are almost snow-covered and underestimated f_{exp} for highly protruding shrub. This suggests that Eq. (3.5) is generally poorly suited to describe the shape of the *B. glandulosa* shrubs sampled in this study. A better fit was achieved with a twofold approach where the data for the lower 75 % and the upper 25 % of shrubs were fitted separately with a linear regression (Figure 3.4c). The good performance of the twofold approach suggests that a structural change occurs at the 75-25 % transition. A similar observation was made by Paradis et al. (2016) who studied the vertical distribution of woody biomass and found that for tall shrubs (> 40 cm) the woody biomass tended to decline sharply in the upper 2 to 3 highest 10 cm strata. A possible interpretation for this structural change is that it marks the transition between branches and twigs. Branches in the lower strata are thicker because they had a longer period of wood accumulation and because they are dominated by radial growth which increases their diameter. In contrast twigs in the upper strata are long and thin because they were formed by primary growth which leads to axis elongation. This change in form could explain the observed reductions in branch surface area and woody biomass (Paradis et al. 2016). Moreover, Paradis et al. (2016) found that the vertical growth rates of *B. glandulosa* depend on shrub height and are larger for large shrubs than for smaller shrubs. This could explain why the shift from branches to twigs is marked by a relative and not an absolute transition (75 %:25 %) and is thus similar for shrubs of different heights. Further research is necessary to determine whether a similar transition is also found for *B. glandulosa* shrubs at other study sites and more generally for other shrubs species currently expanding in the Arctic tundra like *Betula nana*, *Salix spp* and *Alnus crispa* (Tape et al. 2006).

3.4.4.3 Albedo simulations

Overall the allometric modeling approach developed here can accurately compute χ_{calc}

values and mixed surface albedo. There is a good agreement between χ_{calc} and the χ_{adj} values determined in Belke-Brea et al. (2019) (R^2=0.94). Albedo simulations achieved an accuracy of around 3 % (measured by the RMSE). However, the performance of the model depends strongly on the form of the exposed-vegetation function. Using the equation which is implemented in most LSMs and tundra models, Eq. (3.5) with a shape factor set to 1, resulted in a significant overestimation of χ_{calc} (Figure 3.5a) and underestimation of albedo (Figure 3.6a). This shows how crucial it is for models to use exposed-vegetation functions which were specifically established for Arctic shrubs, like here the twofold approach. Using a specialized equation ensures accurate calculations of mixed surface albedo and a reliable quantification of the effect of shrub-induced surface darkening on climate warming.

Model performance depended also on the choice of the allometric equation. Here, two location-specific allometric equations were established, one for coast shrubs and one for valley shrubs, and applying the different equations changed model accuracy by 1.4 %. In particular, model accuracy was 4.2 % when using coast allometry and improved to 2.8 % when using valley allometry. This was an expected result as all albedo and height measurements were conducted in the valley. However, it was unexpected that applying the more general global allometry equation returned the same model accuracy as using the valley allometry. This similar performance of the valley and global allometry may be explained by the wind-exposed location of the albedo measuring site in the upper part of the valley (Figure 3.1) which may have caused some shrub specimens to grow sturdier than the average shrub in the valley. In those particular cases, using global allometry would return a better fit than the valley allometry equation leading to similar average accuracy values. However, considering the non-random distribution of residuals for simulations with valley allometry, it is also possible that the model contains a systematic error. This error could have caused simulated albedo to be higher than measured values by around 2 %. The good performance of global allometry is then due to a partial compensation of this systematic error. Simulations that used coast allometry tended to underestimate albedo. This suggests that in those cases the systematic error was overcompensated by the relatively large BAI_{total} values calculated with the coast allometry equation. Consequently, the impact of choosing a correct location-specific equation, which fits the environmental conditions of the study site, may increase in a model where the systematic error is

corrected. The change in model accuracy of 1.4 % due to different allometric equations is thus considered to be a minimal value.

The residuals calculated for simulations that used valley and global allometry showed a continuous decrease from 850 nm to 400 nm. This leads to the assumption that the systematic error was caused by a process which increases light absorption, particularly at these wavelengths. There are two light-absorbing processes which may have reduced measured albedo but were not considered in the model. First, light-absorbing impurities in the snowpack are known to absorb light in the visible range (e.g. Warren and Wiscombe 1980, Jacobson 2004) which is consistent with the range of the systematic error. Impurities were neglected here mainly because of the lack of information on the concentration and absorption spectrum of impurities in the snowpack in Umiujaq. Secondly, only branches that protruded above the snow were considered, but light is known to penetrate several centimeters into the snowpack (France et al. 2011). Buried branches may therefore also absorb incoming radiation. Light absorption by buried branches increases the effectively illuminated branch area and, as a result, reduces albedo. The next step to obtain a model accuracy of less than 1 % would be to quantify the impact of those processes on albedo and determine if one or both processes could explain the observed albedo overestimation of around 2 %. For this we suggest that the impact of impurities on albedo in Umiujaq be quantified by collecting snow samples and determining impurity concentration as well as conducting a spectral analysis on those impurities. Furthermore, to quantify the impact of branches that absorb light underneath the snow surface, vertical absorption profiles could be measured, as in Libois et al. (2014), at sites where snow is intermingled with shrub branches.

3.4.5 Conclusion

The structural analysis of Arctic *B. glandulosa* shrubs improved simulations of mixed surface albedo in two important ways. First, the structural data revealed that the exposed-vegetation function commonly used in LSMs and tundra models cannot reproduce the shape of shrubs in this study. These functions assume a parabolic or hemispheric shape of shrubs. However, data on shrub architecture in this study suggests that a structural change occurs in Arctic shrubs at the 75:25 % transition. This transition could mark the change

between branches in the lower part of the shrub and twigs in the upper part. Therefore, a better-fitting approach was established. In this new approach, the lower and upper part of the shrubs are fitted with two separate linear equations. Second, an allometric approach was developed linking the illuminated BAI of shrubs to shrub height. This represents an improvement over determining BAI from image analysis because it allows to calculate BAI values continuously for an entire snow season. It also allows to predict BAI values for projected scenarios where shrub height increases. We found that sampling 19 shrub specimen resulted in representative allometric relationships. We further found, that allometric relationships for Arctic shrubs depend on environmental conditions. Shrubs growing in wind-exposed areas are sturdier and have 30 % to 50 % higher BAI values.

Overall, using the allometric relationships and the new exposed-vegetation function returned accurate albedo simulations. Model accuracy was ~ 3 % (measured by the RMSE). It was important to choose allometric equations adapted to the environmental conditions of the albedo measuring site, otherwise simulation accuracy was reduced by around 1 %. The model tended to overestimate albedo by around 2 %, probably due to the assumption of zero impurities in the snowpack or because the absorption of branches below the snow had not been considered.

We conclude that the model presented is a suitable tool to calculate χ_{calc} and mixed-surface albedo. To make the model more widely applicable and achieve an accuracy better than 1%, future studies need to consider a few further steps. These include: 1) identify and correct the source of the systematic overestimation of 2 %, 2) test the performance of the established equations with shrub data from other study sites, 3) determine allometric and exposed-vegetation equations for other shrub species that are rapidly expanding in the Arctic, 4) assemble all shrub-specific equations in an allometric database for shrubs similar to the GlobAllomeTree database for trees (http://globallometree.org/) and 5) to combine the allometric approach with a bending model like that of Ménard et al. (2014b). The model could then be easily implemented in LSMs and climate models, finally allowing the calculations of reliable estimates of the current and projected impact of Arctic shrubification on global and regional warming.

Acknowledgements. This work was funded by the BNP Paribas foundation (APT project), NSERC through the discovery grant program to FD and the French Polar Institute (IPEV) through program 1042 to FD. We thank the community of Umiujaq for their hospitality and support in the field. We are also grateful to the Centre d'Études Nordiques (CEN) for providing and maintaining the Umiujaq Research Station.

References

Anten, N. P. R., E. J. Von Wettberg, M. Pawlowski, and H. Huber. 2009. Interactive Effects of Spectral Shading and Mechanical Stress on the Expression and Costs of Shade Avoidance. *The American Naturalist.* 173 (2): 241-255. doi:10.1086/595761.

Barrere, M., F. Domine, M. Belke-Brea, and D. Sarrazin. 2018. Snowmelt Events in Autumn Can Reduce or Cancel the Soil Warming Effect of Snow–Vegetation Interactions in the Arctic. *Journal of Climate.* 31 (23): 9507–18. doi:10.1175/JCLI-D-18-0135.1.

Belke-Brea, M., F. Domine, M. Barrere, G. Picard, and L. Arnaud. 2019. Impact of Shrubs on Surface Albedo and Snow Specific Surface Area at a Low Arctic Site : In-Situ Measurements and Simulations. *Journal of Climate. 33 (2):* 597–609. doi:10.1175/JCLI-D-19-0318.1.

Berner, L. T., H. D. Alexander, M. M. Loranty, P. Ganzlin, M. C. Mack, S. P. Davydov, and S. J. Goetz. 2015. Biomass Allometry for Alder, Dwarf Birch, and Willow in Boreal Forest and Tundra Ecosystems of Far Northeastern Siberia and North-Central Alaska. *Forest Ecology and Management.* 337: 110–18. doi:10.1016/j.foreco.2014.10.027.

Best, M. J., M. Pryor, D. B. Clark, G. G. Rooney, and R. L. H. Essery. 2011. Model Development The Joint UK Land Environment Simulator (JULES), Model Description – Part 1 : Energy and Water Fluxes. *Geoscientific Model Development.* 4(1): 677-699. doi:10.5194/gmd-4-677-2011.

Biddington, N. L. 1986. The Effects of Mechanically-Induced Stress in Plants - a Review (MIS). *Plant Growth Regulation.* 4: 103–23.

Bond-Lamberty, B., C. Wang, and S. T. Gower. 2002. Aboveground and Belowground Biomass and Sapwood Area Allometric Equations for Six Boreal Tree Species of Northern Manitoba. *Canadien Journal of Forest Research*. 38(2):1441-1450. doi:10.1139/X02-063.

Boone, A., P. Samuelsson, S. Gollvik, A. Napoly, L. Jarlan, E. Brun, and B. Decharme. 2017. The Interactions between Soil – Biosphere – Atmosphere Land Surface Model with a Multi-Energy Balance (ISBA-MEB) Option in SURFEXv8 – Part 1 : Model Description. *Geoscientific Model Development.* 10: 843–72. doi:10.5194/gmd-10-843-2017.

Chapin, F. S., M. Sturm, M. C. Serreze, J. P. McFadden, J. R. Key, A. H. Lloyd, A. D. McGuire, et al. 2005. Role of Land-Surface Changes in Arctic Summer Warming. *Science.* 310(5748): 657–60. doi:10.1126/science.1117368.

de Noblet, N. I., I. C. Prentice, S. Joussaume, D. Texier, A. Botta, and A. Haxeltine. 1996. Possible Role of Atmosphere-Biosphere Interactions in Triggering the Last Glaciation. *Geophysical Research Letters.* 23(22): 3191–94.

Domine, F., A. S. Taillandier, S. Houdier, F. Parrenin, W. R. Simpson, and T. A. Douglas. 2007. Interactions between Snow Metamorphism and Climate: Physical and Chemical Aspects. *Physics and Chemistry of Ice, Proceedings of the International Conference on the Physics and Chemistry of Ice, 11th, Bremerhaven, Germany, July 23-28, 2006*, 27–46.

France, J. L., M. D. King, M. Frey, J. Erbland, G. Picard, S. Preunkert, A. MacArthur and J. Savarino. 2011. Snow Optical Properties at Dome C, (Concordia), Antarctica: Implications for Snow Emissions and Snow Chemistry of Reactive Nitrogen. *Atmospheric Chemistry and Physics.* 11(18): 9787-9801. doi:10.5194/acp-11-9787-2011.

Gagnon, M., F. Domine, and S. Boudreau. 2019. The Carbon Sink due to Shrub Growth on Arctic Tundra : A Case Study in a Carbon-Poor Soil in Eastern Canada. *Environmental Research Communications.* 1(9): 091001.

Gallet, J.-C. C., F. Domine, C. S. Zender, and G. Picard. 2009. Measurement of the Specific Surface Area of Snow Using Infrared Reflectance in an Integrating Sphere at 1310 and 1550 nm. *The Cryosphere.* 3(2): 167–82. doi:10.5194/tc-3-167-2009.

Jacobson, M.-Z. 2004. Climate Response of Fossil Fuel and Bio-Fuel Soot, Accounting for Soot's Feedback to Snow and Seaice Albedo and Emissivity. *Journal of Geophysical Research.* 109(D21). doi:10.1029/2004JD004945.

Jahn, A., M. Claussen, A. Ganopolski, and V. Brovkin. 2005. Quantifying the Effect of Vegetation Dynamics on the Climate of the Last Glacial Maximum. *Climate of the Past.* 1: 1–16.

Jenkins, J. C., D. C. Chojnacky, L. S. Heath, and R. A. Birdsey. 2003. National-Scale Biomass Estimators for United States Tree Species. *Forest Science.* 49(1):12-35.

Ju, J. C. and J. G. Masek. 2016. The Vegetation Greenness Trend in Canada and US Alaska from 1984-2012 Landsat Data. *Remote Sensing of Environment*. 176: 1-16.

Juszak, I., A. M. Erb, C. Maximov, and G. Schaepman-Strub. 2014. Arctic Shrub Effects on NDVI, Summer Albedo and Soil Shading. *Remote Sensing of Environment.* 153: 79–89. doi:10.1016/j.rse.2014.07.021.

Kucharik, C. J., J. M. Norman, and S. T. Gower. 1998. Measurements of Branch Area and Adjusting Leaf Area Index Indirect Measurements. *Agricultural and Dorest Meteorology* 91: 69–88.

Laberge, M., and S. Payette. 1995. Long-Term Monitoring of Permafrost Change in a Palsa Peatland in Northern Quebec, Canada: 1983-1993. *Arctic and Alpine Research.* 27: 167–71. doi:10.2307/1551898.

Lemay, M. A., L. Provencher-Nolet, M. Bernier, E. Lévesque, and S. Boudreau. 2018. Spatially Explicit Modeling and Prediction of Shrub Cover Increase Near Umiujaq, Nunavik. *Ecological Monographs.* 88(3): 385-407.

Libois, Q., G. Picard, J. L. France, L. Arnaud, M. Dumont, C. M. Carmagnola, and M. D. King. 2013. Influence of Grain Shape on Light Penetration in Snow. *Cryosphere.* 7(6): 1803–18. doi:10.5194/tc-7-1803-2013.

Libois, Q., G. Picard, M. Dumont, L. Arnaud, C. Sergent, E. Pougatch, M. Sudul, and D. Vial. 2014. Experimental Determination of the Absorption Enhancement Parameter of Snow. *Journal of Glaciology.* 60(222): 714–24. doi:10.3189/2014JoG14J015.

Liston, G. E., and C. A. Hiemstra. 2011. Representing Grass – and Shrub – Snow – Atmosphere Interactions in Climate System Models. *Journal of Climate.* 24(8): 2061–79. doi:10.1175/2010JCLI4028.1.

Loranty, M. M., and S. J. Goetz. 2012. Shrub Expansion and Climate Feedbacks in Arctic Tundra. *Environmental Research Letters.* 7(1): 011005. doi:10.1088/1748-9326/7/1/011005.

Loranty, M. M., S. J. Goetz, and P. S. A. Beck. 2011. Tundra Vegetation Effects on Pan-Arctic Albedo. *Environmental Research Letters* 6 (2): 029601. doi:10.1088/1748-9326/6/2/029601.

Marsh, P., P. Bartlett, M. MacKay, S. Pohl, and T. Lantz. 2010. Snowmelt Energetics at a Shrub Tundra Site in the Western Canadian Arctic. *Hydrological Processes.* 24(25): 3603–20. doi:10.1002/hyp.7786.

Ménard, C. B., R. Essery, and J. Pomeroy. 2014a. Modelled Sensitivity of the Snow Regime to Topography, Shrub Fraction and Shrub Height. *Hydrology and Earth System Sciences.* 18: 2375–92. doi:10.5194/hess-18-2375-2014.

Ménard, C. B., R. Essery, J. Pomeroy, P. Marsh, and D. B. Clark. 2014b. A Shrub Bending Model to Calculate the Albedo of Shrub-Tundra. *Hydrological Processes* 28(2): 341–51. doi:10.1002/hyp.9582.

Motulsky, H., and A. Christopoulos. 2005. Fitting Models to Biological Data Using Linear and Non-Linear Regression: A Practical Guide to Curve Fitting. *Statistics in Medicine*. 24. doi:10.1002/sim.2181.

Myers-Smith, I. H., B. C. Forbes, M. Wilmking, M. Hallinger, T. Lantz, D. Blok, K. D. Tape, et al. 2011. Shrub Expansion in Tundra Ecosystems: Dynamics, Impacts and Research Priorities. *Environmental Research Letters.* 6(4): 045509. doi:10.1088/1748-9326/6/4/045509.

Onoda, Y., and N. P. R. Anten. 2011. Challenges to Understand Plant Responses to Wind. *Plant Signaling and Behavior.* 6: 1057–59. doi:10.4161/psb.6.7.15635.

Otto-Bliesner, B. L., and G. R. Upchurch Jr. 1997. Vegetation-Induced Warming of High-Latitude Regions during the Late Cretaceaous Period. *Nature.* 385 (6619): 804-807.

Paradis, M., E. Lévesque, and S. Boudreau. 2016. Greater Effect of Increasing Shrub Height on Winter versus Summer Soil Temperature. *Environmental Research Letters.* 11 (8). doi:10.1088/1748-9326/11/8/085005.

Payette, S. 1976. Les Limites Écologiques de La Zone Hémi-Arctique Entre La Mer D'Hudson et La Baie D'Ungava, Nouveau-Québec. *Cahiers de Géographie Du Québec.* 20(50): 347–64.

Pearson, R. G., S. J. Phillips, M. M. Loranty, P. S. Beck, T. Damoulas, S. J. Knight, and S. J. Goetz. 2013. Shifts in Arctic Vegetation and Associated Feedbacks under Climate Change. *Nature Climate Change.* 3(7): 673–77. doi:10.1038/nclimate1858.

Picard, G., Q. Libois, L. Arnaud, G. Verin, and M. Dumont. 2016. Development and Calibration of an Automatic Spectral Albedometer to Estimate near-Surface Snow SSA Time Series. *Cryosphere.* 10(3): 1297–1316. doi:10.5194/tc-10-1297-2016.

Pokorný, R., and M. V. Marek. 2000. Test of Accuracy of LAI Estimation by LAI-2000 under Artificially Changed Leaf to Wood Area Proportions. *Biologia Plantarum.* 43(4): 537–44.

Pomeroy, J. W., D. S. Bewley, R. L. H. Essery, N. R. Hedstrom, T. Link, R. J. Granger, J. E. Sicart, C. R. Ellis, and J. R. Janowicz. 2006. Shrub Tundra Snowmelt. *Hydrological Processes.* 20(4): 923–41. doi:10.1002/hyp.6124.

Provencher-Nolet, L., M. Bernier, and E. Lévesque. 2014. Short Term Changes Detection in Tundra Vegetation near Umiujaq, Subarctic, Quebec, Canada. *IEEE Geoscience and Remote Sensing Symposium (IGARSS).* 4668–70.

Ropars, P., and S. Boudreau. 2012. Shrub Expansion at the Forest–tundra Ecotone: Spatial Heterogeneity Linked to Local Topography. *Environmental Research Letters.* 7(1): 015501. doi:10.1088/1748-9326/7/1/015501.

Sjöman, J. D., A. Hirons, and H. Sjöman. 2015. Branch Area Index of Solitary Trees: Understanding Its Significance in Regulating Ecosystem Services. *Journal of Environmental Quality.* 45(1):175-187. doi:10.2134/jeq2015.02.0069.

Sprugel, D. G. 1983. Correcting for Bias in Log-Transformed Allometric Equations. *Ecology.* 64(1): 209–10.

Sturm, M., T. Douglas, C. Racine, and G. Liston. 2005. Changing Snow and Shrub Conditions Affect Albedo with Global Implications. *Journal of Geophysical Research.* 110(G1): 1–13. doi:10.1029/2005JG000013.

Sturm, M., J. P. Mcfadden, G. E. Liston, F. S. Chapin III, C. H. Racine, and J. Holmgren. 2001. Snow – Shrub Interactions in Arctic Tundra: A Hypothesis with Climatic Implications. *Journal of Climate.* 14: 336–44.

Sturm, M., J. Schimel, G. Michaelson, J. M. Welker, S. F. Oberbauer, G. E. Liston, J. Fahnestock, and V. E. Romanovsky. 2005. Winter Biological Processes Could Help Convert Arctic Tundra to Shrubland. *BioScience.* 55(1): 17–26. doi:10.1641/0006-3568(2005)055[0017:WBPCHC]2.0.CO;2.

Tape, K., M. Sturm, and C. Racine. 2006. The Evidence for Shrub Expansion in Northern Alaska and the Pan-Arctic. *Global Change Biology.* 12(4): 686–702. doi:10.1111/j.1365-2486.2006.01128.x.

Tremblay, B., E. Lévesque, and S. Boudreau. 2012. Recent Expansion of Erect Shrubs in the Low Arctic: Evidence from Eastern Nunavik. *Environmental Research Letters. 7*(3): 035501.

Verseghy, D. 2009. Class – the Canadian Land Surface Scheme (Version 3.4) - Technical Documentation. *Climate Research Division, Science and Technology Branch, Environment Canada*. 180.

Wang, A., and X. Zeng. 2009. Improving the Treatment of the Vertical Snow Burial Fraction over Short Vegetation in the NCAR CLM3. *Advances in Atmospheric Sciences.* 26(5): 877–86. doi:10.1007/s00376-009-8098-3.1.

Warren, S. G. 1982. Optical Properties of Snow. *Reviews of Geophysics and Space Physics*. 20(1): 67–89. doi:10.1029/RG020i001p00067. 20.1

Warren, S. G. and W. Wiscombe. 1980. A Model for the Spectral Albedo of Snow II: Snow Containing Atmospheric Aerosols. *Journal of atmospheric Sciences*. 37: 2734-2745.

Chapter 4

On the influence of erect shrubs on the irradiance profile in snow

4.1 Preamble

The first and second part of the results concentrated on shrub influence on surface albedo. In the third part we plunge into the snowpack and investigate the radiative effect of buried branches. Snow-shrub-light interactions in the snowpack have, to our knowledge, never been measured before and this chapter is a first qualitative analysis on the influence of buried branches on the radiation budget in snow. Unfortunately our data did not permit to make a quantitative analysis of the radiative impact of buried branches because impurity concentrations were unexpectedly high. A quantitative analysis would have been necessary to determine the impact of buried branches on albedo and to create a correction term which could have accounted for the systematic overestimation we found when using the coupled allometric-LME approach in Chapter 3.

The results presented in this chapter are also in preparation to be submitted to the peer-reviewed journal *Biogeosciences*.

4.2 Résumé

L’expansion des arbustes dans la toundra arctique transforme les manteaux neigeux en un mélange de neige, d’impuretés et de branches ensevelies. La présence de branches à l’intérieur d’un manteau neigeux peut en altérer le budget radiatif car la neige est un médium translucide dans lequel la lumière peut pénétrer plusieurs dizaines de centimètres. Les branches ensevelies peuvent donc avoir des répercussions importantes sur la

microstructure et le régime thermal de la neige. Pour caractériser l'influence des branches ensevelies sur le transfert radiatif dans la neige, nous avons mesuré des profils d'irradiation dans des manteaux neigeux avec et sans arbustes près d'Umiujaq dans le Bas-Acrtique canadien (56.5°N, 76.5°W) en novembre et décembre 2015. Nous avons utilisé un modèle de transfert radiatif de Monte Carlo pour analyser les profils des sites sans arbustes et montrons que le type d'impureté principal est la suie (black carbon), avec des concentrations allant jusqu'à 185 ng g^{-1}. Ceci nous a permis de différencier l'effet radiatif des impuretés de celui des branches ensevelies. L'analyse des profils d'irradiation de manteaux neigeux avec arbustes montre que l'impact des branches ensevelies était généralement faible, sauf dans les couches où des branches étaient visibles dans les photographies des profils. Ceci suggère que les branches ont un effet très local sur le transfert radiatif lorsqu'elles sont ensevelies dans le manteau neigeux. Cette hypothèse est appuyée par des observations de fonte et de formation de givre de profondeur formant de petites poches autour des branches dans la neige. Les branches ensevelies ont donc un effet sur les propriétés physiques des manteaux neigeux, et cela pourrait avoir des répercussions sur la faune et la flore de l'Arctique, ainsi que sur le régime thermal du pergélisol. Finalement, les concentrations inhabituellement élevées de suie dans la neige près d'Umiujaq sont probablement une conséquence de l'incinération à ciel ouvert des déchets de la communauté voisine. Ceci illustre un impact local important des populations humaines dans le Nord canadien.

4.3 Abstract

The warming-induced expansion of shrubs in the Arctic is transforming snowpacks into a mixture of snow, impurities and buried branches. Because snow is a translucent medium into which light penetrates up to tens of centimeters, buried branches may alter the snowpack radiation budget with important consequences for the snow thermal regime and microstructure. To characterize the influence of buried branches on radiative transfer in snow, irradiance profiles were measured in snowpacks with and without shrubs near Umiujaq in the Canadian Low Arctic (56.5°N, 76.5°W) in November and December 2015. Using the irradiance profiles measured in shrub-free snowpacks in combination with a Monte Carlo radiative transfer model revealed that the dominant impurity type was black

carbon (BC) in variable concentrations up to 185 ng g^{-1}. This allowed the separation of the radiative effects of impurities and buried branches. Irradiance profiles measured in snowpacks with shrubs showed that the impact of buried branches was generally relatively weak, except for layers where branches were also visible in snowpit photographs, suggesting that branches influence snow very locally (i.e. a few centimeters around branches). The local-effect hypothesis was further supported by observations of localized melting and depth hoar pockets that formed in the vicinity of branches. Buried branches therefore affect snowpack properties, with possible impacts on Arctic flora and fauna and on the thermal regime of permafrost. Lastly, the unexpectedly high BC concentrations in snow are likely caused by nearby open-air waste burning, illustrating that the expanding population in the Canadian North can have an important local impact on BC concentrations.

4.4 Main text

4.4.1 Introduction

Due to Arctic warming, erect shrubs are expanding into the tundra biome, replacing low-growing vegetation like grasses, lichen and mosses (Tape et al. 2006, Myers-Smith et al. 2011, Ropars and Boudreau 2012, Lemay et al. 2018). The vegetation change is transforming natural snowpacks, which originally consisted of snow with impurities, to a mix of snow, impurities and branches (Pomeroy et al. 2006, Loranty and Goetz 2012). This has a large influence on the snow radiation budget, because branches are much more light-absorbing than snow in the visible range (Juszak et al. 2014, Belke-Brea et al. 2019). Numerous experimental and model-based studies have investigated the albedo-reducing effect of branches that protrude above the snow surface (e.g. Sturm et al. 2005, Pomeroy et al. 2006, Liston et al. 2002, Loranty et al. 2011, Ménard et al. 2014, Belke-Brea et al. 2020). However, little attention has been given to the potential effects of branches that are buried in the snowpack.

Snow is a translucent medium into which light can penetrate 20 to 40 cm deep, depending on the wavelength and snow physical properties (France et al. 2011, Tuzet et al. 2019). Light penetration and transmittance are important parameters influencing photochemical processes (Grannas et al. 2007, Domine et al. 2008, France et al. 2011) and the thermal

regime of the snowpack (Flanner and Zender 2005, Picard et al. 2012). In turn, the thermal regime controls snow melt rates in spring and during warm spells in autumn, which is of crucial importance for many bio-geophysical processes in the tundra ecosystem and for Arctic climate (Walker et al. 1993). For example, snow melt timing impacts hydrological processes (Pomeroy et al. 2006), permafrost thawing (Romanovsky et al. 2010, Johansson et al. 2013), energy and mass exchanges between the surface and the atmosphere (Groendahl et al. 2007), hibernation behavior of Arctic fauna (Berteaux et al. 2017, Domine et al. 2018) as well as the growing season length of Arctic flora (Cooper et al. 2011, Semenchuk et al. 2016). Moreover, the depth of light penetration and the amount of transmitted light both impact the microstructure of the snowpack: they influence the formation of melt-freeze grains and the degree of temperature gradient metamorphism (Aoki et al. 2000, Domine et al. 2007). Because the insulating properties of a snowpack depend on its microstructure, light distribution in snow could ultimately affect the permafrost thermal regime and its thawing rate due to climate change (Domine et al. 2011, Pelletier et al. 2018). These complex processes highlight the importance of studying snow-light interactions in the snowpack and understanding how buried branches may alter these processes.

In natural snowpacks, light propagation is strongly influenced by light-absorbing particles (LAP) but also by buried branches. Studying the radiative forcing of LAP in snow, identifying typical LAP types, and quantifying LAP concentrations on a global scale has been an active field of study over the last decades (e.g. Warren and Wiscombe 1980, Hansen and Nazarenko 2004, Doherty et al. 2010, Skiles et al. 2018, Tuzet et al. 2019). It is now known that LAPs increase light absorption in the UV and visible spectrum (350–750 nm), where the absorption by ice is extremely weak, but that their effect is negligible in the near-infrared spectrum (>1000 nm) where ice itself is sufficiently absorptive (Picard et al. 2016, Warren 2019). Each type of LAP has a specific wavelength-dependent absorption efficiency (Figure 4.1), which creates a characteristic shape in plots of spectral absorption measured in snow (Bond et al. 1999, Grenfell et al. 2011, Dal Farra et al. 2018). Due to this spectral signature, optical measurements can be used to not only separate different types of LAP but also measure their respective concentrations in snowpacks. The most absorbing impurity commonly found in snow is black carbon (BC), but significant concentrations of

mineral dust are also found in windy and mountainous regions or close to deserts (e.g. Ramanathan et al. 2001, Painter et al. 2007, Moosmüller et al. 2009, Dang et al. 2017). BC concentrations across the Arctic vary between 4 ng g^{-1} in Greenland and 60 ng g^{-1} in Arctic Russia and Scandinavia (Doherty et al. 2010). The principal source of BC over wide areas in the Arctic is the anthropogenic emissions due to the incomplete combustion of biomass and fossil fuels (Diehl et al. 2012, Bond et al. 2004). The polluted air is transported to the Arctic by atmospheric circulation where it deposits on the snowpack in varying concentrations (from 5 to 50 ng g^{-1}; Rahn and McCaffrey 1980, Cess 1983). Additionally, there is an increasing number of local sources of BC in the Arctic, like ship emissions or the open-air burning of waste that further increase BC air concentrations (Abbatt et al. 2019). Besides LAP, buried branches also have an effect on light transmission and absorption because branches are highly light-absorbing in the visible spectrum (Figure 4.1). However, this effect has not yet been studied, mainly because erect vegetation was mostly absent in high latitudes and high elevation environments, which coincidentally, is where snow is a dominant factor (Stevens and Fox 1991, Holtmeier and Broll 2007). However, shrubs are now expanding northwards due to Arctic warming, and the effect of buried branches on the snow radiation budget in the Arctic tundra may gain in importance.

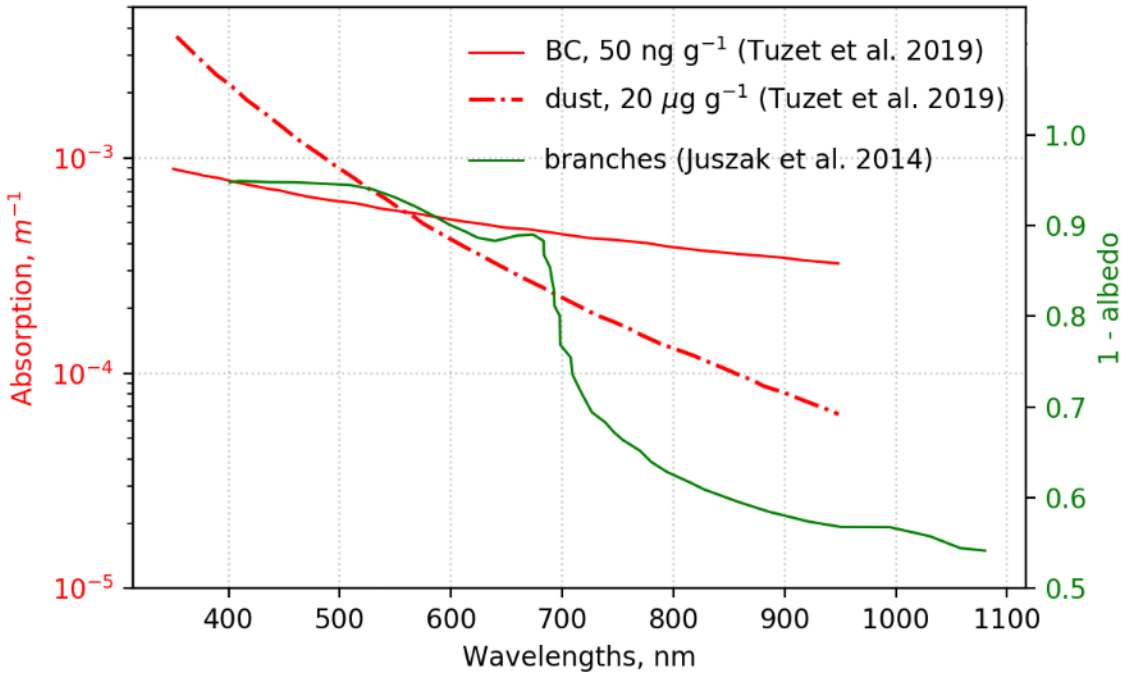

Figure 4.1. Comparison of the spectral absorption of BC (red), dust (red dotted) and the spectral absorption of branches (green). Absorption of branches is illustrated by co-albedo measurements (Juszak et al. 2014). Branch absorption is strongly wavelength dependent and decreases sharply for wavelengths >680 nm.

Irradiance in snow and the effect of LAPs are generally computed numerically with radiative transfer models (Warren and Wiscombe 1980, Hansen and Nazarenko 2004, Aoki et al. 2011, Tuzet et al. 2017). Today, it is possible to calculate radiative transfer through snow as a function of snow physical properties (i.e. snow density and specific surface area (SSA)), using the analytical equations established by Kokhanovsky and Zege (2004). The radiative effect of impurities is calculated for pre-established impurity concentrations from the optical properties that are associated to the different impurity types (i.e. the impurity-specific mass absorption efficiency, MAE). Models have calculated that at concentrations in the 5–50 ng g^{-1} range BC typically reduces albedo from 0 % to 4 %. Albedo reductions of 1–4 % can cause positive radiative forcing of 4–16 W m^{-2} during an average Arctic spring and early summer day, and hence are climatically significant (Warren 2019). Albedo measured over mixed surfaces with snow and protruding branches showed considerably higher albedo reductions of up to 30 % in the broadband (300–2800 nm) and up to 55 % at 500 nm where the contrast between snow and vegetation is most extreme (Sturm et al.

2005, Belke-Brea et al. 2019). These reductions were mostly associated to light absorption by protruding branches and it remains to be tested whether the impact of buried branches in the Arctic tundra could be of the same magnitude as the LAPs mixed in the snowpack. From a radiative transfer modeling point of view, branches and LAP are very different objects. The latter is homogeneously mixed with snow so that its absorption can be averaged and combined with that of the ice, and the classical solution of the radiative transfer equation for homogeneous media applies without any change. In contrast, branches are macroscopic embedded absorbers that affect the path of light, a situation that has no simple analytical solution. To design a model that accurately represents buried branches and allows calculating their specific radiative impact, it is first necessary to acquire basic knowledge about how snow, light and buried branch interact.

This study aims to bring the first insights, to our knowledge, on how buried branches influence light propagation in snowpacks. We present a qualitative analysis where we use a combination of *in situ* measurements and radiative transfer simulations. The latter were computed with the radiative transfer model SnowMCML (Picard et al. 2016) for snowpacks with known snow physical properties and estimated impurity type and concentrations. *In situ* data were acquired during a field campaign in Umiujaq, Northern Quebec (56.5° N, 76.5° W), in autumn 2015 and consisted of (i) vertical spectral irradiance profiles (350–900 nm) measured in snowpacks with and without shrubs, and (ii) vertical profiles of snow density and SSA measured in snowpits. Impurity concentrations and types were estimated by applying two methods which allow retrieving impurity information from optical measurements taken in shrub-free snowpacks. The first method consisted in evaluating the fit between measured and simulated irradiance profiles, where simulated profiles were computed with a range of different impurity types and concentrations. For the second method, extinction coefficients were determined from measured irradiance profiles by using linear regression and the spectral shape of the extinction coefficients was then analysed in order to retrieve information on impurities (Tuzet et al. 2019). The effect of buried branches was investigated by comparing irradiance profiles measured in shrub snowpacks with SnowMCML simulations that include LAPs and irradiance profiles in shrub-free snowpacks.

4.4.2 Study site and data acquisition

4.4.2.1 Study site

Our study site is located near the village of Umiujaq on the coast of Hudson Bay in Nunavik, Northern Quebec (56°33′07″ N, 76°32′57″ E, Figure 4.2). Measurements were taken in Tasiapik Valley, ~4 km from Umiujaq village. The study sites happen to be also ~2 km from a waste disposal site, where waste was occasionally burned in open-air conditions. The measuring sites were situated on a wind-exposed plateau. The plateau is covered with lichen and shrubs, but spruces (mainly *Picea mariana*) are also found in wind-sheltered depressions. Over the last three decades, Nunavik has experienced the strongest greening trend in North America (Ju and Masek 2016). This is due to shrubs expanding in the tundra biome which are replacing lichen patches of mostly *Cladonia spp.* (Ropars and Boudreau 2012, Provencher-Nolet et al. 2014, Gagnon et al. 2019). In the Umiujaq region, the main shrub species are birches (*Betula glandulosa*), willows (mostly *Salix glauca* and *S. planifolia*) and alders (*Alnus viridis* subsp. *crispa*). An automatic weather station has been recording climatic data in the Tasiapik Valley since 1997 (Figure 4.2). From 1997 to 2018, the mean annual air temperature has been -3°C (CEN 2018). In the region of Umiujaq, strong winds and snowstorms are frequent, and wind speeds can reach up to 100 km h-1 (Barrere et al. 2018). The predominant wind direction is from the bay (west and north-west) (Paradis et al. 2016) and our measuring sites are thus mostly downwind from the village and the waste burning site (Figure 4.2). After data analysis it seemed very likely that fumes from the waste burning in open-air could have reached our measuring sites and probably affected the acquired data when wind speeds were high enough.

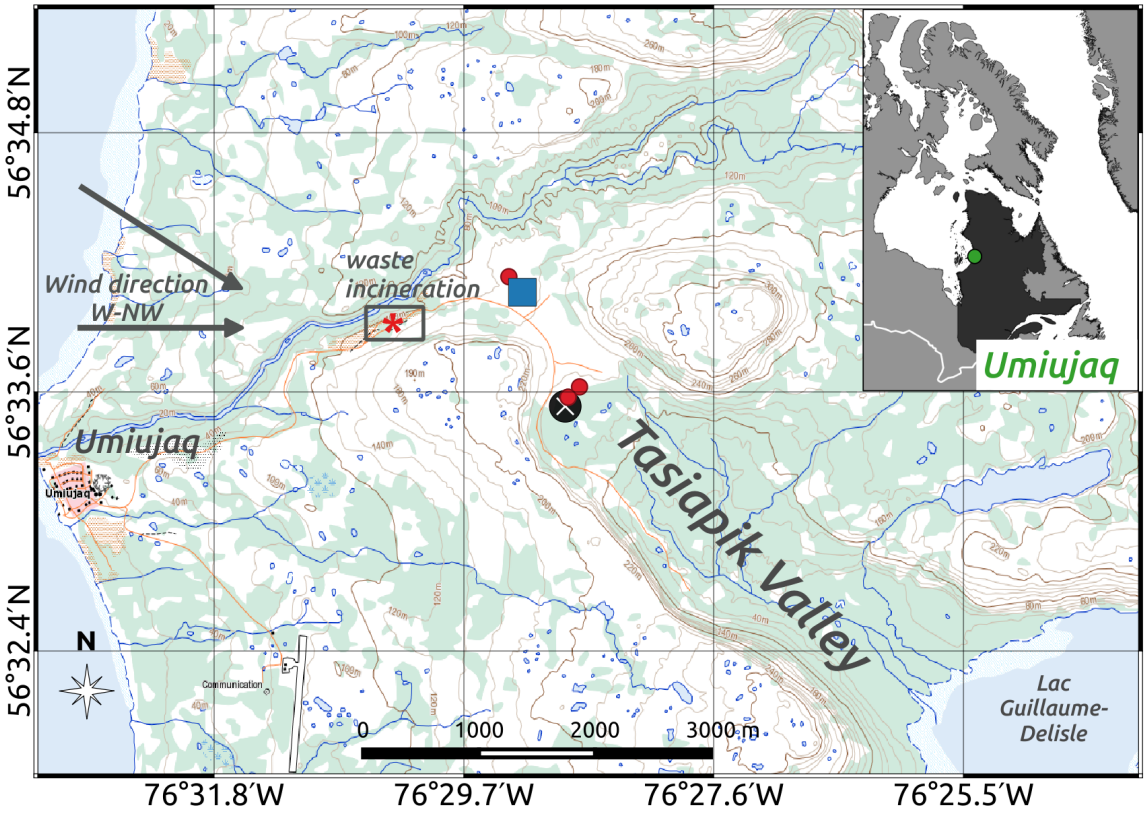

Figure 4.2. Map of the study area in the Tasiapik Valley near the village Umiujaq. The blue rectangle marks the area where SOLEXS profiles were measured in shrub-free snowpacks. The red dots mark where SOLEXS profiles were measured in snowpacks with shrubs. A white cross marks the position of the Automatic Weather Station (AWS) and the site where waste was burned is marked with a red star.

Data were acquired during a field campaign from 29 October to 6 December 2015. During that period, snow and irradiance measurements were taken in four snowpacks with shrubs and three shrub-free snowpacks. Measurements in snowpacks with shrubs were conducted on 3, 9, 14 and 23 November. Snow height at these sites varied between 43 and 63 cm and shrub height varied between 60 and 100 cm (Table 4.1). Measurements in shrub-free snowpacks were conducted on 8, 22 and 28 November, and snow height at these sites varied between 18 and 30 cm (Table 4.1). We aimed to conduct measurements for shrub and shrub-free snowpacks at weekly intervals, but harsh measuring conditions and frequent blizzards often prevented us from maintaining this regular measuring interval.

Table 4.1. Average snow height and shrub height in Umiujaq for the three shrub-free snowpacks and the four snowpacks with shrubs.

Site	Date	Shrub height, cm	Snow height, cm	Protruding branches, cm
Snow only	08 Nov 2015	-	18	-
	22 Nov 2015	-	23	-
	28 Nov 2015	-	30	-
Shrubs	03 Nov 2015	60	43	17
	09 Nov 2015	100	58	42
	14 Nov 2015	80	65	15
	23 Nov 2015	60	50	10

4.4.2.2 Data acquisition

Spectral irradiance profiles

Vertical irradiance in the snowpack was measured with the SOLar EXtinction in Snow profiler (SOLEXS). The instrument was developed and tested by Libois et al. (2014) and Picard et al. (2016), where a full description and schematic illustrations can be found. Basically, the SOLEXS instrument consists of an optical fiber cable which is inserted into a metallic rod painted in white (color: RAL 9003). The rod (10 mm diameter) is vertically inserted in the snowpack into a hole of the same diameter which was punched by a metal rod prior to the measurement. Throughout the continuous manual descent and subsequent rise of the rod in the hole, its position is registered with a depth sensor with a resolution of 1 mm. The optical cable is connected to an Ocean Optics MayaPro spectrometer with a spectral range of 300 to 1100 nm and a resolution of 3 nm. Here, we use measurements from 350 to 900 nm only because the signal-to-noise ratio is too low outside this range. Spectral radiation is recorded every 5 mm while the rod is continuously moving down and up the hole. The maximum acquisition depth is ~40 cm. Below 40 cm the signal-to-noise ratio becomes too low because of the reduced light intensity, and the shadow of the operator

cannot be neglected past this point (Libois et al. 2014), as detailed in Picard et al. (2016). The acquisition of one irradiance profile took around 2 minutes once the instrument was deployed. A photosensor was placed at the snow surface to monitor the incident radiation changes during the acquisition. If changes in incident radiation exceeded 3 %, the measurement was discarded. Measurements were conducted during any lighting conditions, i.e. overcast, partially overcast and sunny.

SOLEXS is accompanied by a post-processing library (Picard et al. 2016). This library automatically deploys the following processing to the recorded profiles: 1) subtraction of the dark current, 2) a depth correction using the small difference of timestamps between the depth and spectrum acquisitions, and 3) normalization by the photosensor current to correct for the small fluctuation of irradiance during the complete acquisition.

Snowpit data

After each acquisition of a SOLEXS profile, we dug a snowpit at the same spot. In the snowpit, the snow stratigraphy was recorded and photographed, vertical profiles of snow density and snow specific surface area (*SSA*) were measured, and, in snowpacks with shrubs, the presence of branches was noted. Snow density profiles have a resolution of 3 cm and were measured with a 100 cm^3 box cutter (Domine et al. 2016). *SSA* is the surface area of the snow-air interface per mass unit and is inversely related to the optical grain diameter of snow (Warren 1982, Domine et al. 2007). *SSA* was acquired with the DUFISS instrument detailed in Gallet et al. (2009). Briefly, DUFISSS measures the infrared reflectance of snow samples at 1310 nm by using an integrating sphere. *SSA* is then calculated from that reflectance with a simple algorithm (Gallet et al. 2009). *SSA* profiles were measured with a resolution of 1 to 3 cm.

Knowing snow density and *SSA* allows calculating the light absorption efficiency of snow by using radiative transfer theory (Kokhanovsky and Zege 2004, Picard et al. 2016). For these calculations, density and *SSA* need to be available with the same depth resolution. Where this was not the case in our data set, we performed linear interpolation between measured density data points, in order to synchronize the *SSA* and density profiles.

4.4.3 Methodology

4.4.3.1 Overview of methods

SOLEXS records the irradiance intensity at different depths (*I(z)*) and thus shows how much light is transmitted through the snowpack. The intensity of transmitted light decreases with depth either because radiation gets absorbed or because it is scattered which provokes a change in the light path direction. The processes of scattering and absorption together are called extinction. In a pure snowpack, extinction is mainly due to scattering. In contrast, impurities in the snowpack as well as buried branches cause light to become extinct mainly through absorption. Hence, when referring to light-impurity or light-branch interactions, for all practical purposes extinction and absorption can be used synonymously. In this study we are interested in comparing the extinction of light with depth in snowpacks with and without shrubs. This extinction is visualized as log-irradiance profiles ($I_{log}(z, \lambda)$):

$$I_{\log}(z,\lambda) = \log\left(I_0(\lambda) / I(z,\lambda)\right), \tag{4.1}$$

where I_0 is the incoming radiation at the surface, z is snow depth, λ is wavelength, and ($I(z, \lambda)$) are the measured SOLEXS profiles. Hence, to obtain $I_{log}(z, \lambda)$ from the measured data, SOLEXS profiles were normalized with $I_0(\lambda)$ and then presented in log scale. Here, the surface irradiance values for normalization are obtained at a depth of 3 cm (z = -3), because the presence of direct light may influence measurements at shallower depths.

Snowpacks are heterogeneous media made up of several kinds of light-extinctive materials – i.e. snow, light-absorbing particles (LAP) and, for snowpacks with shrubs, buried branches. During SOLEXS acquisitions, the measuring rod inserted into the snowpack also contributes to light extinction (Picard et al. 2016). If the interaction between the different light-extinctive materials is negligible, the log-irradiance profile in the medium $I_{log}(z, \lambda)$ is the sum of the material-specific terms. In snowpacks with shrubs this is calculated as:

$$I_{\log}(z,\lambda) = E_{snow}(z,\lambda) + E_{rod}(z,\lambda) + E_{LAP}(z,\lambda) + E_{shrub}(z,\lambda), \tag{4.2}$$

where E_{snow}, E_{LAP}, E_{shrub} and E_{rod}, represent the material-specific extinction of snow, impurities, shrubs and the measuring rod, respectively. In order to evaluate the extinction due to buried branches E_{shrub} from measured I_{log} profiles, E_{snow}, E_{rod} and E_{LAP}, need to be

calculated or estimated.

The approach presented here is a simplification, and more physically based approaches can be imagined where the influence of branches would be calculated with sophisticated 3-D radiative transfer models. Such an approach would require to perform complex simulations and to precisely characterize the optical and physical properties of our medium (i.e. the snowpack with branches and impurities). However, at this stage, very little is known about the influence of branches on radiative transfer in snow. We therefore gave precedence to this simpler and more straightforward approach to obtain first insights into the buried branches-snow-light interactions.

To determine the amount of light absorption by branches, we applied three successive steps. (i) First, light extinction by snow and the measuring rod (E_{snow} + E_{rod}) was calculated with a radiative transfer model as a function of *in situ* measured snow physical properties (Sect. 3.2). (ii) Next, the light absorption of impurities (E_{LAP}) was estimated using two complementary methods that allow retrieving impurity information from the irradiance profiles measured in shrub-free snowpacks (Sect. 3.3). (iii) Finally, based on the information acquired on E_{snow}, E_{rod}, and E_{LAP} in the two previous steps, we determined the influence of buried branches in the irradiance profiles measured in snowpacks with shrubs using Eq. (4.2).

4.4.3.2 Calculation of light extinction by snow and the measuring rod

The 3-D radiative transfer model SnowMCML was used to compute the combined light extinction of snow and the measuring rod (E_{snow} + E_{rod}). SnowMCML was developed by Picard et al. (2016) and is based on the model “Monte Carlo modeling of light transport in multi-layered tissues” (MCML) from Wang et al. (1995). Specifically, Picard et al. (2016) adapted the model to compute the signal recorded at the tip of a rod inserted in a multi-layered snowpack. The snow physical properties of each snow layer are supposed to be known, as well as the absorption of the rod. A detailed description of the model is given in Picard et al. (2016). Briefly, the model traces N light rays through a multi-layered snowpack with known physical properties. At each calculation step, light absorption and scattering is determined and the associated decrease in intensity for each light ray is

calculated. To optimize calculation time, the model uses the inverse principle in optics, launching rays from the collectors tip and tracing them back to the source at the surface instead of launching rays at the surface. Using this inverse mode allows to calculate only the path of those rays that hit the collector and which are thus relevant to compute the signal recorded at the tip of the rod. The size and optical properties of the rod need to be known to implement its effect in the simulations. Following the indications from Picard et al. (2016), the rod was modeled as a cylinder with a 10 mm diameter and a length corresponding to the insertion depth of the rod. The albedo of the rod (ω_{rod}) was set to 0.9 based on the reflectance measurements of the paint conducted by Picard et al. (2016), and it was assumed that the rod had Lambertian scattering characteristics, i.e. rays hitting the rod are scattered in a random direction. In the simulations, the rays hitting the rod were absorbed with a probability 1-ω_{rod}.

In addition to the size and optical properties of the rod, input data to SnowMCML were the physical properties of snow measured in the snowpits. The model outputs were theoretical transmittance profiles. These profiles show light transmittance for a snowpack without LAPs and branches, but with the same physical properties (*SSA* and density) as the snowpacks investigated. The simulated $I(z, \lambda)$ profiles were normalized and converted to log scale to obtain the log-irradiance profiles ($I_{log}(z, \lambda)$) from Eq. (4.1). These profiles were then compared with the log-irradiance profiles acquired in the field.

At transition zones, the performance of the model was found to be limited. These zones include the snow-atmosphere transition in the uppermost layer, the transition between two stratigraphic layers inside the snowpack, or the transition from snow to the underlying soil layer at the bottom of the snowpack. Discrepancies at the snow-atmosphere transition are probably caused by the rod entering the snowpack and causing an optical disturbance. Moreover, close to the surface and down to -7 cm, direct light can potentially penetrate the snowpack and come in through holes around the measuring rod as detailed by Picard et al. 2016. Since the presence of direct light is known to perturb the measured irradiance profiles (Picard et al. 2016, Tuzet et al. 2019), we discarded the first 7 cm in measured and simulated log-irradiance profiles. At stratigraphic transitions inside the snowpack, a mismatch between the model and the measured log-irradiance can be due to uncertainties in

the snow physical properties that are used as input to the model. These arise because snow physical properties often change gradually or are heterogeneous in stratigraphic transition zones. These fine-scale changes are not captured by our measuring profiles with a resolution of 1 to 3 cm, leading in turn to inaccuracies in the simulations compared to processes in the natural snowpack. Moreover, rod-light interactions that are calculated in the model also depend on snow physical properties, which can further amplify the discrepancies between the simulated and measured irradiance profiles.

An additional particularity at stratigraphic transition zones is the occasional occurrence of positive irradiance gradients (Picard et al. 2016). These are caused by different interactions between the rod and radiation in each snow layer near the layer transition. These interactions are complex and are explained in detail by Picard et al. (2016). Intuitively, when the rod reaches a lower layer, the magnitude of its artefact is determined by interactions between the rod and the layer above and in some cases this can result in an increase in the measured signal, even though the radiative transfer in a 1D layered-media excludes positive irradiance gradients. Although SnowMCML accounts for the rod artefact at transition zones and can calculate associated positive gradients, their occurrence in simulated and measured profiles may not concur if there are uncertainties in the snow physical properties that are used as input to the model. For this reason, we excluded transition zones, i.e. the top and bottom of each layer, from the interpretation of SnowMCML simulations.

4.4.3.3 Estimation of absorption by LAPs

Determining the specific absorption of LAPs (E_{LAP}) with radiative transfer models requires that concentrations of LAP be given, and that the optical properties for a given impurity type be known. Unfortunately, there are no data on LAPs for the snowpack near Umiujaq. Therefore, we assumed that LAPs are either mineral dust coming from a local source (hereafter called dust) or black carbon (BC). Dust can be transported from the cliffs and the barren rock surfaces at the top of cuestas to the valley during windy autumn storms which are typical for this region (Barrere et al. 2018, Paradis et al. 2016). BC is typically introduced to Arctic snow through long-range transport from fossil fuel combustion in the south (McConnell et al. 2007, Doherty et al. 2010). Based on field observations it seems

likely that BC was also produced by snowmobile traffic in the valley and, perhaps more importantly, by the waste burning occurring ~2 km upwind from our study site (Figure 4.2). Based on these assumptions, we employed two methods to estimate the relative concentration of BC and mineral dust.

The first method applies a regression approach to *in situ* data while the second uses SnowMCML to simulate radiative transfer in a snowpack with impurities. Both methods are similar in that they determine impurity type and concentration. The advantage of the SnowMCML method is that the model considers the influence of the measuring rod, but the disadvantage is that it assumes homogeneous impurity concentrations for the entire snowpack. In contrast, the regression method neglects the impact of the measuring rod but allows determining LAP concentrations for different layers individually. We applied the two complementary methods to validate results from each other. Finally, both methods were verified against log-irradiance measured in shrub-free snowpacks, where LAPs were the only unknown light-absorbing material. The two methods are detailed in the following sections.

4.4.3.3.1 Regression analysis of experimental profiles

In the first approach, information on LAP concentrations is derived from the irradiance profiles $I(z, \lambda)$ measured with SOLEXS by analyzing the rate of decrease of light intensity with snow depth following Tuzet et al. (2019). In snow layers with optically homogeneous conditions, light intensity decreases exponentially (Beer–Lambert Law). After a logarithmic transformation this exponential decrease becomes linear and the rate of decrease for a specific snowlayer is obtained from the slope of a linear regression (Figure 4.3a). In the literature, this rate of decrease is commonly referred to as the Asymptotic Flux Extinction Coefficient (e.g. Libois et al. 2013), but for the sake of simplicity we will refer to it as the extinction coefficient, k_e. The rate by which light decreases in the snowpack is wavelength-dependent and k_e is thus usually shown as a spectral curve termed $k_e(\lambda)$ (Figure 4.3b). k_e also depends on the physical properties of the snowpack (*SSA* and density ρ), and on the type and concentrations of LAPs mixed in the snowpack. For example, the $k_e(\lambda)$ curve for a dirty snowpack would display higher k_e values than a clean snowpack because the former is a much more absorbing medium and thus absorbs light at a greater rate. Consequently, each

snowpack layer has a specific spectral curve $k_e(\lambda)$ which is a function of the physical properties of the layer as well as the type and concentration of the LAPs mixed in the snowpack. This relation is mathematically expressed as (Libois et al. 2013, Tuzet et al. 2019):

$$k_e(\lambda) = \sqrt{\frac{3(1-g)}{2}\rho^2 SSA\left(\frac{B\gamma_{ice}(\lambda)}{\rho_{ice}} + MAE(\lambda)c\right)}, \quad (4.3)$$

where γ_{ice} is the ice absorption index which was set to the most recent estimate from Picard et al. (2016). B is the ice absorption enhancement factor and g the scattering asymmetry factor, which were set to default values of 1.6 and 0.85, respectively (Libois et al. 2014). ρ_{ice} is the density of ice (917 kg m^{-3}), and finally, c is the LAP concentration in kg kg^{-1} and MAE is the mass absorption efficiency (m^2 kg^{-1}) describing the optical property of a given LAP type (Caponi et al. 2017). For this study, the impurity type and the associated MAE values were either set to dust or BC. To determine LAP concentrations in the Umiujaq snowpack, the $k_e(\lambda)$ curve deduced from SOLEXS measurements (Figure 4.3) ($k_{e\_meas}(\lambda)$) was fitted to the $k_e(\lambda)$ curve calculated with Eq. (4.3) ($k_{e\_calc}(\lambda)$). To fit both curves, the LAP concentration (c in Eq. (4.3)) was estimated using Python's scipy.optimize.least_squares function which minimizes the mean square error between $k_{e\_calc}(\lambda)$ and $k_{e\_meas}(\lambda)$. The final best fit between the $k_{e\_calc}(\lambda)$ and $k_{e\_meas}(\lambda)$ curves in the spectral range considered (350–900 nm) was evaluated with the coefficient of determination (R^2) and the error was given by the root mean square error (RMSE). Determination of $k_{e\_meas}(\lambda)$ curves was restricted to layers where the optical properties in the snowpack were homogeneous for at least 3 consecutive centimeters, and the recorded SOLEXS signal was visually linear, because deducing a slope via linear regression is only possible under these conditions. These layers are hereafter called zones of interest (ZOI). According to Tuzet et al. (2019), ZOIs have to be at least 3 cm thick and lie at a snow depth >7 cm to accurately determine $k_{e\_meas}(\lambda)$. These restrictions are necessary to avoid biases from the SOLEXS measuring rod at shallow depths and around transition zones (discussed in Sect. 3.1; Picard et al. 2016). $k_{e\_meas}(\lambda)$ curves were smoothed using a first order Butterworth filter with the scipy.signal.butter function in Python (cutoff frequency set to 0.05; Figure 4.3b).

The spectrum used to fit $k_{e\_meas}(\lambda)$ and $k_{e\_calc}(\lambda)$ ranged from 400 to 450 nm. In this range absorption by ice is lowest, and impurities have the strongest impact on absorption profiles. Constraining the fit to a specific range instead of using the entire spectrum (350–900 nm) allows testing the hypothesis that BC or dust are the principal impurity types. A good fit between 400–450 nm should also return a good fit at wavelengths >450 nm if the spectral absorption of the absorbers were chosen correctly.

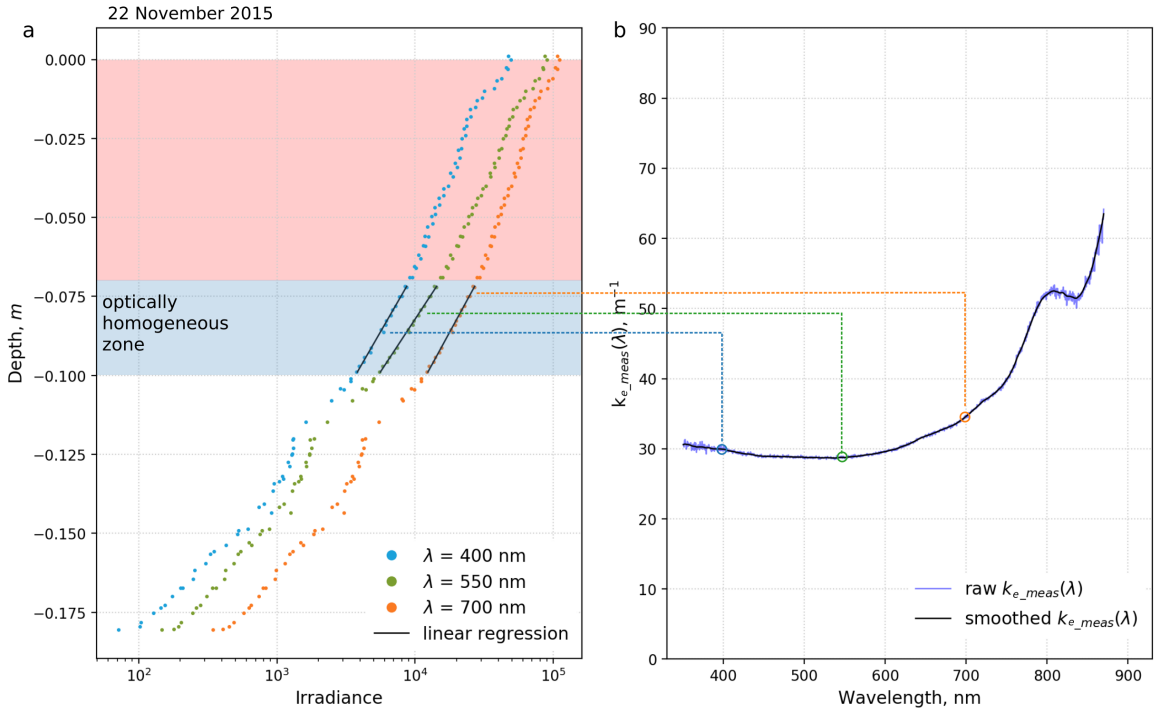

Figure 4.3. Overview of how the extinction coefficient ($k_{e\_meas}(\lambda)$) is determined from optically homogeneous layers in irradianceirradiance profiles. (a) Iirradiancerradiance as a function of depth for selected wavelengths. The blue shaded area highlights an optically homogeneous zone where the recorded signal is linear on logarithmic scale. The red shaded area was discarded due to potential influence of direct light. $k_{e\_meas}(\lambda)$ is the slope of irradiance vs. depth in the optically homogeneous zone obtained via linear regression (black lines). (b) $k_{e\_meas}(\lambda)$ determined for each wavelength in the measured spectrum (350–900 nm) before (blue curve) and after smoothing (black curve). The figure layout was adopted from Tuzet et al. (2019) and modified using data from Umiujaq. The presented data was measured in Umiujaq on 22 November 2015.

4.4.3.3.1 Snow MCML simulations

SnowMCML allows to simulate the effect of light-absorbing impurities for snowpacks with given LAP concentrations and MAE values for a given LAP type. For dust, the MAE was taken from Caponi et al., (2017) choosing Algerian dust type, with a grain diameter of 10

μm. Algerian dust was chosen because its optical properties (in particular its absorption Ångstrom exponent) are similar to that of the typical dust reported for snow in the Canadian sub-Arctic (2.5 for Algerian dust vs. 2.2 for sub-Arctic impurities) (Doherty et al. 2010). The relatively large grain diameter of 10 μm (vs. 2 μm) was chosen because we assumed the dust source to be local. For BC, we followed the approach of Tuzet et al. (2019) and determined the MAE from the study of Bond and Bergstrom (2006) and Hadley and Kirchstetter (2012). SnowMCML simulations were then computed with a variety of BC and dust concentrations. Note that each simulation corresponds to one LAP concentration as SnowMCML simulated radiative transfer assuming homogeneous LAP concentrations in the entire snowpack. BC or dust concentrations were determined by fitting the simulations with known LAP concentrations to the measured log-irradiance profiles with unknown concentrations. The snow-atmosphere transition zone (0 to -7 cm) and the stratigraphic transition zones were excluded from the fit as explained above. From the remaining non-transition layers, LAP type and concentrations were deduced from simulations that most accurately represented the radiative effect in the snowpack in Umiujaq. These best-fitting simulations were determined from a visual comparison of the simulated and measured profiles in shrub-free snowpacks.

4.4.4 Results and discussion

4.4.4.1 Impurities in snow without shrubs

LAP type and concentrations were determined from log-irradiance profiles measured in shrub-free snowpacks on 8, 22 and 28 November. The two methods, i.e. the k_e analysis and the SnowMCML method, are complementary but they should ideally yield similar results for the deduced LAP type and concentration for the Umiujaq snowpack.

LAP type

To test the validity of our initial assumption that LAP was either dust or BC, we compared the fit between $k_{e\_meas}(\lambda)$ and $k_{e\_calc}(\lambda)$ in four zones (ZOI1 to ZOI4) where optical properties were homogeneous and allowed determining an extinction coefficient. Two of these four zones were in snowpits measured on 8 and 22 November, and the other two were in the snowpit of 28 November. We found that setting the LAP type to BC in Eq. (4.3) constantly

returned a very good fit between the estimated and measured k_e curves in all four zones. For example, in ZOI1 which was measured on 8 November, the achieved fit had a R^2 value of 0.98 and a RMSE=1.67 (Figure 4.4a) when LAP was set to BC. The fit was good for all wavelengths in the spectrum considered (350–900 nm), suggesting that the spectral absorption signature of BC is well suited to reproduce the extinction coefficients observed in the field data. In contrast, setting the LAP type to dust in Eq. (4.3) (Figure 4.4b) resulted in visibly poor fits between $k_{e\_meas}(\lambda)$ and $k_{e\_calc}(\lambda)$ curves (R^2=0.38; RMSE=9.13). The fit was poor for the entire spectrum, but the direction and magnitude of the mismatch was wavelength-dependent, suggesting that the spectral absorption signature of dust was ill-suited to reproduce the extinction coefficients observed in the field data. Finally, using both BC and dust in Eq. (4.3) returned results which were essentially the same as for the simulations with BC only, because dust concentrations were estimated to virtually 0, reinforcing the conclusion that LAPs in our study site is mostly composed of BC. These results were similar for the other ZOIs in the shrub-free snowpacks (ZOI2–4), except for ZOI3 where the BC+dust option returned a fit almost as good as BC only, but still with low dust concentration estimations. Results for all four ZOIs are listed in Table 4.2. We conclude from the k_e analysis that BC is the only significant absorber in snow without shrubs, and the absorption due to dust is negligible.

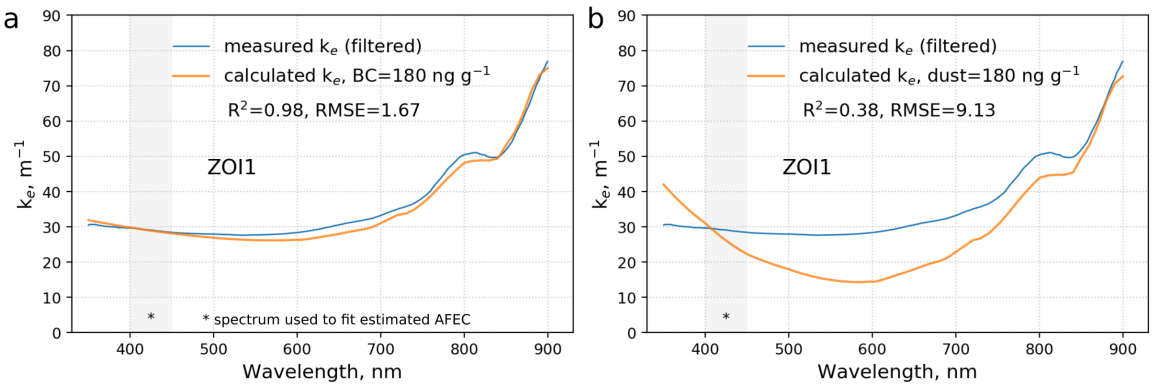

Figure 4.4. Example for measured and calculated absorption coefficient k_e for a snowpack without shrubs. Measured k_e was determined from SOLEXS measurements taken on 8 Nov. (ZOI1). Calculated k_e was computed with either (a) black carbon (BC) or (b) mineral dust as impurity type in the snowpack. The concentration of dust or BC was determined with an iterative approach, where calculated k_e was fitted to the measured k_e. This example shows how assuming BC as impurity type returns significantly better fits.

Table 4.2. Fit between measured and calculated extinction coefficient curves ($k_e(\lambda)$) for measurements in shrub-free snowpacks. Calculated $k_e(\lambda)$ was computed either with black carbon (BC), BC and mineral dust, or mineral dust only. The fit between measured and calculated $k_e(\lambda)$ was analyzed with the coefficient of determination (R^2), the error is indicated with the root mean square error (RMSE).

			BC only			BC+dust			dust only		
ZOI	Snow depth [m]	date	ng g^{-1}	R^2	RMSE	ng g^{-1}	R^2	RMSE	ng g^{-1}	R^2	RMSE
ZOI1	-0.7 – -0.1	8 Nov.	180	0.98	1.67	BC: 180 Dust: $1.1 * 10^{-25}$	0.98	1.67	11 664	0.38	9.13
ZOI2	-0.7 – -0.1	22 Nov.	185	0.96	2.59	BC: 184 Dust: $1.2 * 10^{-26}$	0.96	2.59	11 915	0.31	10.17
ZOI3	-0.7 – -0.1	28 Nov.	21	0.98	1.96	BC: 20 Dust: 42	0.98	1.98	1 359	0.96	2.84
ZOI4	-0.14 – -0.17	28 Nov.	7	0.91	2.02	BC: 7 Dust: $1.4 * 10^{-18}$	0.91	2.02	450	0.93	1.85

The results of the SnowMCML simulations concur with the results of the k_e analysis. Using BC as LAP returned better and wavelength-independent agreements between the simulated profiles and measured log-irradiance profiles. An example is shown in Figure D1 (Appendix D), demonstrating the fit between measured log-irradiance and SnowMCML profiles with either BC or dust at 400 and 500 nm. Therefore, from now on we will assume that BC is the dominant impurity type for the remainder of this study. This result is reasonable because BC has often been found to be the main impurity type in Arctic snow (e.g. Doherty et al. 2010, Wang et al. 2013). Moreover, the open-air waste burning near our study area was probably an important additional BC source (Figure 4.2). It might be that some trace amounts of dust, coming from the cuestas surrounding the Tasiapik valley, were also present in the snow, but their impact was too weak to be detected from our optical measurements. In order to identify all the different LAP constituents, it would be necessary to conduct a detailed chemical analysis of the snowpack but this was beyond the focus of this work.

LAP concentrations

BC concentrations were found to vary considerably among the shrub-free snowpacks. BC concentrations derived from the k_e analysis varied from 7 to 185 ng g^{-1} (Table 4.2). On 8 and 22 November, BC concentrations were high with 180 ng g^{-1} and 185 ng g^{-1}, respectively. On 28 November the snowpack was comparatively cleaner with only 7 and 21 ng g^{-1} BC in ZOI3 and ZOI4, respectively.

BC concentrations from SnowMCML simulations were determined from the ZOI layers also used in the k_e analysis (ZOI1–ZOI4, highlighted in blue in Figure 4.5), plus one additional layer (ZOI2_b, Figure 4.5), while the transition zones (T1–T3 in Figure 4.5) where excluded from our analysis. The additional layer ZOI2_b was only used for the SnowMCML analysis because its signal-to-noise ratio at longer wavelengths was too weak to establish a spectral $k_{e\_meas}(\lambda)$ curve. Note that in layers ZOI1 and ZOI2, simulations showed the same extinction gradient as the measured data but with an offset. Consequently, simulated and measured profiles were parallel to each other in ZOI1 and ZOI2 instead of being superposed. The reason for the offset was probably that the amount of light transmitted to ZOI1 and ZOI2 from the transition zone was inaccurately calculated by the model. In non-transition zones and after correcting the offset in ZOI1 and ZOI2, BC concentrations derived by fitting SnowMCML simulations to measured log-irradiance profiles concurred with the results from the k_e analysis. On 8 and 22 November, SnowMCML simulations with 185 ng g^{-1} fitted best with the observed absorption gradients, while on 28 November the snowpack was cleaner and the best fit was achieved with a simulation without BC.

By excluding transition zones and after correcting the offset where necessary, we obtain concordant results with both independent methods. We are thus confident in the BC concentrations reported here. The observation that BC concentrations have high spatiotemporal variability also fits with our previous interpretation that an important source of BC in Umiujaq snow was most likely the nearby irregular waste burning. Waste was not burned continuously and the specific spatial deposition of BC would strongly depend on wind speed and direction during burning events. The snowpacks sampled on 8 and 22 November both had high BC concentrations and the analysed layers were probably

accumulated during burning events. Accumulation could either have happened through direct precipitation or when a previously clean precipitated layer was drifted by wind through polluted air masses and then redeposited in wind-sheltered depressions. In contrast, the clean snowpack on 28 November was probably accumulated during a waste-burning break. The spatiotemporal variability in BC concentrations is thus probably the result of discontinuous waste burning and the heterogeneous snow accumulation and erosion patterns due to wind drifting.

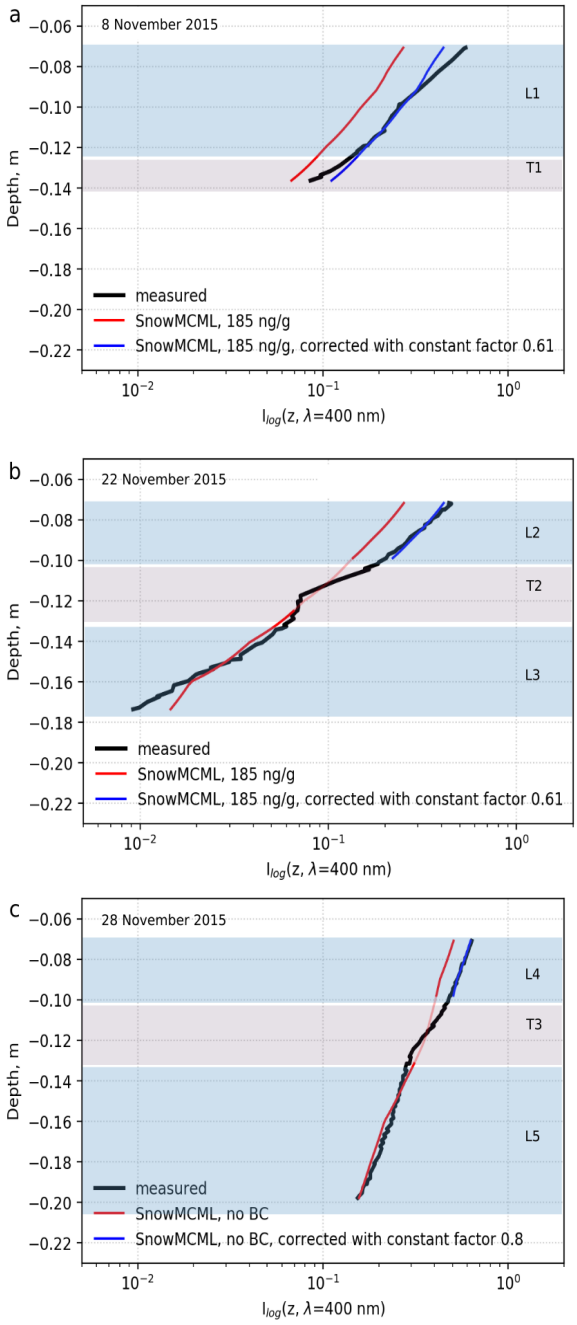

Figure 4.5. Measured log-irradiance profiles (black curves) and MCML simulations (red and blue curves) for snowpacks without shrubs at 400 nm. Simulated profiles were computed assuming black carbon (BC) as impurity type. Log-irradiance profiles were measured on (a) 8 Nov., (b) 22 Nov. and (c) 28 Nov. Gray shaded areas highlight transition zones, where simulated and measured profiles were not expected to fit. Blue shaded areas highlight non-transition zones were the fit between simulated and measured profiles allowed the determination of impurity concentrations.

4.4.4.2 Insights in the radiative effect of buried branches

Determining the effect of buried branches from the acquired log-irradiance profiles proved a complex task because high BC concentrations had a strong impact on absorption, potentially masking the effect of branches. Furthermore, we could not deduce a constant impurity concentration representative of the Umiujaq snowpack in general. Consequently, in Eq. (4.2), $E_{LAP}(z)$ and $E_{shrub}(z)$ both remain unknown variables in the log-irradiance profiles measured in snowpacks with shrubs. Nevertheless, interesting insights on how buried branches might influence light propagation were gained by (i) comparing SnowMCML simulations with the measured log-irradiance profiles and (ii) studying the spectral shape of $k_{e\_meas}(\lambda)$ and $k_{e\_calc}(\lambda)$ for different layers in snowpacks with branches.

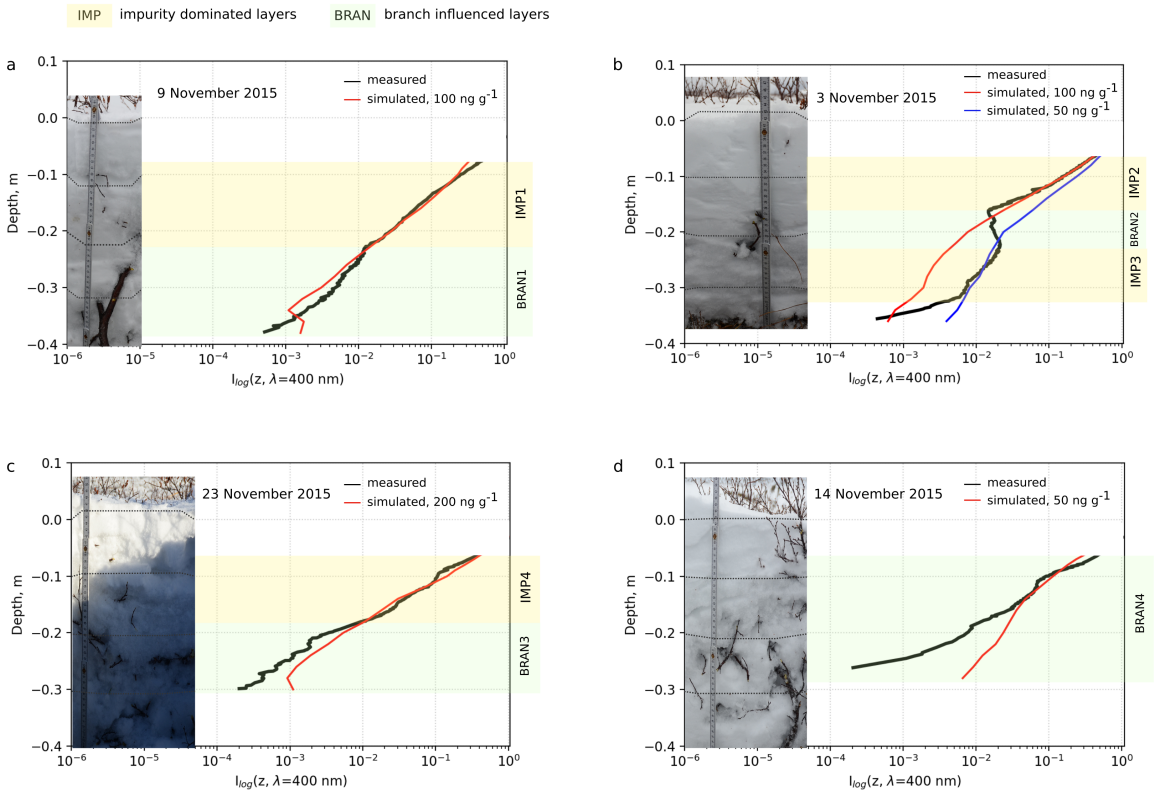

Figure 4.6. Log-irradiance profiles and MCML simulations at 400 nm for measurements taken on (a) 9 Nov., (b) 3 Nov., (c) 23 Nov., and (d) 14 Nov. in snowpacks with shrubs. Yellow shaded areas highlight layers where measured log-irradiance profiles and MCML simulations fitted well. Green shaded areas highlight layers where log-irradiance and MCML simulations fit less well and branches were visible in the snowpit photographs.

From the comparison of measured log-irradiance profiles with SnowMCML simulations at 400 nm, we found that snowpacks in shrubby areas consisted of two types of optically distinct layers (Figure 4.6). Characteristics of the first layer type were that the measured profiles fitted well with the SnowMCML simulations (called layers IMP1 through IMP4 in Figure 4.6), although the simulations only considered the extinction of light by snow, the measuring rod and BC, but not by shrubs. Moreover, photographs of the snowpits showed no or very few branches in these layers. The best examples for this layer type are IMP1 and IMP2, where the measured log-irradiance fitted very well with simulated SnowMCML profiles at BC=100 ng g^{-1} (Figure 4.6a and b). The measured log-irradiance profiles in IMP1 and IMP2 decrease linearly, indicating a constant extinction coefficient. These layers thus seem to have homogeneous optical properties and to be free of optical disturbances like branches. In IMP3 and IMP4 the measured log-irradiance profile was less regular, showing numerous small disturbances in the extinction coefficient. Nevertheless, the general trend in IMP3 fitted well to simulations with BC concentrations of 50 ng g^{-1} and IMP4 to simulations with 200 ng g^{-1}. Therefore, it is reasonable to suggest that light absorption in the IMP layers was mostly dominated by BC concentrations and that the influence of branches was negligible.

For the second layer type (BRAN1 through BRAN4, Figure 4.6), we found several lines of evidence that branches influenced light absorption in snow. First, unlike in the IMP layers, the log-irradiance profiles did not fit the SnowMCML simulations well. Secondly, the log-irradiance profile was very irregular in comparison with IMP1 or IMP2, showing a highly variable extinction coefficient. Finally, comparing the BRAN layers to the snowpit photographs revealed striking correspondences between these layers and the presence of branches. In Figure 4.6a, a branch appeared at 22 cm depth, where the simulated and measured profiles start to diverge (BRAN1). Note that between snow depths 34 and 37 cm in BRAN1 the simulated profile shows a positive irradiance gradient which is not visible in the measured signal. As explained in Sect. 3.2 positive gradients can happen at transition zones and are an artefact caused by the rod. The discrepancy between the measured and modeled profile arises most likely due to uncertainties in the measured snow physical properties input to the model. In Figure 4.6b, two small twigs appeared between snow depths 16 to 24 cm, which coincided with a part of the log-irradiance profile that poorly fits

the simulations (BRAN2). In this layer the measured profile shows a positive gradient but not the simulated profile. This discrepancy may again be caused by uncertainties in the snow physical properties, but it is more likely that here it is the result of the optical disturbance caused by branches. Branches absorb light locally thus reducing the irradiance signal, but once the sensor exits the shadow of the branch light may hit it from the side resulting in an increase in measured irradiance and thus an enhancement of the positive gradient. In Figure 4.6c, the snowpit had generally more branches than the snowpits in Figure 4.6a and 6b. Branches became particularly abundant between 10 and 40 cm depth, as also documented in our field notes. This was also where the simulation started to diverge more significantly from the measured profile (BRAN3). A high variability of the extinction coefficient, which was already observed in IMP4, was also visible in the irregular log-irradiance profile in BRAN3. Finally, in Figure 4.6d, branches were abundant in the entire snowpit and the measured profile could not be properly fitted to any of the simulations (BRAN4). BRAN 4 also showed a highly variable extinction coefficient similar to the log-irradiance profile in Figure 4.6c.

To further confirm the finding that shrubby snowpacks consist of impurity-dominated and branch-influenced layers, the spectral information from the k_e analysis was exploited. We determined the $k_{e\_meas}(\lambda)$ and $k_{e\_calc}(\lambda)$ curves for IMP1, IMP2 and IMP3 as well as for BRAN1 and BRAN4. With this k_e analysis we aimed to test whether light extinction in IMP layers was indeed dominated by BC concentrations. Furthermore, we aimed to verify that any influence of branches was visible in BRAN1 and BRAN4. Note that k_e curves were not determined for BRAN2, because k_e values were negative due to the observed positive extinction gradient, or for BRAN3 because the signal-to-noise ratio was too low. The results of the k_e analysis are shown in Figure 4.7b. For comparison, we also show k_e curves for the ZOIs 1-3 in shrub-free snowpacks (Figure 4.7a). For IMP2, $k_{e\_meas}(\lambda)$ and $k_{e\_calc}(\lambda)$ fitted very well (R^2=0.97) in the 350–830 nm spectral range and returned BC concentrations of 92 ng g^{-1} which concurs with the results from the SnowMCML simulations (BC=100 ng g^{-1}). We conclude that for IMP2, absorption properties of BC were indeed well suited to reproduce the observed spectral extinction and that the assumption that BC is the dominant absorber is likely. For IMP1 the fit was reasonably good (R^2=0.74) and estimated BC concentrations (95 ng g^{-1}) concurred with SnowMCML results (BC=100

ng g^{-1}), but the $k_{e\_meas}(\lambda)$ curve showed a significant drop at wavelengths >780 nm which does not appear in the theoretical $k_{e\_calc}(\lambda)$ curve. For IMP3, BRAN1 and BRAN4 we also observe that the $k_{e\_meas}(\lambda)$ and $k_{e\_calc}(\lambda)$ curves diverge because values in the $k_{e\_meas}(\lambda)$ curves drop at longer wavelengths. For IMP3, BRAN1 and BRAN4 the fit between $k_{e\_meas}(\lambda)$ and $k_{e\_calc}(\lambda)$ was also generally lower with R^2 of -4.65 (IMP3), -9.32 (BRAN1) and 0.62 (BRAN4). Note that obtaining negative R^2 values is possible because we constrained the fit of $k_{e\_meas}(\lambda)$ and $k_{e\_calc}(\lambda)$ to the range 400–450 nm while the evaluation was performed for a much larger range. In such a constrained setting, calculated values can fit the observed values less well than a horizontal line (= the null hypothesis) which results in R^2 values below 0. The interpretation of negative R^2 is that the calculated values fit the observations very poorly in at least part of the spectrum (Motulsky and Christopoulos 2003).

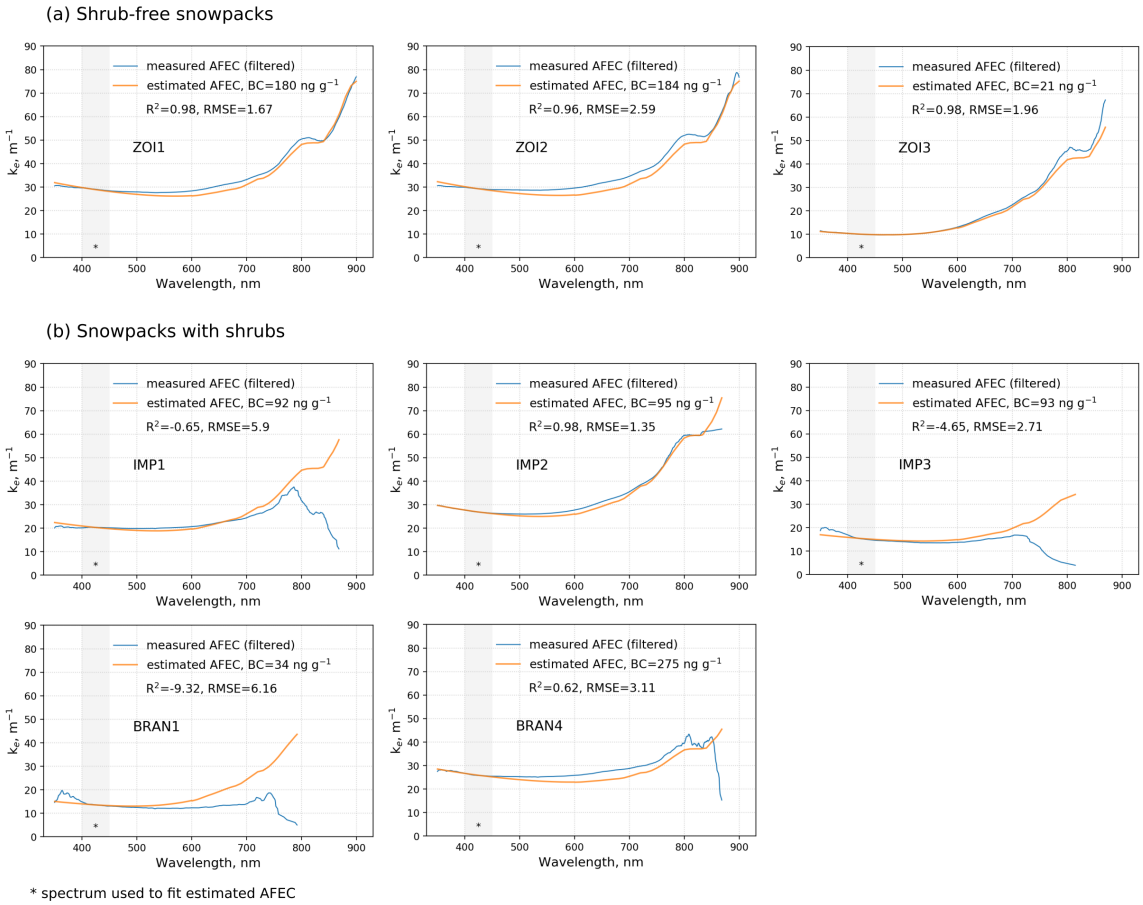

Figure 4.7. Measured and calculated k_e for (a) ZOIs in shrub-free snowpacks and (b) IMP and BRAN layers identified in shrub snowpacks (see also Figure 4.6). Gray areas highlight the spectral range where calculated k_e was fitted to measured k_e. Deviations at wavelengths >680 nm are interpreted as influence of buried branches.

We interpret the observed drop in the $k_{e\_meas}(\lambda)$ curves at >680 nm as a strong indicator of the influence of branches (Figure 4.7). Reflectivity measurements for Arctic shrub branches showed that branches are highly absorbing at 400–500 nm, but that reflectivity increases slightly at 500 nm and then even more sharply at 680 nm (Juszak et al. 2014) (Figure 4.1). We conclude that the optical properties of branches are well suited to explain the observed drop in extinction at 500–900 nm in the measured k_e curves (Figure 4.7). In contrast, $k_{e\_calc}(\lambda)$ curves were calculated assuming that all extinction other than by snow or the rod was due to BC. In this case, the $k_{e\_calc}(\lambda)$ curves overestimate extinction in the spectrum >500 nm because in this range BC is more absorbing than branches (Figure 4.1). It is likely that in IMP1 and IMP3 branches had an influence on the irradiance profile although the measured log-irradiance fitted well with the SnowMCML simulations and no branches were detected in the photographs. In BRAN1 to BRAN4 the effect of branches seemed to be stronger, as suggested by the multiple indicators for branch influence (for example irregular profiles or the mismatch between measured log-irradiance and SnowMCML simulations). In contrast, almost no influence of shrubs could be detected in IMP2 despite the layer being located in a snowpack with shrubs. This leads us to conclude that the optical effect of a buried branch must be highly localized and that its impact strongly weakens as a function of distance from the branch. The log-irradiance profiles here were measured at different distances to branches, but the exact distances are unknown to us, which is why the influence of branches varied in the different IMP and BRAN layers. This shows that quantifying the impact of branches would require to know the position of branches in the snowpack with precision.

An important consequence of increased absorption by shrubs is a local heating effect. This local heating assumption was mentioned in Sturm et al. (2005) and Pomeroy et al. (2006) and is further supported by cursory observations on snow physical properties made during the field campaign in this study. During a warm spell on 19 and 20 November 2015, we observed that snow melt rates were increased in the direct vicinity of branches, forming a snowpack filled with holes (Figure 4.8a and b). If shrub-induced radiative heating would have had a broader effect, the snowpack should melt more homogeneously than the observed swiss cheese snowpack. Localized melting around buried branches was also suggested by Sturm et al. (2005) and Pomeroy et al. (2006), which they considered to be an

important factor for shrub spring-up in spring. In addition to the melt holes, we also found large clusters of melt-freeze grains attached to branches (Figure 4.8c), indicating local melting. When conditions were cold enough to prevent melting, the local radiative heating effect of branches resulted in the formation of pockets of depth hoar (or faceted crystals) around branches (Figure 4.8d and e). Depth hoar are snow grains with a high metamorphic degree (Akitaya 1975) and are formed by high water vapor fluxes generated by strong temperature gradients in snowpacks. Strong vertical temperature gradients exist in the Arctic tundra in autumn, between the cold atmosphere and the relatively warmer soils. In the absence of shrubs, these temperature gradients typically form horizontal layers of depth hoar at the bottom of the Arctic snowpack. In the presence of shrubs, temperature gradients between the warmer branches and the colder snow nearby are increased, leading to enhanced depth hoar formation. As the effect of branches is very local, however, this causes metamorphism only in the direct vicinity of branches, explaining the formation of depth hoar pockets rather than layers. This effect is particularly important for branches near the surface due to the proximity with the cold atmosphere and the higher irradiance. However, when depth hoar starts forming, its low thermal conductivity increases thermal gradients and further favours depth hoar formation so that the process may persist near branches even once they are deeply buried (this is also discussed in Domine et al. 2016).

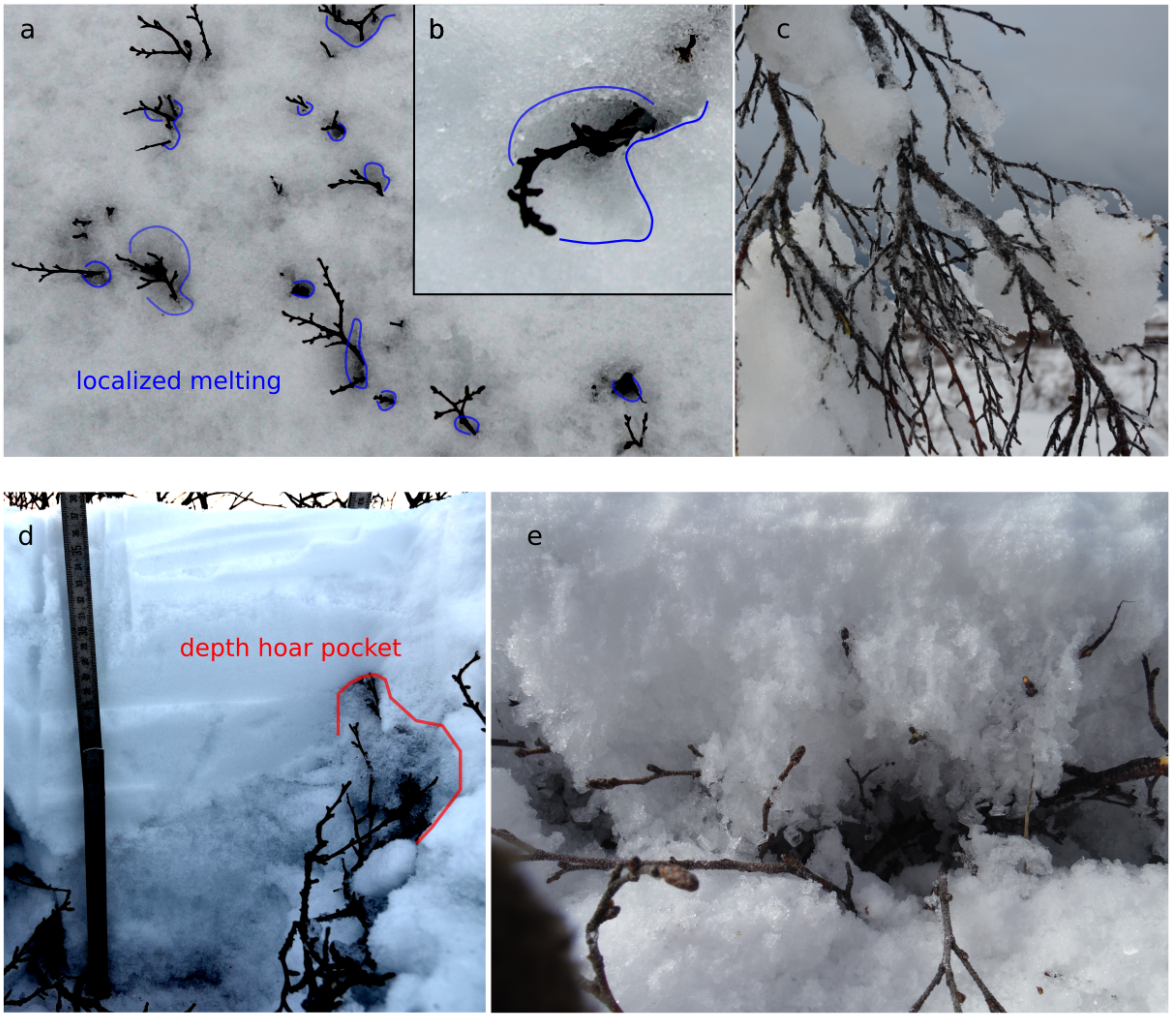

Figure 4.8. Photographs showing cursory observations of localized snow melting around branches (a, b, c) and the formation of depth hoar pockets around buried branches (d, e). Photographs were taken during the measuring campaign from 29 Oct. to 6 Dec. 2015. In (d) the contrast of the photograph was increased to make the depth hoar pockets more visible.

The modifications of snow physical properties induced by buried branches are important because they influence the insulating effect of snow. In particular, depth hoar layers have very good insulating properties (Domine et al. 2016), while melt-freeze layers are poor insulators (Barrere et al. 2018). The insulating properties of a snowpack are critical for the survival of Arctic flora and fauna in winter (Berteaux et al. 2017, Domine et al. 2018), and directly impact the thermal regime of permafrost, which has important implications for ongoing climate change (Koven et al. 2013, Schuur et al. 2015). Apart from these ecosystem-related consequences, shrub-induced modifications of snow physical properties

are also disturbing the layered structure of the snowpack which is important for radiative transfer models calculating light propagation through snow under the presumption that snowpacks are plane-parallel media. It may be important to factor in these branch-induced structural disturbances in future studies simulating snow radiative transfer in mixed snowpacks.

4.4.4.3 Source of high BC concentrations

The data presented here on shrub-free snowpacks were not intended to be an exhaustive study of impurities in snow in the Umiujaq region, as their primary objective was to serve as a comparison to the measurements in snowpacks with shrubs. It is nevertheless noteworthy that BC concentrations measured on 8 and 22 November were unexpectedly more than twice as high as the median values reported for the rest of the Arctic, where concentrations outside Greenland lie around 20 ng g^{-1}, with slightly higher values up to 60 ng g^{-1} in Arctic Russia and Scandinavia (Doherty et al. 2010). High values similar to those measured here usually occur in mid-latitudes, for example in Northern China (117–1220 ng g^{-1}) (Wang et al. 2013) or the Chilean Andes (up to 100 ng g^{-1}) (Rowe et al. 2019), where the proximity to cities and industrial activities produce more BC. The Arctic was usually found to be cleaner due to its distance to BC source regions (Skiles et al. 2016) and because BC concentrations have been continuously declining since industrial BC emissions in Europe and North America started decreasing in the early twentieth century (McConnell et al. 2007, Gong et al. 2010).

The high BC concentrations this study determined in Umiujaq could be either due to forest fires, which are common in the boreal forest areas in Quebec (Gauthier et al. 2015), or due to local anthropogenic sources. Forest fires occur mostly in summer, and we therefore think that it is unlikely that they can be the source for the observed high BC concentrations in early winter. Based on the field observations it seems more likely that high concentrations were due to local anthropogenic sources such as snowmobile traffic in the valley and, perhaps more importantly, the waste burning occurring ~2 km upwind from our study site (Figure 4.2). Such local anthropogenic sources in the Arctic may become more influential as northern communities keep growing, Arctic tourism keeps blooming and ship traffic keeps increasing. It is thus most likely that the contribution of BC emissions produced in

the North, amongst others by waste burning, will increase in the near future and decrease snow albedo which could possibly advance the melt season by a few weeks (Tuzet et al. 2020). However, more research is necessary to accurately quantify BC production in Umiujaq and in northern communities in general and to determine potential impacts. Nevertheless, our findings highlight that the anthropogenic footprint in the Arctic may be important and suggests that a cleaner waste management should be put in place for the protection of northern communities and the ecosystem.

4.4.5 Conclusion

This study presented the first measurements of irradiance profiles in snowpacks with shrubs, together with complementary irradiance measurements acquired in shrub-free snowpacks. Profiles measured in shrub-free snow were analysed to determine impurity type and impurity concentrations. For snow in Umiujaq, the main impurity, as inverted from a radiative transfer model, was black carbon (BC) which occurred in concentrations with large spatiotemporal variability. Some layers featured low concentrations (0–7 ng g^{-1}) while other layers had concentrations as high as 180–185 ng g^{-1}. High concentration layers were probably produced by the emission of nearby open-air waste burning. The high BC concentrations reported here may be one of the first indicators that cleaner waste manamagement plans are required to avoid the production of important BC concentrations from local sources in the Arctic. However, more research is required to draw firm conclusions over a longer period.

Irradiance profiles measured in snowpacks with shrubs showed that the impact of branches was weak and local. In some layers, light absorption depended primarily on BC concentrations and branches played only a minor role. In other layers, coinciding with where branches were visible in snowpit photographs, the branch effect was more prominent, suggesting the local-effect hypothesis. This assumption was further supported by cursory observations of localized melting and depth hoar pockets forming in the vicinity of branches in the snowpack. The local modification of snow physical properties by branches increases the heterogeneity of the snowpack and disturbs its plane-parallel structure. This heterogeneity should be considered by future research aiming to measure the radiative impact of shrubs *in situ* or simulate it with radiative transfer models.

References

Abbatt, J. P. D., W. R. Leaitch, A. A. Aliabadi, A. K. Bertram, J.-P. Blanchet, A. Boivin-Rioux, H. Bozem, et al. 2019. Overview Paper : New Insights into Aerosol and Climate in the Arctic." *Atmospheric Chemistry and Physics.* 19(4): 2527-2560. doi:10.5194/acp-19-2527-2019.

Akitaya, E. 1975. Studies on depth hoar. In Nye J., ed. Snow Mechanics (Proceedings of a symposium held at Grindelwald, April 1974) IAHS Pub. 114, 42–48

Aoki, T., T. Aoki, M. Fukabori, A. Hachikubo, Y. Tachibana, and F. Nishio. 2000. Effects of Snow Physical Prameters on Spectral Albedo and Bidirectional Reflectance of Snow Surface. *Journal of Geophysical Research* 105(D8): 10219-10236. doi:10.1029/1999JD901122.

Aoki, T., K. Kuchiki, M. Niwano, Y. Kodama, M. Hosaka, and T. Tanaka. 2011. Physically Based Snow Albedo Model for Calculating Broadband Albedos and the Solar Heating Profile in Snowpack for General Circulation Models. *Journal of Geophysical Research.* 116(D11): 1–22. doi:10.1029/2010JD015507.

Barrere, M., F. Domine, M. Belke-Brea, and D. Sarrazin. 2018. Snowmelt Events in Autumn Can Reduce or Cancel the Soil Warming Effect of Snow–Vegetation Interactions in the Arctic. *Journal of Climate.* 31(23): 9507–18. doi:10.1175/JCLI-D-18-0135.1.

Bartlett, P. A., M. D. Mackay, and D. L. Verseghy. 2006. Modified Snow Algorithms in the Canadian Land Surface Scheme: Model Runs and Sensitivity Analysis at Three Boreal Forest Stands. *Atmosphere-Ocean.* 44(3): 207–22. doi:10.3137/ao.440301.

Belke-Brea, M., F. Domine, M. Barrere, G. Picard, and L. Arnaud. 2019. Impact of Shrubs on Surface Albedo and Snow Specific Surface Area at a Low Arctic Site : In-Situ Measurements and Simulations. *Journal of Climate.* 33(2): 1–42. doi:10.1175/JCLI-D-19-0318.1.

Berteaux, D., G. Gauthier, F. Domine, R. A. Ims, S. F. Lamoureux, E. Lévesque, and N. Yoccoz. 2017. Effects of Changing Permafrost and Snow Conditions on Tundra Wildlife : Critical Places and Times. *Arctic Science.* 3(2): 65–90.

Bond, T. C., and R. W. Bergstrom. 2006. Light absorption by carbonaceous particles: An investigative review, Aerosol science and technology. 40(1) 27–67.

Bond, T. C., T. L. Anderson, and D. Campbell. 1999. Calibration and Intercomparison of Filter-Based Measurements of Visible Light Absorption. *Aerosol Science and Technology* 30(6): 582–600. doi:10.1080/027868299304435.

Bond, T. C., and R. W. Bergstrom. 2006.Light Absorption by Carbonaceous Particles: An Investigative Review. *Aerosol science and technology.* 40(1): 27-67.

Bond, T. C., D. G. Streets, K. F. Yarber, S. M. Nelson, J. Woo, and Z. Klimont. 2004. A

Technology-Based Global Inventory of Black and Organic Carbon Emissions from Combustion. *Journal of Geophysical Research* 109(D14): 1–43. doi:10.1029/2003JD003697.

Caponi, L., P. Formenti, D. Massabó, C. Di Biagio, M. Cazaunau, E. Pangui, S. Chevaillier, et al. 2017. Spectral- and Size-Resolved Mass Absorption Efficiency of Mineral Dust Aerosols in the Shortwave: A Simulation Chamber Study. *Atmospheric Chemistry and Physics.* 17(11): 7175–91. doi:10.5194/acp-2017-5.

Cess, R. D. 1983. Arctic Aerosols: Model Estimates of Interactive Influences upon the Surface-Atmosphere Clear-Sky Radiaiton Budget. *Atmospheric Environment.* 17(12): 2555–64.

Cooper, E. J., S. Dullinger, and P. Semenchuk. 2011. Late Snowmelt Delays Plant Development and Results in Lower Reproductive Success in the High Arctic. *Plant Science.* 180(1): 157–67. doi:10.1016/j.plantsci.2010.09.005.

Dal Farra, A., S. Kaspari, J. Beach, T. D. Bucheli, M. Schaepman, and M. Schwikowski. 2018. Spectral Signatures of Submicron Scale Light-Absorbing Impurities in Snow and Ice Using Hyperspectral Microscopy. *Journal of Glaciology.* 64(245): 377–86. doi:10.1017/jog.2018.29.

Dang, C., S. G. Warren, Q. Fu, S. Doherty, M. Sturm, and J. Su. 2017. Journal of Geophysical Research : Atmospheres. *Journal of Geophysical Research Atmospheres.* 122(10): 149–68. doi:10.1002/2017JD027070.

Diehl, T., A. Heil, M. Chin, X. Pan, D. Streets, M. Schultz, and S. Kinne. 2012. Anthropogenic, Biomass Burning, and Volcanic Emissions of Black Carbon, Organic Carbon, and SO_2 from 1980 to 2010 for Hindcast Model Experiments. *Atmospheric Chemistry and Physics Discussion.* 12(9): 24895–954. doi:10.5194/acpd-12-24895-2012.

Doherty, S. J., S. G. Warren, T. C. Grenfell, A. D. Clarke, and R. E. Brandt. 2010. Light-Absorbing Impurities in Arctic Snow. *Atmospheric Chemistry and Physics.* 10(23): 11647–80. doi:10.5194/acp-10-11647-2010.

Domine, F., M. Albert, T. Huthwelker, H. W. Jacobi, A. A. Kokhanovsky, M. Lehning, G. Picard, and W. R. Simpson. 2008. Snow Physics as Relevant to Snow Photochemistry. *Atmospheric Chemistry and Physics.* 8: 171–208.

Domine, F., M. Barrere, and S. Morin. 2016. The Growth of Shrubs on High Arctic Tundra at Bylot Island: Impact on Snow Physical Properties and Permafrost Thermal Regime. *Biogeosciences Discussions.* 13(23): 6471. doi:10.5194/bg-2016-3.

Domine, F., A. S. Taillandier, S. Houdier, F. Parrenin, W. R. Simpson, and T. A. Douglas. 2007. Interactions between Snow Metamorphism and Climate: Physical and Chemical Aspects. *Physics and Chemistry of Ice, [Proceedings of the International Conference on the Physics and Chemistry of Ice], 11th, Bremerhaven, Germany, July 23-28, 2006*, 27–46.

Domine, F., G. Gauthier, V. Vionnet, D. Fauteux, M. Dumont, and M. Barrere. 2018. Snow Physical Properties May Be a Significant Determinant of Lemming Population Dynamics in the High Arctic. *Arctic Science.* 4(4): 813–26. doi:dx.doi.org/10.1139/as-2018-0008.

Domine, F., J. Bock, S. Morin, G. Giraud. 2018. Linking the effective thermal conductivity of snow to its shear strength and density. *Journal of Geophysical Research: Earth Surface.* 116(F4): F04027. doi:10.1029/2011JF002000.

Flanner, M. G., and C. S. Zender. 2005. Snowpack Radiative Heating: Influence on Tibetan Plateau Climate. *Geophysical Research Letters.* 32(6): 1–5. doi:10.1029/2004GL022076.

Förster, K., J. Garvelmann, G. Meißl, and U. Strasser. 2018. Modelling Forest Snow Processes with a New Version of WaSiM. *Hydrological Sciences Journal.* 63(10): 1540–57. doi:10.1080/02626667.2018.1518626.

France, J. L., M. D. King, M. M. Frey, J. Erbland, G. Picard, S. Preunkert, A. MacArthur, and J. Savarino. 2011. Snow Optical Properties at Dome C (Concordia), Antarctica; Implications for Snow Emissions and Snow Chemistry of Reactive Nitrogen. *Atmospheric Chemistry and Physics.* 11(18): 9787–9801. doi:10.5194/acp-11-9787-2011.

Gagnon, M., F. Domine, and S. Boudreau. 2019. The Carbon Sink due to Shrub Growth on Arctic Tundra : A Case Study in a Carbon-Poor Soil in Eastern Canada. *Environmental Research Communications.* 1(9): 091001.

Gallet, J. C., F. Domine, C. S. Zender, and G. Picard. 2009. Measurement of the Specific Surface Area of Snow Using Infrared Reflectance in an Integrating Sphere at 1310 and 1550 Nm. *The Cryosphere.* 3(2): 167–82. doi:10.5194/tc-3-167-2009.

Gauthier S., P. Bernier, T. Kuuluvainen, A. Z. Shvidenko and D. G. Schepaschenko. 2015. Boreal forest health and global change. *Science. 349*(6250): 819-822. doi: 10.1126/science.aaa9092

Gong, S. L., T. L. Zhao, S. Sharma, D. Toom-Sauntry, D. Lavoué, X. B. Zhang, W. R. Leaitch, and L. A. Barrie. 2010. Identification of Trends and Interannual Variability of Sulfate and Black Carbon in the Canadian High Arctic: 1981 – 2007. *Journal of Geophysical Research.* 115(D7): 1–9. doi:10.1029/2009JD012943.

Grannas, A. M., A. E. Jones, J. Dibb, M. Ammann, C. Anastasio, H. J. Beine, M. Bergin, et al. 2007. An Overview of Snow Photochemistry: Evidence, Mechanisms and Impacts. *Atmospheric Chemistry and Physics Discussion.* 7(2): 4165–4283.

Grenfell, T. C., S. J. Doherty, A. D. Clarke, and S. G. Warren. 2011. Light Absorption from Particulate Impurities in Snow and Ice Determined by Spectrophotometric Analysis of Filters. *Applied Optics.* 50(14): 2037–48.

Groendahl, L., T. Friborg, and H. Soegaard. 2007. Temperature and Snow-Melt Controls on Interannual Variability in Carbon Exchange in the High Arctic. *Theoretical and Applied Climatology.* 88(1-2): 111–25. doi:10.1007/s00704-005-0228-y.

Hadley, O. L., and T. W. Kirchstetter. 2012. Black-Carbon Reduction of Snow Albedo. *Nature Climate Change.* 2(6): 437-440.

Hansen, J., and L. Nazarenko. 2004. Soot Climate Forcing via Snow and Ice Albedos. *Proceedings of the National Academy of Sciences.* 101(2): 423–28. doi:www.pnas.org?cgi?doi?10.1073?pnas.2237157100.

Hedstrom, N. R., and J. W. Pomeroy. 1998. Measurements and Modelling of Snow Interception in the Boreal Forest. *Hydrological Processes.* 12(10-11): 1611–25.

Holtmeier, F.-K., and G. Broll. 2007. Treeline Advance – Driving Processes and Adverse Factors. *Landscape Online.* 1: 1–33. doi:10.3097/LO.200701.

Johansson, M., T. V. Callaghan, J. Bosiö, J. Akerman, M. Jackowicz-Korczynski, and T. R. Christensen. 2013. Rapid Responses of Permafrost and Vegetation to Experimentally Increased Snow Cover in Sub-Arctic Sweden. *Environmental Research Letters.* 8(3): 035025. doi:10.1088/1748-9326/8/3/035025.

Ju, J. C. and J. G. Masek. 2016. The vegetation greenness trend in Canada and US Alaska from 1984-2012 Landsat data. *Remote Sensing of Environment*. 176: 1-16.

Juszak, I., A. M. Erb, C. Maximov, and G. Schaepman-Strub. 2014. Arctic Shrub Effects on NDVI, Summer Albedo and Soil Shading. *Remote Sensing of Environment.* 153: 79–89. doi:10.1016/j.rse.2014.07.021.

Kokhanovsky, A., and E. P. Zege. 2004. Scattering Optics of Snow. *Applied Optics.* 43(7): 1589–1602. doi:10.1364/AO.43.001589.

Koven, C. D., W. J. Riley, and A. Stern. 2013. Analysis of Permafrost Thermal Dynamics and Response to Climate Change in the CMIP5 Earth System Models.” *Journal of Climate* 26(6): 1877-1900. doi:10.1175/JCLI-D-12-00228.1.

Lemay, M.-A., L. Provencher-Nolet, M. Bernier, E. Lévesque, and S. Boudreau. 2018. Spatially Explicit Modeling and Prediction of Shrub Cover Increase near Umiujaq, Nunavik. *Ecological Monographs.* 88(3): 385–407. doi:10.1002/ecm.1296.

Libois, Q., G. Picard, J. L. France, L. Arnaud, M. Dumont, C. M. Carmagnola, and M. D. King. 2013. Influence of grain shape on light penetration in snow. *The Cryosphere* 7(6): 1803–1818. https://doi.org/10.5194/tc-7-1803-2013

Libois, Q., G. Picard, M. Dumont, L. Arnaud, C. Sergent, E. Pougatch, M. Sudul, and D. Vial. 2014. Experimental Determination of the Absorption Enhancement Parameter of Snow. *Journal of Glaciology.* 60(222): 714–24. doi:10.3189/2014JoG14J015.

Liston, G. E., J. P. Mcfadden, M. Sturm, and R. A. Pielke. 2002. Modelled Changes in Arctic Tundra Snow, Energy and Moisture Fluxes due to Increased Shrubs. *Global Change Biology.* 8(1): 17–32. doi:10.1046/j.1354-1013.2001.00416.x.

Loranty, M. M., and S. J. Goetz. 2012. Shrub Expansion and Climate Feedbacks in Arctic Tundra. *Environmental Research Letters.* 7(1): 011005. doi:10.1088/1748-9326/7/1/011005.

Loranty, M. M., S. J. Goetz, and P. S. A. Beck. 2011. Tundra Vegetation Effects on Pan-Arctic Albedo. *Environmental Research Letters.* 6(2): 029601. doi:10.1088/1748-9326/6/2/029601.

Lund, M., B. U. Hansen, S. H. Pedersen, C. Stiegler, and M. P. Tamstorf. 2014. Characteristics of Summer-Time Energy Exchange in a High Arctic Tundra Heath 2000–2010. *Tellus B: Chemical and Physical Meteorology.* 66(1): 21631. doi:10.3402/tellusb.v66.21631.

Manninen, T., and E. Jääskeläinen. 2018. The Effect of Boreal Forest Canopy on Snow Covered Terrain Broadband Albedo. *Geophysical Society of Finland.* 53(1): 9–29.

McConnell, J. R., R. Edwards, G. L. Kok, M. G. Flanner, C. S. Zender, E. S. Saltzman, J. R. Banta, D. R. Pasteris, M. M. Carter, and J. D. W. Kahl. 2007. 20th-century Industrial Black Carbon Emissions Altered Arctic Climate Forcing. *Science.* 317(5843): 1381-1384. doi:10.1126/science.1144856.

Ménard, C. B., R. Essery, J. Pomeroy, P. Marsh, and D. B. Clark. 2014. A Shrub Bending Model to Calculate the Albedo of Shrub-Tundra. *Hydrological Processes.* 28(2): 341–51. doi:10.1002/hyp.9582.

Motulsky, H., and A. Christopoulos. 2005. Fitting Models to Biological Data Using Linear and Non-Linear Regression: A Practical Guide to Curve Fitting. *Statistics in Medicine* 24. doi:10.1002/sim.2181.

Moosmueller, H., R. K. Chakrabarty, and W. P. Arnott. 2009. Aerosol Light Absorption and Its Measurement : A Review. *Journal of Quantitative Spectroscopy & Radiative Transfer.* 110(11): 844–78. doi:10.1016/j.jqsrt.2009.02.035.

Myers-Smith, I. H., B. C. Forbes, M. Wilmking, M. Hallinger, T. Lantz, D. Blok, K. D. Tape, et al. 2011. Shrub Expansion in Tundra Ecosystems: Dynamics, Impacts and Research Priorities. *Environmental Research Letters* 6(4): 045509. doi:10.1088/1748-9326/6/4/045509.

Painter, T. H., N. P. Molotch, M. Cassidy, M. Flanner, and K. Steffen. 2007. Contact Spectroscopy for Determination of Stratigraphy of Snow Optical Grain Size. *Journal of Glaciology.* 53(180): 121–27.

Paradis, M., E. Lévesque, and S. Boudreau. 2016. Greater Effect of Increasing Shrub Height on Winter versus Summer Soil Temperature. *Environmental Research Letters.* 11(8): 085005. doi:10.1088/1748-9326/11/8/085005.

Pelletier, M., A. Allard, and E. Levesque. 2018. Ecosystem changes across a gradient of permafrost degradation in subarctic Québec (Tasiapik Valley, Nunavik, Canada). *Arctic*

Science. 5(1): 1-26. doi.org/10.1139/as-2016-0049.

Picard, G, Q. Libois, and L. Arnaud. 2016. Refinement of the Ice Absorption Spectrum in the Visible Using Radiance Profile Measurements in Antarctic Snow. *Cryosphere.* 10(6): 1–36.

Picard, G., F. Domine, G. Krinner, L. Arnaud, and E. Lefebvre. 2012. Inhibition of the Positive Snow-Albedo Feedback by Precipitation in Interior Antarctica. *Nature Climate Change* 2(11): 795–98. doi:10.1038/nclimate1590.

Pomeroy, J. W., D. S. Bewley, R. L. H. Essery, N. R. Hedstrom, T. Link, R. J. Granger, J. E. Sicart, C. R. Ellis, and J. R. Janowicz. 2006. Shrub Tundra Snowmelt. *Hydrological Processes* 20(4): 923–41. doi:10.1002/hyp.6124.

Provencher-Nolet, L., M. Bernier, and E. Lévesque. 2014. Short term change detection in tundra vegetation near Umiujaq, Subarctic Quebec, Canada. *Geoscience and Remote Sensing Symposium (IGARSS)*, 4668–70.

Rahn, K. A., and R. J. McCaffrey. 1980. On the Origin and Transport of the Winter Arctic Aerosol. *Annals of the New York Academy of Sciences.* 486–503.

Ramanathan, V., P. J. Crutzen, J. T. Kiehl, and D. Rosenfeld. 2001. Aerosols, Climate, and the Hydrological Cycle. *Science.* 294(5549): 2119–24. doi:10.1126/science.1064034.

Romanovsky, V. E., S. L. Smith, and H. H. Christiansen. 2010. Permafrost Thermal State in the Polar Northern Hemisphere during the International Polar Year 2007 – 2009: A Synthesis. *Permafrost and Periglacial Processes.* 21: 106–16. doi:10.1002/ppp.689.

Ropars, P., and S. Boudreau. 2012. Shrub Expansion at the Forest–tundra Ecotone: Spatial Heterogeneity Linked to Local Topography. *Environmental Research Letters.* 7(1): 015501. doi:10.1088/1748-9326/7/1/015501.

Rowe, P. M., R. R. Cordero, S. G. Warren, E. Stewart, S. J. Doherty, A. Pankow, M. Schrempf, et al. 2019. Black Carbon and Other Light- Absorbing Impurities in Snow in the Chilean Andes. *Nature Scientific Reports.* 9: 1–16. doi:10.1038/s41598-019-39312-0.

Schuur, E. A., A. D. McGuire, C. Schädel, G. Grosse, J. W. Harden, D. J. Hayes and S. M. Natali. 2015. Climate change and the permafrost carbon feedback. *Nature.* 520(7546): 171-179. doi: 10.1038/nature14338.

Semenchuk, P. R., M. A. K. Gillespie, S. B. Rumpf, N. Baggesen, B. Elberling, and E. J. Cooper. 2016. High Arctic Plant Phenology Is Determined by Snowmelt Patterns but Duration of Phenological Periods Is Fixed : An Example of Periodicity. *Environmental Research Letters.* 11(12): 125006. doi:10.1088/1748-9326/11/12/125006.

Skiles, S. M., M. Flanner, J. M. Cook, M. Dumont, and T. H. Painter. 2018. Radiative Forcing by Light-Absorbing Particles in Snow. *Nature Climate Change.* 8(11): 964-971. doi:10.1038/s41558-018-0296-5.

Skiles, S. M., T. Painter, and G. S. Okin. 2016. A Method to Retrieve the Spectral Complex Refractive Index and Single Scattering Optical Properties of Dust Deposited in Mountain Snow. *Journal of Glaciology* 63(237): 133–47. doi:10.1017/jog.2016.126.

Stevens, G. C., and J. F. Fox. 1991. The Causes of Treeline. *Annual Review of Ecology and Systematics.* 22(1): 177–91.

Sturm, M., T. Douglas, C. Racine, and G. Liston. 2005. Changing Snow and Shrub Conditions Affect Albedo with Global Implications. *Journal of Geophysical Research.* 110(G1): 1–13. doi:10.1029/2005JG000013.

Tape, K., M. Sturm, and C. Racine. 2006. The Evidence for Shrub Expansion in Northern Alaska and the Pan-Arctic. *Global Change Biology.* 12(4): 686–702. doi:10.1111/j.1365-2486.2006.01128.x.

Tuzet, F., M. Dumont, L. Arnaud, D. Voisin, M. Lamare, F. Larue, J. Revuelto, and G. Picard. 2019. Influence of Light Absorbing Particles on Snow Spectral Irradiance Profiles. *The Cryosphere Discussions.* 13(8): 1–33.

Tuzet, F., M. Dumont, M. Lafaysse, G. Picard, L. Arnaud, D. Voisin, Y. Lejeune, L. Charrois, P. Nabat, and S. Morin. 2017. A Multilayer Physically Based Snowpack Model Simulating Direct and Indirect Radiative Impacts of Light-Absorbing Impurities in Snow. *The Cryosphere.* 11(6): 2633–53. doi:https://doi.org/10.5194/tc-11-2633-2017.

Tuzet, F., M. Dumont, G. Picard, M. Lamare, D. Voisin, P. Nabat, M. Lafaysse, F. Larue, J. Revuelto, and L. Arnaud. 2020. Quantification of the Radiative Impact of Light-Absorbing Particles during Two Contrasted Snow Seasons at Col Du Lautaret (2058 M a. S. L., French Alps). *The Cryosphere Discussions*, no. January: 1–38.

Walker, D. A., J. C. Halfpenny, M. D. Walker, and C. A. Wessman. 1993. Long-Term Studies of Snow–Vegetation Interactions. *BioScience.* 43(5): 287–301. doi:10.2307/1312061.

Wang, X., S. J. Doherty, and J. Huang. 2013. Black Carbon and Other Light-Absorbing Impurities in Snow across Northern China. *Journal of Geophysical Research.* 118(3): 1471–92. doi:10.1029/2012JD018291.

Wang, L., S. L. Jacques, and L. Zheng. 1995. MCML—Monte Carlo modeling of light transport in multi-layered tissues. *Computer methods and programs in biomedicine.* 47(2): 131–146. doi:10.1016/0169-2607(95)01640-f.

Warren, S. G. 1982. Optical Properties of Snow. *Reviews of Geophysics and Space Physics.* 20(1): 67-89. doi:10.1029/RG020i001p00067.

Warren, S. G., and A. D. Clarke. 1986. Soot from Arctic haze: radiative effects on the Arctic snowpack. *Proceedings of the Snow Watch Workshop1985: Glaciological Data*, Vol. 18 (Boulder, CO: NSIDC, University of Colorado Boulder), 73–77.

Warren, S. G., and W. J. Wiscombe. 1980. A model for the spectral albedo of snow. II: Snow containing atmospheric aerosols. *Journal of Atmospheric Sciences.* 37(12): 2734-2745. doi: 10.1175/1520-0469(1980)037<2734:AMFTSA>2.0.CO;2

Warren, S. G. 2019. Optical Properties of Ice and Snow. *Philosophical Transactions of the Royal Society A.* 377: 2146.

General conclusions and outlook

In this PhD project we studied the effect of shrub expansion in the low-Arctic on albedo and the radiation budget in autumn and winter near Umiujaq, Northern Quebec (56.5°N, 76.5°W). A unique dataset was collected, consisting of first-time measurements of (i) spectral albedo of mixed snow-shrub surfaces (400–1080 nm), (ii) irradiance profiles in mixed snowpacks, and (iii) shrub architecture. These datasets were complemented with *in situ* measured snow physical properties to increase the fundamental understanding on shrub-snow-light interactions in the Arctic tundra and to develop an accurate yet simple parameterization for mixed surface albedo.

Previous studies had investigated the radiative impact of shrubs in spring, assuming that shrub-induced surface darkening is only significant when large amounts of radiation reach the Arctic. However, measurements here, conducted in autumn and winter 2015-2016, revealed that surface darkening in autumn reduced albedo by up to 55 % in the visible (400–750 nm) and by 18 % in the near infrared (750–1080 nm). These albedo-reductions increased the amount of absorbed energy by 70 W m^{-2} on 8 November 2015 and by 2–6 W m^{-2} on 2 December 2015, despite the relatively lower amounts of incoming radiation compared to spring. This leads to the conclusion that shrubs have a significant radiative impact during the entire snow season for latitudes at least up to 56.5°N.

The additional energy is mostly absorbed by protruding or buried branches, causing branch heating and driving complex shrub-snow interactions that depend on meteorological conditions. During warm spells in autumn, branch heating increases snow melting and enhances the formation of surface layers with melt-freeze crystals that have low SSA, reducing snow albedo. When temperatures are <0°C and it is too cold for snow melting, warm branches establish horizontal temperature gradients inside the snowpack, which enhances temperature gradient metamorphism and creates pockets of large depth hoar

crystals around branches, with efficient thermal insulation properties. In addition to these two heating-related effects, protruding branches at the snow surface increase aerodynamic roughness, which reduces wind speed and causes fresh snow with high SSA and high albedo to accumulate within shrubs. These complex shrub-snow-light interactions in autumn have important implications for the thermal regime and the microstructure of the snowpack, which can prevail for the rest of the snow season. The snow microstructure in turn is a key factor for snow albedo in the near infrared spectrum and for the insulating properties of the snowpack, thus affecting the thermal regime of permafrost. Shrubs and shrub-snow interactions also impact the temperatures at the snow-atmosphere boundary, which has implications for meteorological and climatological processes. These far-reaching ramifications of the complex snow-light-shrub interactions highlight how simplifying the radiative effect of shrubs in land surface models (LSMs) can cause significant inaccuracies in the simulation of land surface processes. LSMs in turn are a component of earth system models used to calculate climate change, and consequently, these inaccuracies transmit to climate projections which are an essential tool for scientists and policymakers to develop effective socio-economic strategies to respond to climate change.

As a first step towards more accurate simulations, we validated and improved the use of the Linear Mixing Equation (LME) as a parameterization of mixed surface albedo. The LME is used in most LSMs and is a simple equation requiring only three arguments, i.e. shrub albedo (α_{veg}), snow albedo (α_{snow}), and a weighting factor indicating the fractional surface covered by shrub branches. An extensive validation with *in situ* measured spectral albedo of mixed snow-shrub surfaces showed that carefully choosing the input parameters significantly increases the LME performance. More specifically, α_{veg} should be measured directly for shrub branches, instead of using hemispherical albedo measured over shrubs in autumn. Secondly, α_{snow} should be calculated with a snow radiative transfer model like TARTES as a function of snow SSA measurements, as this considers the impact of shrubs on SSA and snow albedo in extreme weather conditions. Using instead snow albedo measured over adjacent shrub-free sites returned satisfyingly accurate simulations most of the time but failed during extreme weather conditions, where for example wind-drifted snow accumulated in shrubs is different from eroded snow outside of shrubs. Finally, the calculation of the weighting factor in current implementations is either based on a set of

unverified equations describing shrub architecture, or requires the input of extensive *in situ* data preventing the LME to be used in a predictive way. Here we conducted a thorough analysis of shrub architecture to develop a validated allometric approach. The allometric approach allows calculating the weighting factor from shrub height and snow height which are readily accessible to modelers. The coupled allometric-LME approach simulated mixed surface albedo with an accuracy of 3 %, which is a significant improvement over simulations in previous studies which reported accuracies of 7 to 20 % when using the unverified LME approach.

However, before implementing the new approach in LSMs, further improvements and validation steps are required. 1) The coupled approach should be validated against shrub and albedo data from Arctic sites other than Umiujaq, Northern Quebec, to establish its general suitability. This step is particularly important because we found allometric equations to vary between sites with different environmental conditions. 2) Upscaling experiments should be conducted using airborne and satellite data to address the questions i) how accurate it is to use the allometric approach with average shrub height values in large grid cells and ii) how different shrub densities within grid cells may modify albedo calculations. 3) Findings on shrub architecture were determined for dwarf birches (*Betula glandulosa*) and it should be tested on other shrub species expanding in the Arctic (e.g. willow or alder). To avoid having to cut numerous shrubs and laboriously measure their branch dimensions, the possibility should be tested to apply photogrammetry methods to reliably determine shrub architecture. 4) We detected a systematic error in the new approach, which overestimated simulated albedo by 2 % compared to the measured data. The systematic error was probably caused by neglecting the influence of light-absorbing impurities and buried branches. To correct this error, it would be necessary to add an impurity term to the LME and to quantify the effect of buried branches. In this thesis we presented the first study on buried branch-light interactions and the results suggested that branches generally had a weak radiative impact. However a definite quantification of the radiative impact of buried branches was prevented by the unexpectedly high concentrations of black carbon in the Umiujaq snowpack which masked the effect of buried branches. For a future study it would be useful to measure irradiance profiles and simultaneously take snow samples which allow to determine concentrations and spectral absorption profiles of

impurities in order to distinguish the radiative effect of impurities and buried branches. 5) Finally, the equations established in this study are only suitable to calculate albedo during overcast conditions. In future work it would be necessary to adapt the allometric equations to direct light conditons also, in order to determine BAI as a function of shrub height, solar zenith angle and solar azimuth angle. Once these improvements are made and a large-scale validation is conducted, the coupled approach can easily be implemented in LSMs, finally allowing an accurate estimate of the magnitude of the current and projected impact of Arctic shrubification on global and regional warming. Considering the fast expansion of shrubs, and the large implications for the Arctic radiation budget, an implementation of an accurate parameterization is of the utmost importance.

Finally, the results of this research showed a measurable level of BC at all of the sampling sites with concentrations up to 185 ng g^{-1}. Observations in the field led to the conclusion that the likeliest source for these high BC concentrations was the open-air waste burning in proximity to our measuring sites. However, BC concentrations were deduced with a modeling approach and I suggest that this work should be extended in partnership with the community to identify the sources of BC in snow with absolute certainty. If found to be due to local waste burning, work with the community should be established to reduce this contamination and identify management and monitoring options.

I want to close this thesis with a personal note: I think it would be very important in the years to come to put an emphasis on a sustainable and ecological developement of northern communities. With an increasing number of scientists and tourists visiting the north, and a growing population in northern communities, air, water and soil pollution as well as the accumulation of large waste deposits may become a real problem. There are many examples of what happens if the potential impact of humans on the ecosystem is neglected and I hope that the same mistakes aren’t repeated as the Arctic opens up.

References

Akitaya, E. 1974. Studies on Depth Hoar. *Snow Mechanics.* 114: 42–48.

Arrhenius, S. 1896. XXXI. On the Influence of Carbonic Acid in the Air upon the Temperature of the Ground. *The London, Edinburgh, and Dublin Philosophical Magazine and Journal of Science.* 251 (41): 237–76. doi:10.1080/14786449608620846.

Barrere, M., F. Domine, B. Decharme, S. Morin, and V. Vionnet. 2017. Evaluating the Performance of Coupled Snow–Soil Models in SURFEXv8 to Simulate the Permafrost Thermal Regime at a High Arctic Site. *Geoscientific Model Development.* 10: 3461–79.

Barrere, M., F. Domine, M. Belke-Brea, D. Sarrazin. 2018. Snowmelt events in autumn can reduce or cancel the soil warming effect of snow–vegetation interactions in the Arctic. *Journal of Climate. 31*(23): 9507-9518.

Barry, R.G. and E. A. Hall-McKim. 2014. Essentials of the Earth's climate system. Cambridge University Press.

Berger, A., and C. Tricot. 1992. The Greenhouse Effect. *Surveys in Geosphysics.* 13(6): 523–49.

Bewley, D., R. Essery, J. Pomeroy, and C. Ménard. 2010. Measurements and Modelling of Snowmelt and Turbulent Heat Fluxes over Shrub Tundra. *Hydrology and Earth System Sciences.* 14: 1331–40.

Bonan, G. B. 2008. Forests and Climate Change : Climate Benefits of Forests. *Science.* 320(5882): 1444–49.

Bonfils, C. J. W., T. J. Phillips, D. M. Lawrence, P. Cameron-Smith, W. J. Riley, and Z. M. Subin. 2012. On the Influence of Shrub Height and Expansion on Northern High Latitude Climate. *Environmental Research Letters.* 7(1): 015503. doi:10.1088/1748-9326/7/1/015503.

Bright, R. M., E. Davin, T. O. Halloran, J. Pongratz, K. Zhao, and A. Cescatti. 2017. Local Temperature Response to Land Cover and Managment Change Driven by Non-Radiative Processes. *Nature Climate Change.* 7(4):296-302.

Brown, R., D. V. Schuler, O. Bulygina, C. Derksen, K. Luojus, L. Mudryk, L. Wang, and D. Yang. 2017. Arctic Terrestrial Snow Cover. *AMAP 2017 Snow, Water, Ice and Permafrost in the Arctic (SWIPA)* (2017): 269.

Büntgen, U., W. Tegel, K. Nicolussi, M. McCromick, D. Frank, V. Trouet, J. O. Kaplan, et al. 2011. 2500 Years of European Climate Variability and Human Susceptibility. *Science.* 331(6017): 578–82. doi:10.1126/science.1197175.

Callaghan, T. V., M. Johansson, R. D. Brown, P. Y. Groisman, N. Labba, V. Radionov, R. S. Bradley, et al. 2012. Multiple Effects of Changes in Arctic Snow Cover. *Ambio.* 40: 32–45. doi:10.1007/s13280-011-0213-x.

Chapin, F. S., M. Sturm, M. C. Serreze, J. P. McFadden, J. R. Key, A. H. Lloyd, A. D.

McGuire, et al. 2005. Role of Land-Surface Changes in Arctic Summer Warming. *Science.* 310(5748): 657–60. doi:10.1126/science.1117368.

Chapin, F. S., G. R. Shaver, A. E. Giblin, K. J. Nadelhoffer, and J. A. Laundre. 1995. Responses of Arctic Tundra to Experimental and Observed Changes in Climate. *Ecology.* 76(3): 694–711.

Chepstow-Lusty, A. J., M. R. Frogley, B. S. Bauer, M. J. Leng, K. P. Boessenkool, C. Carcaillet, A. A. Ali, and A. Gioda. 2009. Putting the Rise of the Inca Empire within a Climatic and Land Management Context. *Climate of the Past.* 5: 375–88.

Claussen, M. 2009. Late Quaternary Vegetation-Climate Feedbacks. *Climate of the Past.* 5: 203–16.

Cohen, J., J. Pulliainen, C. B. Ménard, B. Johansen, L. Oksanen, K. Luojus, and J. Ikonen. 2013. Effect of Reindeer Grazing on Snowmelt, Albedo and Energy Balance Based on Satellite Data Analyses. *Remote Sensing of Environment. 135:* 107-117.

Coumou, D., and S. Rahmstorf. 2012. A Decade of Weather Extremes. *Nature Climate Change.* 2(7):491-496. doi:10.1038/NCLIMATE1452.

Cowie, J., 2012. Climate Change: Biological and Human Aspects. Cambridge University Press.

Crowley, T. J. 2000. Causes of Climate Change Over the Past 1000 Years. *Science.* 289(5477): 270-277. doi:10.1126/science.289.5477.270.

Cullen, H. M., P. B. DeMenocal, S. Hemming, G. Hemming, F. H. Brown, T. Guilderson, and F. Sirocko. 2000. Climate Change and the Collapse of the Akkadian Empire : Evidence from the Deep Sea. *Geology.* 28(4): 379–82.

Derksen, C., and R. Brown. 2012. Spring snow cover extent reductions in the 2008–2012 period exceeding climate model projections. *Geophysical Research Letters.* 39: L19504. doi.org/10.1029/2012GL053387.

Déry, S. J., and R. D. Brown. 2007. Recent Northern Hemisphere Snow Cover Extent Trends and Implications for the Snow-Albedo Feedback. *Geophysical Research Letters.* 34: 2–7. doi:10.1029/2007GL031474.

Doherty, S. J., S. G. Warren, T. C. Grenfell, A. D. Clarke, and R. E. Brandt. 2010. Light-Absorbing Impurities in Arctic Snow. *Atmospheric Chemistry and Physics.* 10: 11647–80. doi:10.5194/acp-10-11647-2010.

Domine, F., J. Bock, S. Morin, and G. Giraud. 2011. Linking the Effective Thermal Conductivity of Snow to Its Shear Strength and Density. *Journal of Geophysical Research: Earth Surface.* 116(4): 1–10. doi:10.1029/2011JF002000.

Domine, F., M. Barrère, and D. Sarrazin. 2011. Seasonal evolution of the effective thermal conductivity of the snow and the soil in high Arctic herb tundra at Bylot Island, Canada. *The Cryosphere.* 10(6): 2573.

Domine, F., A. S. Taillandier, S. Houdier, F. Parrenin, W. R. Simpson, and T. A. Douglas. 2007. Interactions between Snow Metamorphism and Climate: Physical and Chemical Aspects. *Physics and Chemistry of Ice, [Proceedings of the International Conference*

on the Physics and Chemistry of Ice], 11th, Bremerhaven, Germany, July 23-28, 2006, 27–46.

Eddy, J. A. 1977. Climate and the Changing Sun. *Climate Change* 1: 173–90.

Elmendorf, S. C., G. H. R. Henry, R. D. Hollister, R. G. Björk, N. Boulanger-Lapointe, E. J. Cooper, J. H. C. Cornelissen, et al. 2012. Plot-Scale Evidence of Tundra Vegetation Change and Links to Recent Summer Warming. *Nature Climate Change.* 2(6): 453–57. doi:10.1038/nclimate1465.

Estilow, T. W., A. H. Young, and D. A. Robinson. 2015. A Long-Term Northern Hemisphere Snow Cover Extent. *Earth System Science Data.* 7(1): 137–42. doi:10.7289/V5N014G9.

Fernandes, R., H. Zhao, X. Wang, J. Key, X. Qu, and A. Hall. 2009. Controls on Northern Hemisphere Snow Albedo Feedback Quantified Using Satellite Earth Observations. *Geophysical Research Letters.* 36(21): 1–6. doi:10.1029/2009GL040057.

Flanner, M. G., K. M. Shell, M. Barlage, D. K. Perovich, and M. A. Tschudi. 2011. Radiative Forcing and Albedo Feedback from the Northern Hemisphere Cryosphere between 1979 and 2008. *Nature Geoscience.* 4(3):151-155. Nature Publishing Group: 151–55. doi:10.1038/ngeo1062.

France, J. L., M. D. King, M. M. Frey, J. Erbland, G. Picard, S. Preunkert, A. MacArthur, and J. Savarino. 2011. Snow Optical Properties at Dome C (Concordia), Antarctica; Implications for Snow Emissions and Snow Chemistry of Reactive Nitrogen. *Atmospheric Chemistry and Physics.* 11(18): 9787–9801. doi:10.5194/acp-11-9787-2011.

Fraser, R. H., T. C. Lantz, I. Olthof, S. V. Kokelj, and R. A. Sims. 2014. Warming-Induced Shrub Expansion and Lichen Decline in the Western Canadian Arctic. *Ecosystems.* 17: 1151–68. doi:10.1007/s10021-014-9783-3.

Frost, G. V., and H. E. Epstein. 2014. Tall Shrub and Tree Expansion in Siberian Tundra Ecotones since the 1960s. *Global Change Biology.* 20(4): 1264–77. doi:10.1111/gcb.12406.

Gallet, J.-C. C., F. Domine, C. S. Zender, and G. Picard. 2009. Measurement of the Specific Surface Area of Snow Using Infrared Reflectance in an Integrating Sphere at 1310 and 1550 Nm. *The Cryosphere.* 3(2): 167–82. doi:10.5194/tc-3-167-2009.

Grenfell, T. C. 2011. Albedo. Edited by V Singh, P Singh, and U Haritashya. *Encyclopedia of Snow, Ice and Glaciers*. 1st ed. The Netherlands: Springer. doi:10.1017/CBO9781107415324.004.

Grenfell, T. C., and G. A. Maykut. 1977. The Optical Properties of Ice and Snow in the Arctic Basin. *Journal of Glaciology.* 18(80): 445–63.

Grenfell, T. C., S. G. Warren, and P. C. Mullen. 1994. Reflection of Solar Radiation by the Antarctic Snow Surface at Ultraviolet, Visible, and near-Infrared Wavelengths. *Journal of Geophysical Research.* 99(D9): 18669. doi:10.1029/94JD01484.

Grenfell, T. C., and B. Light. 2002. Spatial Distribution and Radiative Effects of Soot in the

Snow and Sea Ice during the SHEBA Experiment. *Journal of Geophysical Research.* 107(C10): 1–7. doi:10.1029/2000JC000414.

Hays, J. D., J. Imbrie, and N. J. Shackleton. 1976. Variations in the Earth's Orbit : Pacemaker of the Ice Ages. *Science.* 194(4270): 1121-1132.

Imbrie, J., and J. Z. Imbrie. 1980. Modeling the Climatic Response to Orbital Variations. *Science.* 207(4434), 943-953.

Jahn, A., M. Claussen, A. Ganopolski, and V. Brovkin. 2005. Quantifying the Effect of Vegetation Dynamics on the Climate of the Last Glacial Maximum. *Climate of the Past.* 1: 1–16.

Jia, G. J., H. E. Epstein, and D. A. Walker. 2009. Vegetation Greening in the Canadian Arctic Related to Decadal Warming. *Journal of Environmental Monitoring.* 11(12): 2231–38. doi:10.1039/b911677j.

Ju, J., and J. G. Masek. 2016. The vegetation greenness trend in Canada and US Alaska from 1984–2012 Landsat data. *Remote Sensing of Environment.* 176: 1-16. doi:10.1039/b911677j.

Juszak, I., A. M. Erb, C. Maximov, and G. Schaepman-Strub. 2014. Arctic Shrub Effects on NDVI, Summer Albedo and Soil Shading. *Remote Sensing of Environment.* 153: 79–89. doi:10.1016/j.rse.2014.07.021.

Keeling, C. D., R. B. Bacastow, A. E. Bainbridge, C. A. Ekdahl, P. R. Guenther, and L. S. Waterman. 1976. Atmospheric Carbon Dioxide Variations at Mauna Loa Observatory , Hawaii. *Tellus.* 28(6): 538–51.

Kopp, G., and J. L. Lean. 2011. A New, Lower Value of Total Solar Irradiance : Evidence and Climate Significance. *Geophysical Research Letters.* 38(January): 1–7. doi:10.1029/2010GL045777.

Koven, C. D., B. Ringeval, P. Friedlingstein, P. Ciais, P. Cadule, D. Khvorostyanov, G. Krinner, and C. Tarnocai. 2011. Permafrost Carbon-Climate Feedbacks Accelerate Global Warming. *Proceedings of the National Academy of Sciences of the United States of America.* 108(36): 14769–74. doi:10.1073/pnas.1103910108.

Lantz, T. C., P. Marsh, and S. V. Kokelj. 2013. Recent Shrub Proliferation in the Mackenzie Delta Uplands and Microclimatic Implications. *Ecosystems.* 16: 47–59. doi:10.1007/s10021-012-9595-2.

Lawrence, D. M., and S. C. Swenson. 2011. Permafrost Response to Increasing Arctic Shrub Abundance Depends on the Relative Influence of Shrubs on Local Soil Cooling versus Large-Scale Climate Warming. *Environmental Research Letters.* 6(4): 045504. doi:10.1088/1748-9326/6/4/045504.

Legagneux, L., A. Cabanes, and F. Dominé. 2002. Measurement of the Specific Surface Area of 176 Snow Samples Using Methane Adsorption at 77 K. *Journal of Geophysical Research Atmospheres.* 107(D17): ACH-5. doi:10.1029/2001JD001016.

Lemke, P., J. Ren, R.B. Alley, I. Allison, J. Carrasco, G. Flato, Y. Fujii, et al. 2007. Observations: Changes in Snow, Ice and Frozen Ground. In *Climate Change 2007:*

The Physical Science Basis. Contribution of Working Group I to the Fourth Assessment Report of the Intergovernmental Panel on Climate Change, edited by S. Solomon, D. Qin, M. Manning, Z. Chen, M. Marquis, K.B. Averyt, M. Tignor, and H.L. Miller, 2:2004. Cambridge, United Kingdom: Cambridge University Press.

Libois, Q., G. Picard, J. L. France, L. Arnaud, M. Dumont, C. M. Carmagnola, and M. D. King. 2013. Influence of Grain Shape on Light Penetration in Snow. *Cryosphere.* 7(6): 1803–18. doi:10.5194/tc-7-1803-2013.

Liston, G. E, and C. A. Hiemstra. 2011. Representing Grass – and Shrub – Snow – Atmosphere Interactions in Climate System Models. *American Meteorological Society.* 24(8): 2061–79. doi:10.1175/2010JCLI4028.1.

Liston, G., and C. Hiemstra. 2011. The Changing Cryosphere : Pan-Arctic Snow Trends (1979–2009). *American Meteorological Society.* 24(21): 5691-5712. doi:10.1175/JCLI-D-11-00081.1.

Loranty, M. M., and S. J. Goetz. 2012. Shrub Expansion and Climate Feedbacks in Arctic Tundra. *Environmental Research Letters.* 7(1): 011005. doi:10.1088/1748-9326/7/1/011005.

Loranty, M. M., S. J. Goetz, and P. S. A. Beck. 2011. Tundra Vegetation Effects on Pan-Arctic Albedo. *Environmental Research Letters.* 6(2): 029601. doi:10.1088/1748-9326/6/2/029601.

Marsh, P., P. Bartlett, M. MacKay, S. Pohl, and T. Lantz. 2010. Snowmelt Energetics at a Shrub Tundra Site in the Western Canadian Arctic. *Hydrological Processes.* 24(25): 3603–20. doi:10.1002/hyp.7786.

McManus, K. M., Douglas C. Morton, J. G. Masek, D. Wang, J. O. Sexton, J. R. Nagol, P. Ropars, and S. Boudreau. 2012. Satellite-Based Evidence for Shrub and Graminoid Tundra Expansion in Northern Quebec from 1986 to 2010. *Global Change Biology.* 18(7): 2313–23. doi:10.1111/j.1365-2486.2012.02708.x.

Ménard, C. B., R. Essery, J. Pomeroy, P. Marsh, and D. B. Clark. 2014. A Shrub Bending Model to Calculate the Albedo of Shrub-Tundra. *Hydrological Processes* 28(2): 341–51. doi:10.1002/hyp.9582.

Milankovitch, M. 1948. Ausbau und gegenwärtiger Stand der astronomischen Theorie der erdgeschichtlichen Klimate. *Experientia.* 4(11): 413-418.

Mudryk, L. R., P. J. Kushner, C. Derksen, and C. Thackeray. 2017. Snow Cover Response to Temperature in Observational and Climate Model Ensembles. *Geophysical Research Letters.* 44: 919–26. doi:10.1002/2016GL071789.

Myers-Smith, I. H., B. C. Forbes, M. Wilmking, M. Hallinger, T. Lantz, D. Blok, K. D. Tape, et al. 2011. Shrub Expansion in Tundra Ecosystems: Dynamics, Impacts and Research Priorities. *Environmental Research Letters.* 6(4): 045509. doi:10.1088/1748-9326/6/4/045509.

O'Brian, H.W., and R.H. Munis. 1975. Red and near-Infrared Spectral Reflectance of Snow. *Corps of Engineers, US Army, Cold Regions Research and Engineering Laboratory.* 332: 24–35.

Overland, J. E., and M. Wang. 2016. Recent Extreme Arctic Temperatures are due to a Split Polar Vortex. *Journal of Climate*. 29: 5609–17. doi:10.1175/JCLI-D-16-0320.1.

Picard, G., Q. Libois, and L. Arnaud. 2016. Refinement of the Ice Absorption Spectrum in the Visible Using Radiance Profile Measurements in Antarctic Snow. *Cryosphere*. 10(6): 1–36.

Picard, N., L. Saint-André, and M. Henry. 2012. Manual for Building Tree Volume and Biomass Allometric Equations: From Field Measurement to Prediction. *FAO/CIRAD*.

Pielke, R. A., G. Marland, R. A. Betts, T. N. Chase, J. L. Eastman, J. O. Niles, D. dutta S Niyogi, S. W. Running, and P. Trans. 2002. The Influence of Land-Use Change and Landscape Dynamics on the Climate System: Relevance to Climate-Change Policy beyond the Radiative Effect of Greenhouse Gases. *Philosophical Transactions of the Royal Society B.* 360: 1–15. doi:10.1098/rsta.2002.1027.

Pomeroy, J. W., D. S. Bewley, R. L. H. Essery, N. R. Hedstrom, T. Link, R. J. Granger, J. E. Sicart, C. R. Ellis, and J. R. Janowicz. 2006. Shrub Tundra Snowmelt. *Hydrological Processes* 20(4): 923–41. doi:10.1002/hyp.6124.

Poynting, J.H. 1907. LXXIV. On Prof. Lowell's Method for Evaluating the Surface-Temperautres of the Planets; with an Attempt to Represent the Effect of Day and Night on the Temperature of the Earth. *The London, Edinburgh, and Dublin Philosophical Magazine and Journal of Science.* 84(14): 749–60. doi:10.1080/14786440709463737.

Provencher-Nolet, L., M. Bernier, and E. Lévesque. 2014. Short term Change Detection in Tundra Vegetation near Umiujaq, Subarctic Quebec, Canada. In *Geoscience and Remote Sensing Symposium (IGARSS)*, 4668–70.

Ramanathan, V. 1988. The Greenhouse Theory of Climate Change: A Test by an Inadvertent Global Experiment. *Science.* 240(4850): 293–99.

Roche, Y., and M. Allard. 1996. L'enneigement et la dynamique du pergélisol: l'exemple du détroit de Manitounuk, Québec nordique. *Géographie physique et Quaternaire.* 50(3): 377-393.

Ropars, P., and S. Boudreau. 2012. Shrub Expansion at the Forest–Tundra Ecotone: Spatial Heterogeneity Linked to Local Topography. *Environmental Research Letters.* 7(1): 015501. doi:10.1088/1748-9326/7/1/015501.

Schaefer, K., H. Lantuit, V. E. Romanovsky, E. G. Schuur, and R. Witt. 2014. The Impact of the Permafrost Carbon Feedback on Global Climate. *Environmental Research Letters.* 9(8): 085003. doi:10.1088/1748-9326/9/8/085003.

Schaefer, K., T. Zhang, L. Bruhwiler, and A. P. Barrett. 2011. Amount and Timing of Permafrost Carbon Release in Response to Climate Warming. *Tellus, Series B: Chemical and Physical Meteorology.* 63(2): 165–80. doi:10.1111/j.1600-0889.2011.00527.x.

Schmidt, R. A. 1984. Transport Rate of Drifting Snow and the Mean Wind Speed Profile. *Boundary-Layer Meteorology.* 34: 231–41.

Schuur, E.A., J. Bockheim, J. G. Canadell, E. Euskirchen,C. B. Field, S. V. Goryachkin, S.

Hagemann, P. Kuhry, P. M. Lafleur, H. Lee, and G. Mazhitova. 2008. Vulnerability of Permafrost Carbon to Climate Change: Implications for the Global Carbon Cycle. *BioScience*. *58*(8): 701-714.

Schuur, E. A. G., A. D. McGuire, G. Grosse, J. W. Harden, D. J. Hayes, G. Hugelius, C. D. Koven, and P. Kuhry. 2015. Climate Change and the Permafrost Carbon Feedback. *Nature.* 520: 171–79. doi:10.1038/nature14338.

Schuur, E. A. G., and M. C. Mack. 2018. Ecological Response to Permafrost Thaw and Consequences for Local and Global Ecosystem Services. *Annual Reviews of Ecology, Evolution, and Systematics.* 49: 279–301.

Serreze, M. C., A. P. Barrett, J. C. Stroeve, D. N. Kindig, and M. M. Holland. 2009. The Emergence of Surface-Based Arctic Amplification. *The Cryosphere.* 3: 11–19.

Sommerfeld, R.A., and E. LaChapelle. 1970. The Classification of Snow. *Journal of Glaciology*. 9(55): 3-18. doi:10.1002/j.1477-8696.1950.tb01198.x.

Stephens, G. L., J. Li, M. Wild, C. A. Clayson, N. Loeb, S. Kato, T. L. Ecuyer, P. W. Stackhouse Jr, M. Lebsock, and T. Andrews. 2012. An Update on Earth's Energy Balance in Light of the Latest Global Observations. *Nature Geoscience.* 5(10): 691-696. doi:10.1038/ngeo1580.

Strack, J. E., R. A. Pielke, and G. E. Liston. 2007. Arctic Tundra Shrub Invasion and Soot Deposition: Consequences for Spring Snowmelt and near-Surface Air Temperatures. *Journal of Geophysical Research: Biogeosciences.* 112(4): 1–12. doi:10.1029/2006JG000297.

Sturm, M., and I. C. S. Benson. 1997. Vapor Transport, Grain Growth and Depth-Hoar Developement in the Subarctic Snow. *Journal of Glaciology.* 43(143): 42-59. doi:10.3198/1997JoG43-143-42-59.

Sturm, M., T. Douglas, C. Racine, and G. Liston. 2005. Changing Snow and Shrub Conditions Affect Albedo with Global Implications. *Journal of Geophysical Research.* 110(G1): 1–13. doi:10.1029/2005JG000013.

Sturm, M., J. P. Mcfadden, G. E. Liston, F S. Chapin III, C. H. Racine, and J. Holmgren. 2001. Snow–Shrub Interactions in Arctic Tundra: A Hypothesis with Climatic Implications. *Journal of Climate.* 14: 336–44.

Tape, K., M. Sturm, and C. Racine. 2006. The Evidence for Shrub Expansion in Northern Alaska and the Pan-Arctic. *Global Change Biology.* 12(4): 686–702. doi:10.1111/j.1365-2486.2006.01128.x.

Tarnocai, C., J. G. Canadell, E. A G Schuur, P. Kuhry, G. Mazhitova, and S. Zimov. 2009. Soil Organic Carbon Pools in the Northern Circumpolar Permafrost Region. *Global Biogeochemical Cycles.* 23(2): 1–11. doi:10.1029/2008GB003327.

Tuzet, F., M. Dumont, L. Arnaud, D. Voisin, M. Lamare, F. Larue, J. Revuelto, and G. Picard. 2019. Influence of Light Absorbing Particles on Snow Spectral Irradiance Profiles. *The Cryosphere.* 13(8): 1–33.

Tyndall, F.R.S. 1861. On the Absorption and Radiation of Heat by Gases and Vapours, and

on the Physical Connexion of Radiation, Absorption, and Conduction. *Proceedings of the Royal Society of London.* 11: 100–104.

Vonder Haar, T. H., G. G. Campbell, E. A. Smith, A. Arking, K. Coulson, J. Hickey, F. House, et al. 1981. Measurements of the Earth Radiation Budget from Satellites during the First Garp Global Experiment. *Advances in Space Research.* 1: 285–97.

Warren, S. G. 1982. Optical Properties of Snow. *Reviews of Geophysics and Space Physics*. 20(1):67-89. doi:10.1029/RG020i001p00067.

Warren, S. G., and R. E. Brandt. 2008. Optical Constants of Ice from the Ultraviolet to the Microwave: A Revised Compilation. *Journal of Geophysical Research: Atmospheres.* 113(D14): D14220. doi:10.1029/2007JD009744.

Wiscombe, and Warren. 1980. A Model for the Spectral Albedo of Snow. I: Pure Snow. *Journal of the Atmospheric Sciences.* 37(12): 2712-2733.

Xu, C., T. A. Kohler, T. M. Lenton, J.-C. Svenning, and M. Scheffer. 2020. Future of the Human Climate Niche. *Proceedings of the National Academy of Sciences.* 117(21): 11350–55. doi:10.1073/pnas.1910114117.

Zhang, T. 2005. Influence of Seasonal Snow Cover on the Ground Thermal Regime: An Overview. *Reviews in Geophysics.* 43(2004): 1–23. doi:10.1029/2004RG000157.1.INTRODUCTION.

Appendix A – Albedo measured over shrubby surfaces

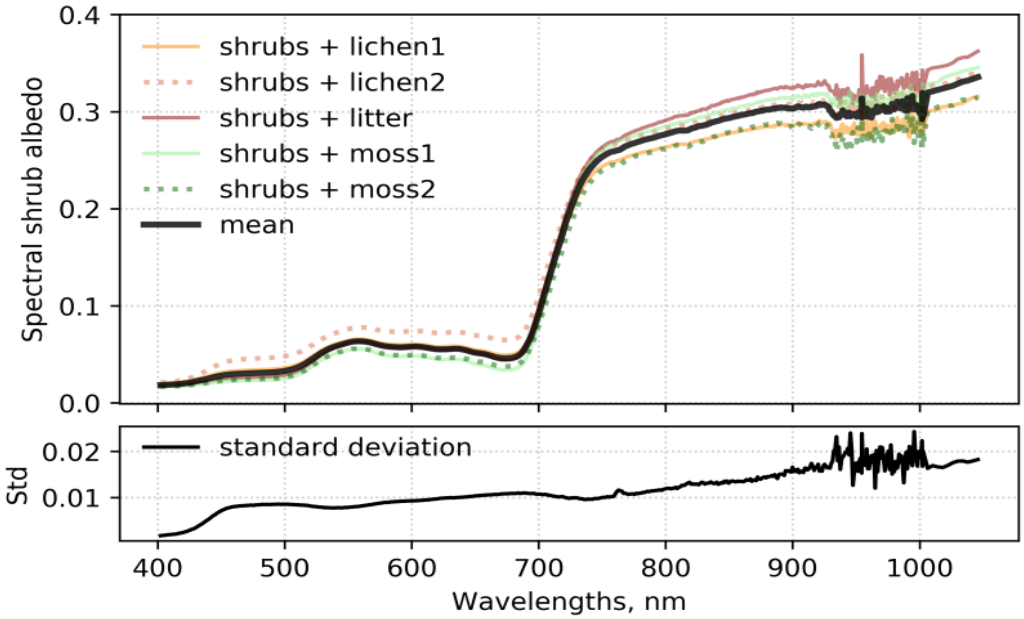

Figure A1. Spectral shrub albedo measured during the late summer campaign 2015 for shrubs growing on lichen (2 measurements), moss (2 measurements) or soil covered by fallen leaves (litter, 1 measurement).

Appendix B – Propagated errors

B1. Propagated errors of calculated weighting factors

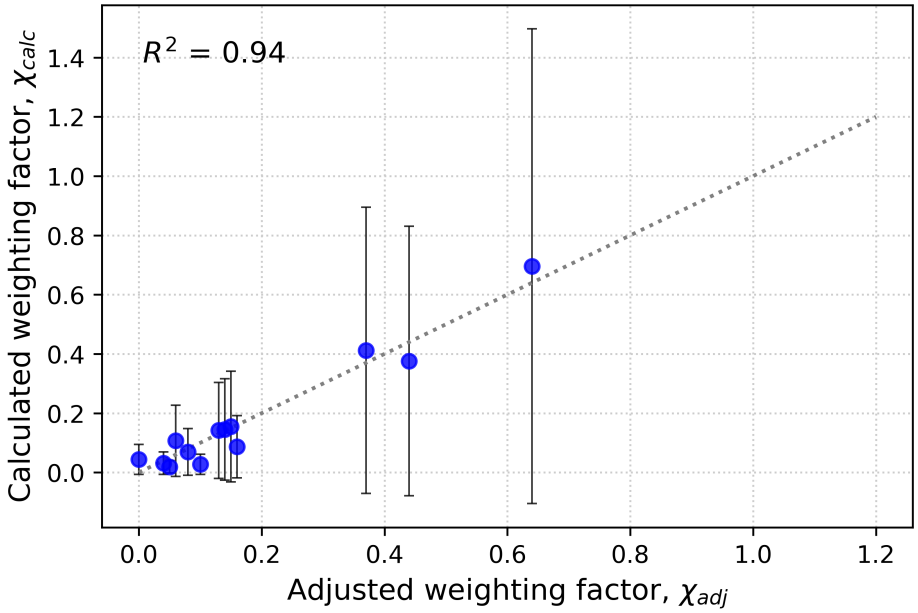

Figure B1. Correlation of adjusted weighting factor (χ_{adj}) and calculated weighting factor (χ_{calc}). The former was taken from the modeling results of Chapter 1 (Belke-Brea et al. 2019). Vertical error bars indicate the χ_{calc} errors calculated from the error propagation shown in the Appendix B2.

B2. Calculating error propagation

The errors of the fitted coefficients *a* and *b* in Eq. (3.2) were calculated from the covariance matrix returned by the scipy.optimize.curve_fit (which is a wrapper of the scipy.optimize.least_squares function). To calculate the errors propagated from the fitted coefficients to BAI_{total}, $BAI_{exposed}$, k, χ and finally α_{mix}, we used the variance formula of Gauss. The propagated errors are thus calculated from the partial derivatives of each respective equation for BAI_{total}, $BAI_{exposed}$, k, χ and α_{mix} which are shown below (together with the original equations).

The equation for BAI_{total} is:

$$BAI_{total} = a \cdot H_{\text{veg}}^{b} \qquad \text{B2.Eq. (1)}$$

and the error ΔBAI_{total} is calculated from:

$$\Delta BAI_{total} = H_{veg}^{b} \cdot \Delta a + a \cdot H_{\mathrm{veg}}^{b} \cdot \log\left(h_{veg}\right) \cdot \Delta b \qquad \text{B2.Eq. (2)}$$

The equation for $BAI_{exposed}$ is:

$$BAI_{exposed} = f_{\exp} \cdot BAI_{total} \qquad \text{B2.Eq. (3)}$$

and the error $\Delta BAI_{exposed}$ is given by:

$$\Delta BAI_{exposed} = f_{\exp} \cdot \Delta BAI_{total} \qquad \text{B2.Eq. (4)}$$

The equation for k is:

$$k = 1 + \alpha_{snow} \cdot \left(1 - BAI_{exposed}\right) \qquad \text{B2.Eq. (5)}$$

and the error Δk results from:

$$\Delta k = -\alpha_{snow} \cdot \Delta BAI_{exposed} \qquad \text{B2.Eq. (6)}$$

The equation for χ is:

$$\chi = k \cdot f_{\exp} \cdot BAI_{total} \qquad \text{B2.Eq. (7)}$$

and the error $\Delta\chi$ is calculated from:

$$\Delta\chi = f_{\exp} \cdot BAI_{total} \cdot \Delta k + k \cdot f_{\exp} \cdot \Delta BAI_{total} \qquad \text{B2.Eq. (8)}$$

Finally α_{mix} results from:

$$\alpha_{mix} = \left(1 - \chi\right) \cdot \alpha_{snow} + \chi \cdot \alpha_{veg} \qquad \text{B2.Eq. (9)}$$

and the error $\Delta\alpha_{mix}$ is given by:

$$\Delta\alpha_{mix} = \left(\alpha_{veg} - \alpha_{snow}\right) \cdot \Delta\chi \qquad \text{B2.Eq. (10)}$$

Appendix C – Wind speed Umiujaq coast vs. Tasiapik valley

Wind speed on the coast is almost always greater than in the valley. As an example, Figure C1 compares average hourly wind speed data from a station located 10 m from shore to those obtained in the valley. Both stations used a Young anemometer at the top of a 10 m tower. The wind speed distribution curve for the coast is clearly significantly higher than that for the valley. In the valley, wind speed is >10 m s^{-1} 3.85 % of the time, whereas that value is reached 10.62 % of the time on the coast.

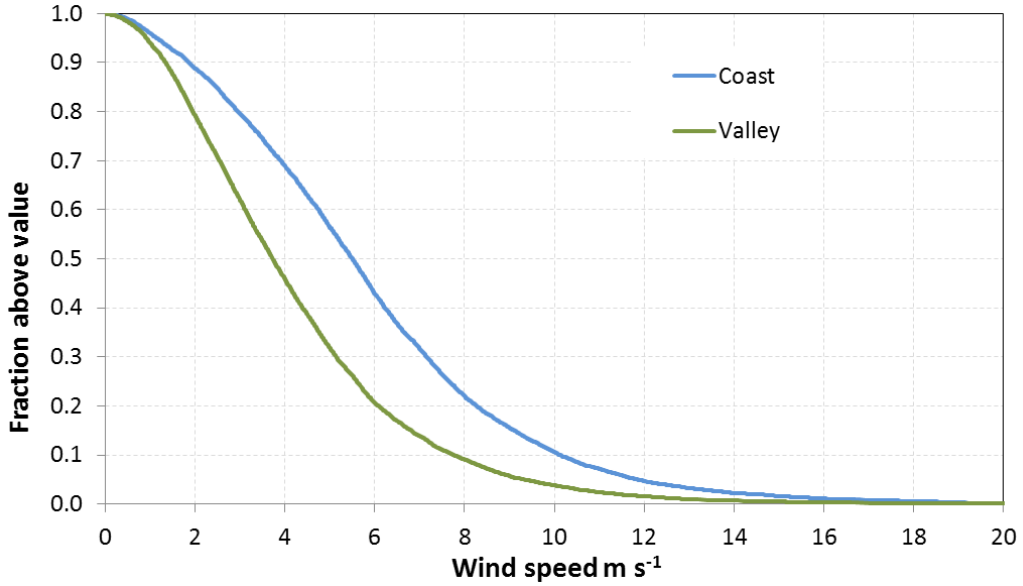

Figure C1. Comparison of wind speed distributions on the coast and in the valley for the year 2013

Appendix D – Wavelength-dependent SnowMCML simulations

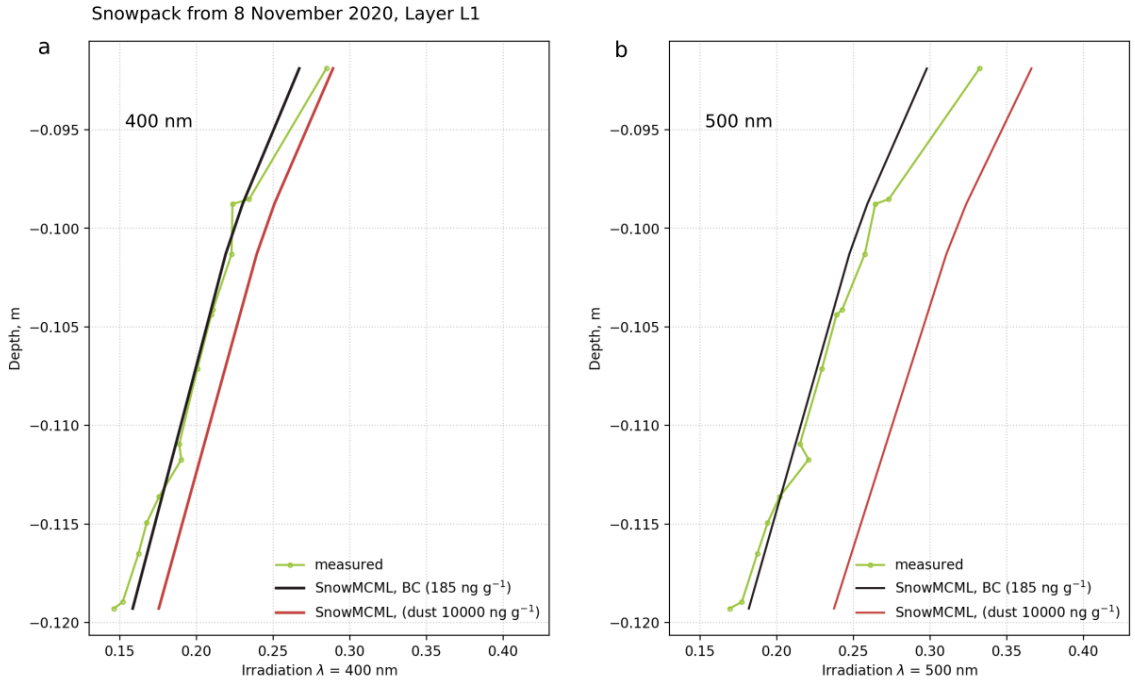

Figure D1. SOLEXS irradiance profiles and SnowMCML simulations at 400 nm (a) and 500 nm (b) for 8 Nov. SnowMCML simulations were computed either with impurity type set to mineral dust (red plots) or BC (black plots). Using BC returns a good fit-quality independent of wavelength, while the fit with dust varies from 400 to 500 nm.